Dissertation

submitted to the
Combined Faculty of Natural Sciences and Mathematics
of the Ruperto-Carola-University of Heidelberg, Germany
for the degree of
Doctor of Natural Sciences

Put forward by
Carina da Costa Castanheira
born in Espariz Tábua (Portugal)

Oral examination: January 25$^{\text{th}}$, 2023

Controlling the time-dependent dipole response in liquid-phase targets

Referees: Prof. Dr. Thomas Pfeifer

Prof. Dr. Andreas Wolf

Laser-induzierte Kontrolle der zeitabhängigen Dipolantwort in Flüssigphase:

Diese Arbeit beschäftigt sich mit der Fragestellung wie die Absorption von flüssigen Proben durch dynamische Wechselwirkung zweier ultrakurzer Laserimpulse verändert werden kann. Dabei hängt das durch den ersten Laserimpuls im Medium generierte Dipolmoment von drei Faktoren ab: Lösemittel, gelöstes Molekül und Laserimpuls Form. In dieser Arbeit wird gezeigt, dass das Absorptionsspektrum von gelösten Aluminium-Chlorid-Phthalocyanin (AlClPc)-Komplexen durch die Interaktion mit einem zweiten, zeitlich verzögerten, Laserimpuls modifiziert werden kann. Die zeitabhängigen Effekte im Molekül können dabei durch Laser-induzierte kohärente Kopplungsdynamiken zwischen dem Grundzustand und einem Ensemble angeregter Zustände erklärt werden, welches mittels einer Mehrlevel Simulation im Rahmen dieser Arbeit bestätigt wird. Darüber hinaus wird im Rahmen einer zweiten Simulation untersucht welche zusätzlichen zeitabhängigen Effekte durch die Präsenz des Lösemittels und die zeitliche Entwicklung der Laserimpuls Form generiert werden. Die präsentierten Ergebnisse leisten einen Beitrag zu einem tieferen Verständnis der Wechselwirkung zwischen intensiven Laserfeldern und komplexen Molekülen in Lösung. Dies kann in der Zukunft dafür verwendet werden die Dynamik in komplexen Systemen gezielter zu kontrollieren.

Controlling the time-dependent dipole response in liquid-phase targets:

This thesis focuses on the dynamical changes in the absorption of liquid-phase targets due to the interaction with strong, ultrashort laser pulses. Therefore, it is shown that the absorption spectrum of aluminum chloride phthalocyanine (AlClPc) in the liquid phase can be dynamically modified through the time-resolved interaction with a second laser pulse, which can be explained by laser-induced coherent coupling dynamics between the ground state and an ensemble of excited states, as reproduced by a few-level toy model. Furthermore, it is shown which time-dependent effects upon the measured absorption spectra are generated due to the presence of the solvent and the non-trivial pulse-form itself, which is confirmed through a second simulation. The presented results contribute to a better understanding in how intense laser fields interact with complex molecules in solution and can, in the future, be used to improve dynamic laser-control of complex systems.

Contents

1. Introduction

With the invention of the first laser in the 1960s [1, 2], it became possible to investigate the first (fully) coherent interactions between matter and light. Over the years the field has largely expanded and technologic improvements such as Q-switching [3], mode-locking [4–7] and chirped-pulse amplification [8] enabled the creation of intense ultrashort laser pulses. This opened up the possibility to resolve intrinsic atomic and molecular timescales, thereby establishing the field of time-resolved ultrafast spectroscopy [9]. A multitude of different experimental techniques to study the ultrafast light-matter interaction of atomic, molecular and solid-state systems have been developed throughout the years [10]. These light-matter interactions enable the coherent control of atomic and molecular systems. In the thus created field of quantum coherent control one aims to place the investigated system in a desired (quantum) state by the interaction with light. Experimental techniques which were developed to fulfill this task are, for example, feedback-optimized control with spectrally or temporally shaped ultrashort laser pulses and two-dimensional spectroscopy [11–13]. These techniques aim for coherent control using weak fields with a perturbative approach. But also, strong fields exceeding the non-perturbative regime can be used to efficiently control not only atomic [14], but also complex molecular dynamics [15–17].

Experimental concepts using coherent laser-control are widely used to efficiently control matter [18–20]. It has been shown that the optical response of atomic and molecular targets in the gaseous phase can be controlled by XUV-NIR multi-pulse experiments, which could be understood through laser-induced couplings between isolated electronic states [21–24], also including vibrational couplings [25–29]. Using this approach, the dipole response can be selectively modified and controlled with intense fields [30–32]. In more complex systems such as molecules dissolved in solution, the coupling to a bath leads to rather rapid decoherence effects [33–37], which increases the intricacy of coherent light-matter interaction. Nevertheless, coherent-control concepts have been realized in these complex systems [11, 12, 38] and can also be

understood through atom-like modelling [16, 39]. Based on existing dynamic coherent-control concepts established in the XUV-NIR spectral region on gas phase targets [14, 31, 40] this work aims to expand the dynamic control of absorption spectra to the liquid phase using time-resolved absorption spectroscopy in the visible (VIS) to near-infrared (NIR) regime.

The conceptual idea of measuring and controlling the optical dipole response is the following: First a weak excitation pulse induces a freely decaying dipole response at time $t = 0$ in the target. This free-induction decay interferes with the electric field of the excitation pulse, leading to the characteristic (unperturbed) static absorption spectrum of the system imprinted on the excitation pulse spectrum. The subsequent interaction of a second pulse (at time $t = \tau > 0$) with the initially induced dipole response, can lead to a coherent modification of it. This effect is also known as perturbed free-induction decay [41–43] and leads to characteristic spectral modifications of the absorption spectrum of the excitation pulse [22, 24, 31].

The spectral information is thereby obtained through the use of a grating spectrometer, which intrinsically performs the Fourier transform. In this way, a time-integrated spectral measurement is made, which includes both the excitation pulse at $t = 0$ and its (in the presence of the control pulse, possibly perturbed) dipole response for $t > 0$. Using this time-domain picture of light-matter interaction, the absorption of light can be understood in the impulsive limit of a time-domain (dipole) response function, the laser control of which is only possible while the system still reacts coherently upon the initial (excitation-induced) impulsive stimulus. Provided a sufficiently short excitation pulse is used, the full real-time action of the control pulse on the system's dynamics can be retrieved from the measured absorption spectrum [32].

With this knowledge laser-induced coupling dynamics have been extracted across isolated atomic [23, 30, 44] and molecular [26, 27, 39] resonances. In this work the aforementioned laser-control concepts of absorption spectra and the dipole response are applied to an organo-metallic complex in the liquid phase to explore new possibilities to dynamically control the system's absorption properties. Therefore, the impact of a strong laser field on a molecular coherence is experimentally and computationally explored. The molecular coherence is encoded in the weak-field excitation-only absorption spectrum on which the concept of the induced dipole moment and its manipulation is applied. In addition, this approach is supported by reproducing the measured coherent effects of the dynamically modified dipole response by using a numerical atom-like few-level toy model.

The target of interest are aluminum phthalocyanine chloride (AlClPc) complexes dissolved in a mixture of ethanol and ultra-pure water. By virtue of their outstanding electronic and optical properties, phthalocyanines enjoy a variety of industrial and medical applications such as solar cells [45, 46] and photodynamic therapy (PDT) of tumors [47–49]. In addition, phthalocyanines are thermally and chemically stable, which makes them adequate candidates for the interaction with intense laser fields in the liquid phase. Their ground state absorption is in general governed by a π-π^* transition of the 18 delocalized π-electrons of the phthalocyanine ring resulting in two characteristic absorption bands, namely the Soret- (300 – 350 nm) and the Q-band (600 – 700 nm) [50].

This thesis is structured as follows: Chapter 2 provides an overview of the basic theoretical concepts relevant throughout this thesis. It is subdivided in four main sections which focus on the theoretical treatment of ultrashort light pulses, transient absorption spectroscopy, quantum dynamics of laser-coupled few-level systems and the electronic absorption-band structure of molecules in the liquid phase. Chapter 3 presents the experimental setup used to perform the measurements presented in this thesis. It is subdivided in 5 sections, presenting the laser system, the generation of ultrashort broadband light pulses, their characterization via the dispersion scan (D-scan) technique, as well as the experimental setup used for the coherent control of transient absorption spectra in two different versions. In addition, the sample characterization setup is presented, which was used to characterize and optimize the target. The results of the target's characterization are presented in chapter 4. In chapter 5, both the measurement concept used to convey strong-field laser-induced coherent control of the optical response of dissolved AlClPc molecules is presented, as well as the data evaluation and the experimental results. These include the characterization of the ultra-short laser pulses and the treatment of measurement difficulties/artifacts for both measurement runs (1&2), separately. Chapter 6 focuses on the modeling of the in chapter 5 observed effects. Therefore, it is divided into the following three sub-chapters: Chapter 6.1 deals with the simulation of the laser-control of AlClPc's time-dependent dipole moment. After showing that an atom-like few level simulation suffices to reproduce the observed effects, chapter 6.2 focuses on the treatment of measurement artifacts due to the generation of cross-phase modulation (XPM) in the solvent and how by this the laser pulses' temporal structure is imprinted onto the absorbance of the pure solvent. Chapter 6.3 shows how the presence of the generated XPM signal superimposes with the laser-induced optical response of AlClPc,

leading to additional features in both absorbance and Fourier energy. Finally, chapter 7 concludes this thesis by giving a summary of the main findings and an outlook.

2. Theoretical background

The main focus of this work is the interaction between light and molecules on ultrafast timescales. Therefore, this chapter's aim is to lay out the theoretical background of the physical concepts used in this thesis to analyze and interpret the experimental data later on. This chapter starts with the mathematical description of ultrashort laser pulses and their interaction with matter in section 2.1, followed by an introduction into the concept of transient absorption spectroscopy in section 2.2. After introducing the essentials of quantum dynamics in section 2.3, this chapter closes with a summary about the physical and chemical properties of this thesis' main target aluminum chloride phthalocyanine given in section 2.4. More detailed information can be found in standard textbooks [9, 51–56] which have been used as references for the following sections.

2.1. Ultrashort light pulses

As the shutter time of any detector is the limiting factor in observing a dynamical process without blurring, the constraint to resolve quantum dynamics in the time domain is the duration of the light-pulses used to initiate and steer the dynamical process. With the invention of the first laser in the 1960s [2] coherent laser pulses have become one of the main tools to investigate quantum dynamics directly in the time domain. Over the years, technological improvements such as Q-switching [3], mode-locking [5] and chirped-pulse amplification [8] enabled the creation of intense ultrashort laser pulses, which in turn made it possible to resolve intrinsic atomic and molecular timescales, thereby, establishing the field of time-resolved ultrafast spectroscopy [9]. For more details on the properties and characteristics of ultrashort laser pulses the reader is referred to look into [53].

2.1.1. Mathematical description

As already emphasized, ultrashort laser pulses are an optimal tool to study the electron dynamics in atoms and molecules. Given the laser pulses are well characterized, the pulse-induced atomic/molecular dynamics can be extracted. Therefore, one first needs to know the pulses used. These can be in general described in time and space by the electric field $\mathbf{E}(t, x, y, z)$. Assuming linear polarization, the electric field in the time domain can be simplified to:

$$E(t) = \mathcal{E}(t)e^{i\phi(t)}, \tag{2.1}$$

with the temporal phase $\phi(t)$ and the complex envelope $\mathcal{E}(t)$. Knowing the spectral distribution, a laser pulse can also be defined in the frequency domain via:

$$E(\omega) = \mathcal{E}(\omega)e^{i\varphi(\omega)}, \tag{2.2}$$

with the spectral phase $\varphi(\omega)$ and the spectral amplitude $\mathcal{E}(\omega)$. The temporal and spectral representations of the electric field are directly connected via Fourier transformation. Therefore, if the spectral field is given, the Fourier transform returns the temporal electric field and vice versa:

$$E(t) = \frac{1}{\sqrt{2\pi}} \int_{-\infty}^{\infty} E(\omega)e^{i\omega t}d\omega, \tag{2.3}$$

$$E(\omega) = \frac{1}{\sqrt{2\pi}} \int_{-\infty}^{\infty} E(t)e^{-i\omega t}dt. \tag{2.4}$$

The intensity of a laser pulse (measured in units $\mathrm{W/m^2}$) is defined as the average of one optical period T:

$$I(t) = \epsilon_0 cn \frac{1}{T} \int_{t-\frac{T}{2}}^{t+\frac{T}{2}} E^2(t')dt', \tag{2.5}$$

where ϵ_0, c and n are the dielectric permittivity, the vacuum speed of light and the refractive index of the propagation medium. In addition to the temporal intensity $I(t)$, also the spectral intensity can be measured experimentally, which is in turn given by:

$$S(\omega) = 2\epsilon_0 cn|E(\omega)|^2. \tag{2.6}$$

As $S(\omega)$ is usually measured with slow detectors, it is a time-averaged quantity. Looking at equation 2.6 one notices that the spectral phase $\varphi(\omega)$ is lost during the measurement and, therefore, also the crucial information about the pulse shape. To

characterize the pulse's duration and its spectral bandwidth, the full width at the half of its maximum value (FWHM) is used. In the scope of this thesis the pulse duration will be abbreviated by Δt_{FWHM} and the spectral width by $\Delta\omega_{\mathrm{FWHM}}$.

Since most of the conventional laser systems use spherical resonator mirrors, the spatial profile of a laser beam can be described by a Gaussian. In this case the intensity profile $I(r, z)$ along the beam radius r and the axis of propagation z is given by:

$$I(r,z) = I_0 \left(\frac{W_0}{W_z}\right)^2 e^{-\frac{2r^2}{W(z)^2}}, \tag{2.7}$$

with I_0 as the intensity at the beam waist W_0. As can be seen in equation 2.7, the gaussian intensity profile is completely defined by the waist $W(z)$ and the Rayleigh range z_r:

$$W(z) = W_0\sqrt{1 + (z/z_r)^2}, \tag{2.8}$$

with

$$z_r = \pi W_0/\lambda. \tag{2.9}$$

The Rayleigh range z_r is defined as the distance to the focus at which the beam has expanded by a factor of $\sqrt{2}$. Integrating over the Gaussian intensity profile links the time-averaged intensity I_0 to the beam's total power P:

$$I_0 = \frac{2P}{\pi W_0^2}. \tag{2.10}$$

As the temporal and spectral characteristics of the electric field are linked via Fourier transform (as shown in equations 2.4 and 2.3), the pulse duration Δt_{FWHM} and the spectral width $\Delta\omega_{\mathrm{FWHM}}$ cannot vary independently of each other. There is a minimum duration–bandwidth product, representing the uncertainty principle, given by:

$$\Delta t_{\mathrm{FWHM}} \cdot \Delta\omega_{\mathrm{FWHM}} \geq 2\pi \cdot C_{\mathrm{shape}}, \tag{2.11}$$

with the pulse-shape dependent constant C_{shape}.

Assuming an ultrashort laser pulse with a Gaussian profile in time:

$$E_G(t) = E_0(t)e^{-\frac{t^2}{\sigma^2}}, \tag{2.12}$$

with σ representing the width (standard deviation) of the Gaussian distribution, the

pulse duration Δt_{FWHM} is given by

$$\Delta t_{\mathrm{FWHM}} = \sqrt{2\ln(2)}\sigma. \tag{2.13}$$

Since the Fourier transform of a Gaussian is again a Gaussian, the spectral distribution results in:

$$E_G(\omega) \propto e^{-\frac{\omega^2\sigma^2}{2}}, \tag{2.14}$$

with the spectral width $\Delta\omega_{\mathrm{FWHM}}$:

$$\Delta\omega_{\mathrm{FWHM}} = 2\sqrt{2\ln(2)}/\sigma. \tag{2.15}$$

Plugging in both, the pulse duration as well as the spectral width of the Gaussian pulse into equation 2.11 results in $C_{\mathrm{shape}} = \ln(2)/\pi \approx 0.411$ for a Gaussian pulse.

The equality of equation 2.11 holds for the case of so called "bandwidth-limited" or "Fourier-transform limited (FTL)" pulses, meaning pulses without frequency modulation. In theory, a laser pulse is Fourier limited, if it's time- $\phi(t)$ and frequency-dependent phase $\varphi(\omega)$ is constant. However, this is unrealistic from an experimental point of view, as shown by a simple Taylor expansion of both phases. The temporal phase $\phi(t)$ can be Taylor expanded into:

$$\phi(t) = \sum_{n=0}^{\infty} \frac{\phi_n}{n!} t^n = \phi_{\mathrm{CEP}} + \omega_c t + \Phi(t), \tag{2.16}$$

with the constant carrier-envelope phase (CEP) ϕ_{CEP}, defined by the offset between the maximum of the envelope $E_0(t)$ and the oscillations of the electric field with carrier frequency ω_c. For the case of broadband pulses, the carrier frequency ω_c can not be clearly defined, thus it is often assigned to either the frequency at the maximum of the spectrum or as a weighted average of all spectral components. The term $\Phi(t)$ contains all phases of order ≥ 2. The effects of those higher-order phases can best be understood by studying the instantaneous frequency $\omega(t)$ which is defined as the temporal derivative of the temporal phase:

$$\omega(t) = \frac{d}{dt}\phi(t) = \omega_c + \frac{d}{dt}\Phi(t). \tag{2.17}$$

If the term $\Phi(t)$ containing all higher-order phases vanishes ($\Phi(t) = 0$), ω_c is constant and thus the frequency of the pulse keeps unchanged within its duration. In this case the pulse is called Fourier-transform limited (FTL). For $\Phi(t) \neq 0$ the pulse is called

chirped and its electric-field oscillation changes over the duration of the pulse. If the frequency increases/decreases over time, the pulse is called up-chirped/down-chirped. An example for an up-chirped pulse is presented in the right panel of Fig.2.1(B).

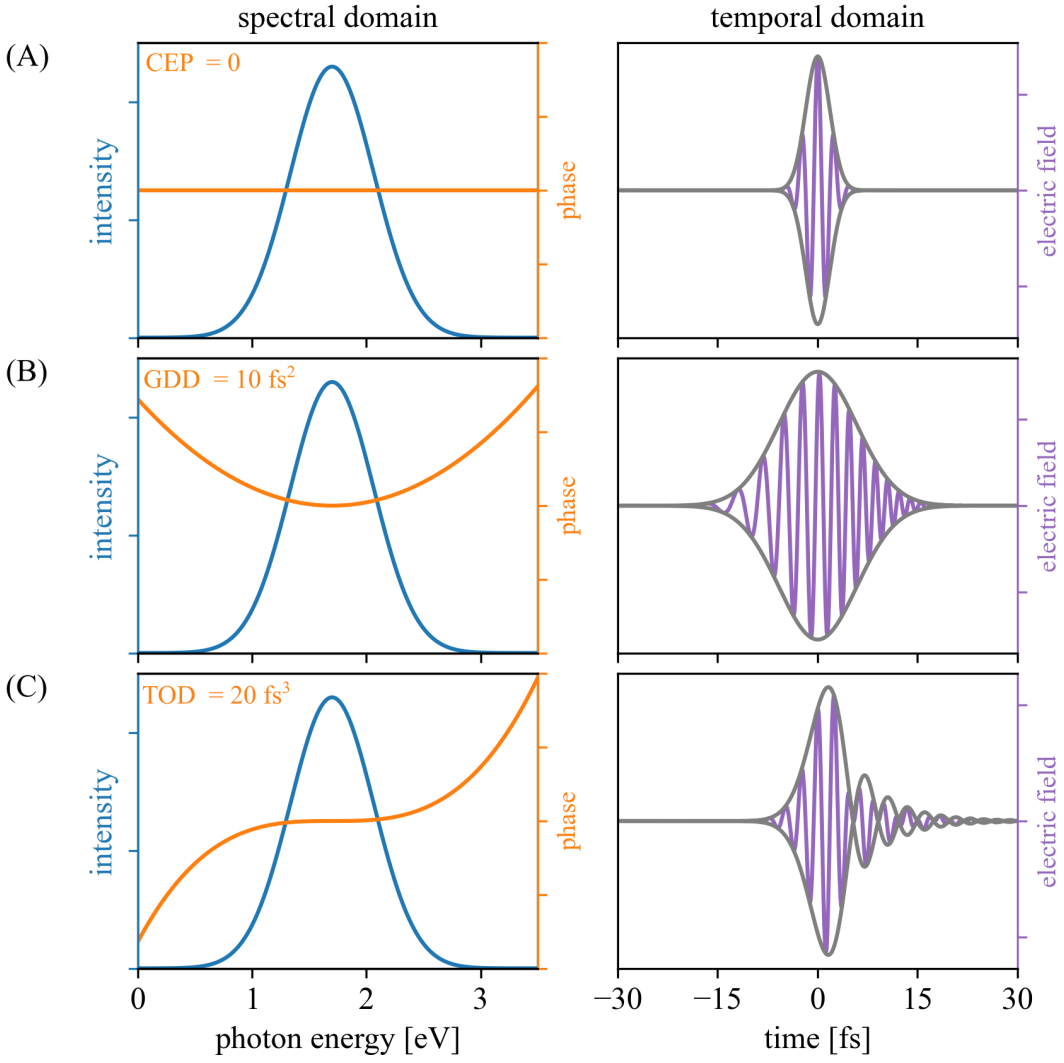

Figure 2.1.: Impact of the spectral phase on the temporal profile of ultrashort laser pulses. In the left column the spectral amplitude of a 3 fs FWHM laser pulse with a central energy of 1.70 eV is depicted in blue. Spectral phases of different orders are shown in orange. Especially for ultrashort broadband pulses, the spectral phase has a big impact on the resulting electric field in the temporal domain (see purple transients in the respective right column graphs). In addition, the electric field envelopes are depicted in gray. Fig. 2.1(A) shows a Fourier-transform limited pulse with a constant phase CEP=0. Fig. 2.1(B) shows the impact of a quadratic spectral phase. As a result, the laser pulse is up-chirped and stretched in time. Fig. 2.1(C) depicts a positive cubic phase (TOD > 0). In this case post-pulses and a small offset of the electric field envelope are introduced in the temporal domain.

A Taylor expansion of the spectral phase $\varphi(\omega)$, leads to the following:

$$\begin{aligned}\varphi(\omega) &= \sum_{n=0}^{\infty} \frac{\varphi_n}{n!}(\omega - \omega_c)^n \\ &= \varphi_{\mathrm{CEP}} + \tau_{\mathrm{GD}}(\omega - \omega_c) + \frac{\mathrm{GDD}}{2}(\omega - \omega_c)^2 + \frac{\mathrm{TOD}}{6}(\omega - \omega_c)^3 + \dots .\end{aligned} \tag{2.18}$$

The constant term φ_{CEP} is equal to the phase offset ϕ_{CEP} in the time domain. τ_{GD} is called the group delay and defines the pulse's absolute position in time. All higher-order terms induce frequency-dependent delays of subsequent spectral components, leading to a chirped pulse. The first higher-order contribution is known as the group-delay dispersion (GDD). A positive GDD leads to an up-chirped pulse, while a negative contribution of the GDD leads to a down-chirped pulse. The next order is called third-order dispersion (TOD) and leads to a generation of post-pulses for positive TOD, and pre-pulses for negative TOD. The Taylor series can be further expanded leading to fourth-order and higher terms. Since the presented orders suffice to explain the behavior of the dispersion of the experimentally used laser pulses, the spectral phase will be restricted to the aforementioned terms within the scope of this thesis.

2.1.2. Propagation effects

So far only the temporal and spectral properties of the laser pulses were introduced. This subsection deals with the propagation of these ultrashort laser pulses through matter. For this the electric field needs to be considered in its temporal and spatial dependence by the electric field vector $\mathbf{E}(t, x, y, z)$. Since only dielectric materials will be used for propagation within the scope of this thesis, external charges and currents can be neglected. A wave equation can then be derived for the electric field $\mathbf{E}(t, x, y, z)$ from the Maxwell equations, as follows:

$$\left(\nabla^2 - \frac{1}{c^2}\frac{\partial^2}{\partial t^2}\right)\mathbf{E}(t, x, y, z) = \mu_0 \frac{\partial^2}{\partial t^2}\mathbf{P}(t, x, y, z), \tag{2.19}$$

with the magnetic permeability of free space μ_0 and the polarization $\mathbf{P}(t, x, y, z)$, which describes the response of the medium. To study the impact of strong laser fields (exceeding the linear interaction with the medium), it makes sense to expand

the polarization in a Taylor series:

$$\mathbf{P}(t) = \epsilon_0 \sum_n \chi^{(n)} \mathbf{E}^n = \epsilon_0 (\chi^{(1)} \mathbf{E}(t) + \chi^{(2)} \mathbf{E}^2(t) + \chi^{(3)} \mathbf{E}^3(t) + ...), \tag{2.20}$$

where the different coefficients $\chi^{(n)}$ are the n$^{\text{th}}$-order complex-valued dielectric susceptibility tensors of the medium. One solution to equation 2.19 is a plane wave propagating in z-direction in a medium with wave vector $k(\omega)$:

$$E(\omega, z) = \mathcal{E}(\omega, 0) e^{-ik(\omega)z}. \tag{2.21}$$

The first-order term of equation 2.20, represents linear interactions of the electric field with the medium, given by:

$$\mathbf{P}(\omega) = \epsilon_0 \chi^{(1)}(\omega) \mathbf{E}(\omega), \tag{2.22}$$

with the complex valued first-order dielectric susceptibility

$$\chi^{(1)}(\omega) = \chi'(\omega) + i\chi''(\omega), \tag{2.23}$$

which is in turn directly connected to the refractive index n by the relation

$$n^2 = 1 + \chi^{(1)}(\omega). \tag{2.24}$$

While the real part of $\chi^{(1)}$ accounts for dispersion, the imaginary part accounts for the absorption of the medium. The absorption can be described by the absorption coefficient

$$\alpha(\omega) = \frac{\omega}{c} \cdot \chi''(\omega). \tag{2.25}$$

Assuming the imaginary part of the first-order dielectric susceptibility to be zero, ergo no absorption of the (transparent) medium, dispersion is still possible, as for example known from prisms. In this case the frequency-dependent refractive index leads to a frequency-dependent wave vector $k(\omega)$ with

$$k(\omega) = n(\omega) \frac{\omega}{c}. \tag{2.26}$$

Resulting in a change of the pulse's phase due to the propagation in the medium, as the phase fronts of each individual spectral component travel with the respective

phase velocity

$$v_p(\omega_0) = \left.\frac{\omega}{k}\right|_{\omega_0} = \frac{c}{n(\omega_0)}. \tag{2.27}$$

The velocity of the complete pulse is in turn defined by the group velocity via:

$$v_g = \frac{d\omega}{dk} = v_p \left(1 + \frac{\omega}{n}\frac{dn}{d\omega}\right)^{-1}. \tag{2.28}$$

How the spread of the different spectral components affects the pulse is given by the group-velocity dispersion (GVD) as

$$\mathrm{GVD}(\omega_0) = \left.\frac{d^2\omega}{dk^2}\right|_{\omega_0} = \frac{d}{d\omega}\left(\frac{1}{v_g(\omega)}\right)_{\mathcal{W}_0} = \frac{2}{c}\left(\frac{\partial n}{\partial \omega}\right)_{\mathcal{W}_0} + \frac{\omega_0}{c}\left(\frac{\partial^2 n}{\partial \omega^2}\right)_{\mathcal{W}_0}. \tag{2.29}$$

The group-velocity dispersion (GVD) is directly linked to the group-delay dispersion (GDD), via GDD = GVD · L with L being the length of the medium which the laser propagates through. Therefore, the GVD as a material property can be used to determine and control the chirp imprinted on a laser pulse. In normal-dispersive materials ($dn/d\omega > 0$), such as glass, the low-frequency components travel trough the medium faster than the high-frequency components, leading to an up-chirp of the pulse which in turn stretches the pulse in the time domain. Therefore, dispersion compensation is crucial to ensure ultrashort pulses in the time domain. To compensate for the up-chirp, materials with anomalous dispersion ($dn/d\omega < 0$) providing a down-chirp are used for pulse compression. There are two approaches to do so. One are grating compressors, where the angular dispersion is arranged such that the required negative dispersion is achieved. The second approach uses so-called chirped mirrors. These are specially designed dielectric multi-layer mirrors where the low-frequency components are reflected on the top layers of the coating, while the high-frequency components of the pulse are reflected on the bottom layers of the mirrors, leading to a negative group delay dispersion (GDD).

Now that the impact of dispersion upon the behavior of the pulse duration is clear, one can proceed with the higher-order terms of equation 2.20. Since the strength of the higher-order susceptibilities $\chi^{(n)}$ decreases with increasing order n, nonlinear higher-order effects require the presence of high field strengths. The probably most famous nonlinear effect of second order is the so-called second-harmonic generation (SHG). As the name already implies, this process converts two photons with energy $\hbar\omega_0$ to one photon with twice the energy $\hbar\omega_{\mathrm{SHG}} = 2\hbar\omega_0$, provided the propagation

medium has a non-zero second-order susceptibility $\chi^{(2)} \neq 0$. Please note, that this is only given for non-isotropic media, such as crystals. To make the process clear, an exemplary laser field given by

$$E(t) = \mathrm{Re}[E_0 e^{i\omega t}] = \frac{1}{2}\left(E_0 e^{i\omega t} + E_0^* e^{-i\omega t}\right), \tag{2.30}$$

is inserted in the second-order part of equation 2.20. This leads to:

$$\begin{aligned} \chi^{(2)} E^2(t) &= \frac{\chi^{(2)}}{4}\left(E_0^2 e^{2i\omega t} + 2E_0 E_0^* + {E_0^*}^2 e^{-2i\omega t}\right) \\ &= \frac{\chi^{(2)}}{2} E_0 E_0^* + \mathrm{Re}\left[\frac{\chi^{(2)}}{2} E_0^2 e^{i2\omega t}\right], \end{aligned} \tag{2.31}$$

which shows that the quadratic part of the nonlinear polarization has two contributions, one at zero frequency and one that oscillates with double the initial frequency. Taking the wave equation 2.19 into consideration, the zero-frequency term vanishes, while the 2ω-component does not. Therefore, electromagnetic radiation with twice the frequency is emitted. In this thesis beta-barium borate (BBO) was used as a nonlinear crystal for SHG.

An important third-order nonlinear effect which plays a role within the scope of this thesis is the optical Kerr effect which is the source of self-focusing, as well as self-phase modulation (SPM). These third-order nonlinearities are induced by the χ^3 susceptibility and result in the medium to exhibiting an intensity-dependent refractive index, such that

$$n(x, y, z, t) = n_0 + n_2 I(x, y, z, t). \tag{2.32}$$

In the process of self-focusing, the space- and time-dependent refractive index $n(x, y, z, t)$ induces a lensing effect, due to the spatial intensity profile of the laser beam. This process is taken advantage of in femtosecond Ti:Sa laser oscillators to ensure the cavity favors high-power pulsed operation over cw-operation. The so-called Kerr lens mode-locking technique enables passive mode-locking since no active element is needed (see chapter 3.1 for more details on the laser system). Self-phase modulation (SPM) induces spectral broadening of the laser pulse while propagating trough the medium. This is used within the scope of this work to spectrally broaden the laser pulse provided from the Ti:Sa laser system in a gas-filled hollow-core fiber (see chapter 3.2). By focusing the short pulses into a glass capillary, the temporal intensity profile of the laser pulse induces a time-dependent refractive index of the

gas, leading to a modulation of the pulse's phase. Assuming a Gaussian intensity profile $I_{\text{Gaussian}}(t) = I_0 e^{-t^2/\tau^2}$, the instantaneous frequency $\omega(t)$ as given by equation 2.17 can be expressed as:

$$\omega(t) = \omega_c - \frac{\omega_c}{c}\frac{d}{dt}n(t) = \omega_c + \frac{\omega_c}{c}\frac{2I_0 n_2}{\tau^2} t e^{-\frac{t^2}{\tau^2}}. \tag{2.33}$$

One can see that new frequency components with lower/higher frequency compared to ω_c are produced in the leading/trailing edges of the pulse. This nonlinear process is used in the experiment to generate broadband pulses. These are subsequently temporally compressed with a chirped-mirror compressor leading to spectrally broad but at the same time temporally short laser pulses.

2.2. Transient absorption spectroscopy

Now that the mathematical description of ultrashort laser pulses and their interaction with matter is layed out, this section introduces the measurement technique used within the scope of this thesis – namely transient absorption spectroscopy. The observable of interest is the spectral intensity distribution of light after propagating through a target as a function of experimental control parameters, such as the time delay between two pulses or the light intensity. By measuring the transient spectra, not only macroscopic but also microscopic target properties such as the laser-induced dipole moment can be determined and controlled.

2.2.1. The link between macroscopic and microscopic quantities

As described in section 2.1.2, an electric field $E(t)$ passing an isotropic medium will induce a polarization response $\mathbf{P}$ in the medium. Taking only the linear relation into account, the polarization is then defined by equation 2.22, which is already the macroscopic description of the polarization.

However, there is also the possibility of a microscopic derivation. In this case the electric field shifts the electrons relative to the nuclei on the atomic and molecular level, thereby inducing a dipole moment $\mathbf{d}$

$$\mathbf{d} = q \cdot \mathbf{r}, \tag{2.34}$$

with the charge q and the displacement $\mathbf{r}$. To show the back action of the atoms on

the incoming field - leading to absorption - the microscopic dipole can be connected to the propagation of electromagnetic waves via the macroscopic polarization

$$\mathbf{P} = \rho \cdot \mathbf{d}, \tag{2.35}$$

with the medium density ρ. Using the wave equation 2.19 and restricting the fields $\mathbf{E}(t, x, y, z)$ and $\mathbf{P}(t, x, y, z)$ to be linearly polarized plane waves propagating in z-direction, equation 2.19 simplifies to

$$\left(\frac{\partial^2}{\partial z^2} - \frac{1}{c^2}\frac{\partial^2}{\partial t^2}\right)\mathcal{E}(t, z)e^{i(kz-\omega t)} = \mu_0 \frac{\partial^2}{\partial t^2}\mathcal{P}(t, z)e^{i(kz-\omega t)}. \tag{2.36}$$

The time derivatives of this simplified wave equation can be solved in the spectral domain using Fourier transformation by considering the following relation

$$\mathcal{F}\left\{\frac{\partial}{\partial t}\ \mathcal{E}(t)\right\} \propto \int dt\ e^{-i\omega t}\ \frac{\partial}{\partial t}\ \mathcal{E}(t) = i\omega \int dt\ e^{-i\omega t}\ \mathcal{E}(t) = i\omega\ \mathcal{E}(\omega). \tag{2.37}$$

In addition, the spatial derivative is performed in the *slowly varying envelope approximation*. This assumes that the field envelope $\mathcal{E}(z)$ is weakly dependent on z resulting in $\partial^2/\partial z^2\ \mathcal{E}(z) \to 0$. Using both simplification equation 2.36 reduces to

$$2ik\frac{\partial}{\partial z}\mathcal{E}(\omega, z) = -\mu_0\omega^2\mathcal{P}(\omega, z). \tag{2.38}$$

Combining equation 2.38 with 2.35 the effect of the microscopic dipoles onto the macroscopic field gets clear

$$\frac{\partial}{\partial z}\mathcal{E}(\omega, z) = i\omega\frac{\rho}{2\epsilon_0 c}d(\omega, z). \tag{2.39}$$

2.2.2. Optical density

As already emphasized in the introduction of this section, the aim of this work is to access the microscopic molecular dipoles and their dynamics by measuring the spectral distribution of light after propagation through the target via transient absorption spectroscopy. In this regime the measure of choice is the optical density (OD) which is defined by

$$OD(\omega) = -\log_{10}\left(\frac{I(\omega)}{I(\omega_0)}\right), \tag{2.40}$$

with the spectral intensities measured before $I(\omega_0)$ and after $I(\omega)$ the target. The results from above can be linked to the optical density. Therefore, the medium of propagation is assumed to be homogeneous, meaning that both the density ρ, as well as the dipole moments are independent of the propagation axis z: $\rho(z) = \rho$ and $d(\omega, z) = d(\omega)$. Under this assumption propagation effects in the medium are neglected. To obtain the spectral intensity $I(\omega)$ after a target with length L the integration of equation 2.39 is performed

$$\mathcal{E}(\omega, L) = \mathcal{E}(\omega, 0) + \frac{i\omega}{2\epsilon_0 c} \int_0^L dz \rho(z) d(\omega, z) \approx \mathcal{E}(\omega, 0) + i\frac{\omega \rho L}{2\epsilon_0 c} d(\omega) = \mathcal{E}_{in} + i\mathcal{E}_{gen}, \quad (2.41)$$

where $\mathcal{E}_{in}$ denote the incoming and $\mathcal{E}_{gen}$ the generated electric field. It can be directly seen that the generated field is phase-shifted by $\pi/2$ compared to the incoming electric field. The absorption of light can thus be understood as an interference phenomenon between the incoming electric field and the induced dipole emission of the target medium (free-induction decay). Using the above expressions, the spectral intensity can be written as

$$I(\omega) = |\mathcal{E}(\omega)|^2 = |\mathcal{E}_{in}|^2 - i\mathcal{E}_{in}\mathcal{E}^*_{gen} + i\mathcal{E}^*_{in}\mathcal{E}_{gen} + |\mathcal{E}_{gen}|^2. \quad (2.42)$$

Since the intensity of the generated signal is weak compared to the incoming radiation, the term $|\mathcal{E}_{gen}|^2$ can be neglected, leading to a heterodyne detection scheme of the generated signal. Therefore, the intensity ratio between outgoing and incoming intensities is given by

$$\frac{I(\omega)}{I_0(\omega)} = \frac{|\mathcal{E}_{in}|^2 - i\mathcal{E}_{in}\mathcal{E}^*_{gen} + i\mathcal{E}^*_{in}\mathcal{E}_{gen}}{|\mathcal{E}_{in}|^2} = 1 - i\left(\frac{\mathcal{E}^*_{gen}}{\mathcal{E}^*_{in}} - \frac{\mathcal{E}_{gen}}{\mathcal{E}_{in}}\right) = 1 - 2\,\mathrm{Im}\left(\frac{\mathcal{E}_{gen}}{\mathcal{E}_{in}}\right). \quad (2.43)$$

Using the results of equation 2.41 and 2.43, as well as the approximation for the logarithm $ln(1 - x) \approx -x$, the optical density can be written as

$$OD(\omega) = -\log_{10}\left(\frac{I(\omega)}{I(\omega_0)}\right) = \frac{\rho L}{ln(10)} \frac{\omega}{\epsilon_0 c}\,\mathrm{Im}\left(\frac{d(\omega)}{\mathcal{E}_{in}(\omega)}\right). \quad (2.44)$$

This shows that by measuring the optical density one has direct access to the dipole moment of the system. Looking from a time-domain perspective, the dipole response is recorded in a time-integrated manner, which is convenient, since measuring the dipole response in real time is yet not possible. At the same time this means that the time resolution in a transient absorption measurements only depends on the chosen

time-delay steps, while the real time evolution of the dipole moment is encoded in the spectral domain.

2.2.3. Beer-Lambert's law

While the above presented expression of the optical density is valid for arbitrary nonlinear relationships between the incoming electric field and the induced dipole emission, it can be further simplified in the weak-field limit, where the relation between macroscopic polarization and the electric field is linear:

$$\mathbf{P}(\omega) = \rho d(\omega, z) = \epsilon_0 \chi^{(1)}(\omega)\mathbf{E}(\omega). \tag{2.45}$$

Using this linear relation the integration of equation 2.38 simplifies to

$$\frac{\partial}{\partial z}\mathcal{E}(\omega, z) = i\frac{\omega}{2c}\chi^{(1)}(\omega)\mathcal{E}(\omega, z), \tag{2.46}$$

resulting in the following expression for the electric field:

$$\mathcal{E}(\omega, z) = \mathcal{E}_{in}(\omega)\exp\left(i\frac{\omega}{2c}\chi^{(1)}(\omega)z\right). \tag{2.47}$$

Calculating the intensity, the famous *Beer-Lambert's law* can be obtained

$$I(\omega, z) = \frac{1}{2}\epsilon_0 c|\mathcal{E}(\omega, z)|^2 = I_0 e^{-\sigma(\omega)\rho z}, \tag{2.48}$$

with the microscopic absorption cross section $\sigma(\omega)$:

$$\sigma(\omega) = \frac{\omega}{\epsilon_0 c}\,\mathrm{Im}\left(\frac{d(\omega)}{\mathcal{E}_{in}(\omega)}\right). \tag{2.49}$$

2.2.4. The time-dependent dipole response

In this chapter, microscopic target properties were connected to the measurement observables. Equation 2.44 thereby directly shows how the optical density is related to the Fourier transform (FT) of the system's time-dependent dipole moment:

$$OD(\omega) \propto \omega\,\mathrm{Im}\left(\frac{d(\omega)}{E_{in}(\omega)}\right) = \omega\,\mathrm{Im}\left(\frac{FT[d(t)]}{FT[\mathcal{E}_{in}(t)]}\right). \tag{2.50}$$

By measuring the optical density one should therefore be able to reconstruct the time-dependent dipole moment. Now the question arises, which constraints on the measurement data have to be made such that this reconstruction is possible? The crucial point is that the incoming pulse $\mathcal{E}_{in}(t)$ needs to be sufficiently short in the time domain, such that it can be described as a δ-function. Otherwise the causality presented in equation 2.50 does not apply. A *delta* pulse ensures that there is no dipole emission prior to the excitation such that $d(t < 0) = 0$. Under this condition the time-dependent dipole can be reconstructed, as was demonstrated in helium under the presence of a second perturbating electric field [32]:

$$d(t) \propto FT^{-1}[iOD(\omega)](t) = \frac{1}{\sqrt{2\pi}} \int iOD(\omega) e^{i\omega t} d\omega \text{ for } t > 0. \tag{2.51}$$

Thus the reconstruction of the temporal dipole from measurement data is, in principle, feasible provided the laser pulses used for the experiment are sufficiently short in time.

2.3. Quantum dynamics of laser-coupled few-level systems

For the case of non-relativistic quantum mechanics, the time-dependent Schrödinger equation describes the dynamics of any quantum system by

$$i\hbar \frac{\partial}{\partial t} |\psi(t)\rangle = \mathcal{H} |\psi(t)\rangle , \tag{2.52}$$

with the wave function $|\psi(t)\rangle$ and the total Hamiltonian operator $\mathcal{H}$. While the wave function can be represented as a sum of the complex-valued time-dependent state coefficients $c_i(t)$ and the spatial eigenstates of the system $|\Phi_i\rangle$ via

$$|\psi(t)\rangle = \sum_{i=1}^{n} c_i(t) |\Phi_i\rangle , \tag{2.53}$$

the total Hamiltonian operator can be split into the Hamiltonian of the unperturbed time-independent system $\mathcal{H}_0$ and the light-matter interaction operator $\mathcal{H}_{int}$:

$$\mathcal{H} = \mathcal{H}_0 + \mathcal{H}_{int}. \tag{2.54}$$

In the dipole approximation the interaction operator is given by

$$\mathcal{H}_{int} = \hat{d} \cdot E(t), \tag{2.55}$$

with the dipole operator $\hat{d}$ and the electric field $E(t)$. The total Hamiltonian is therefore represented by an n x n matrix with the eigenenergies $E_i = \langle \Phi_i | \mathcal{H}_0 | \Phi_i \rangle$ on the diagonal entries and the couplings $\mathcal{H}_{int_{ij}} = \langle \Phi_i | \mathcal{H}_{int} | \Phi_j \rangle$ on the off-diagonals. Referring to equation 2.55 the off-diagonal matrix elements $\mathcal{H}_{int_{ij}}$ evaluate to

$$\mathcal{H}_{int_{ij}} = \langle \Phi_i | \mathcal{H}_{int} | \Phi_j \rangle = \langle \Phi_i | \hat{d} | \Phi_j \rangle E(t) = d_{ij} E(t), \tag{2.56}$$

with dipole matrix elements d_{ij}.

The time-dependent evolution of the system is solved by determining the evolution of the n state coefficients $c_i(t)$ numerically via a split-step algorithm [57]. Under the assumption that the Hamiltonian $\mathcal{H}$ is constant during each time step Δt, this routine solves iteratively the equations of motion for every step by changing between the diagonalized Hilbert spaces of the unperturbed Hamiltonian $\mathcal{H}_0$ and the interaction Hamiltonian $\mathcal{H}_{int}$ as follows:

1. Field-free evolution:
$$c_i(t + \Delta t) = e^{-\frac{i}{\hbar} E_i \Delta t} c_i(t) \tag{2.57}$$

2. Transformation into the eigensystem of the interaction. The transformation matrix U is given by the diagonalization of $\mathcal{H}_{int}$.

$$\tilde{\mathcal{H}}_{int} = \mathrm{diag}(\tilde{\mathcal{H}}_{int_1} ... \tilde{\mathcal{H}}_{int_n}) = U^\dagger \mathcal{H}_{int} U \,, \quad |\tilde{\psi}\rangle = \hat{U}^\dagger |\psi\rangle \tag{2.58}$$

3. Propagation in the interaction basis:

$$\tilde{c}_i(t + \Delta t) = e^{-\frac{i}{\hbar} \tilde{\mathcal{H}}_{int_i} \Delta t} \tilde{c}_i(t) \tag{2.59}$$

4. Transformation back into the energy basis:

$$|\psi\rangle = U |\tilde{\psi}\rangle \tag{2.60}$$

After these 4 points the initial state vector has been propagated for one time step Δt in both domains. Assuming $t_k = k \cdot \Delta t$ as the total propagation time, this sequence

of operations needs to be performed for each of the k steps, while updating the state vector after each time step.

Having determined the state coefficients $c_i(t)$ the time-dependent dipole response $d(t)$ of the system can be calculated via

$$d(t) = \langle\psi(t)|\,\hat{d}\,|\psi(t)\rangle = \sum_{m,n} d_{nm} c_n(t) c_m^*(t) + c.c. \tag{2.61}$$

where $d_{nm} = \langle\Phi_m|\,\hat{d}\,|\Phi_n\rangle$.

By Fourier transforming the dipole response $d(t)$ in addition, the dipole spectrum $d(\omega)$ can be obtained which allows, together with the spectral electric field, the calculation of the absorption cross section. This is in turn proportional to the optical density which was previously introduced.

To facilitate the calculations, atomic units were used for the simulations (see Appendix A.1).

2.4. Molecules in the liquid phase

After introducing the light-matter interaction and how to link the measurement observable OD to the microscopic light-induced dipole moment, this section focuses on the target of interest, namely aluminum phthalocyanine chloride complexes dissolved in a mixture of water and ethanol. Therefore, it will start with the basic concept of molecular orbital theory to lay out the physical properties of molecules in general, followed by a short overview of absorption band structures in molecules and ending with the complex molecule aluminum phthalocyanine chloride.

2.4.1. Molecular orbital theory

To describe bonding and excitation in molecules, a short summary of molecular orbital theory is presented here. The properties are introduced through the example of a diatomic, homo-nuclear molecule. One of the methods used, especially for larger molecules that cannot be treated exactly is the LCAO approximation, where the molecular wave function is composed of *linear combinations of the atomic orbitals* of the atoms that form the molecule. Since the absolute square of the wave function ψ represents the spatial probability density distribution of the electron – which is equivalent to the time-averaged classical orbitals – the molecular wave function is

called molecular orbital. The molecular wave function of a molecule consisting of two identical atoms can therefore be written, as the linear combination of the two atomic wave functions:

$$\psi(\mathbf{r}, R) = c_1\phi_A(\mathbf{r}_A) + c_2\phi_B(\mathbf{r}_B), \tag{2.62}$$

with atomic valence orbitals ϕ_i of the atoms and coefficients c_i. The wave function should be normalized for an arbitrary inter-nuclear separation R. This demands that the probability distribution is equal to 1:

$$\int \psi^2 d\mathbf{r} = c_1^2 \int |\phi_A(\mathbf{r}_A)|^2 d\mathbf{r}_A + c_2^2 \int |\phi_B(\mathbf{r}_B)|^2 d\mathbf{r}_B + 2c_1c_2 \int \phi_A(\mathbf{r}_A)\phi_B(\mathbf{r}_B) d\mathbf{r} = 1. \tag{2.63}$$

The integration is here performed over the coordinates of the electron. As the atomic orbitals are already normalized, the first two integrals in equation 2.63 are equal to 1. This leads to the following condition on the coefficients c_i of the molecular wave function:

$$c_1^2 + c_2^2 + 2c_1c_2S_{AB} = 1, \tag{2.64}$$

with the overlap integral

$$S_{AB} = \int \phi_A(\mathbf{r}_A)\phi_B(\mathbf{r}_B) d\mathbf{r}, \tag{2.65}$$

which depends on the spatial overlap of the two atomic wave functions. Due to the symmetry argument of a diatomic, homo-nuclear molecule the condition $|c_1|^2 = |c_2|^2$ applies. In addition the molecular wave function has to be either symmetric or anti-symmetric with respect to the exchange of the two atomic orbitals. This postulates $c_1 = \pm c_2$ which results in the two normalized molecular wave functions:

$$\psi_\pm = \frac{1}{\sqrt{2(1 \pm S_{AB})}}(\phi_A \pm \phi_B). \tag{2.66}$$

In the case of two 1s-orbitals, the linear combination by addition (ψ_+), therefore, leads to a constructive interference between the wave functions and thus to a higher electron density in between the two atoms, thereby forming a bonding molecular orbital. The linear combination by subtraction (ψ_-) in turn leads to destructive interference, forming the anti-bonding molecular orbitals. Anti-bonding molecular orbitals are by convention marked with the superscript * (cf. Fig. 2.2). Please note, in general, the overlap integral S_{AB} determines whether a specific linear combination ($\psi_\pm$) leads to the formation of a bonding, or anti-bonding orbital (cf. Fig. 2.3).

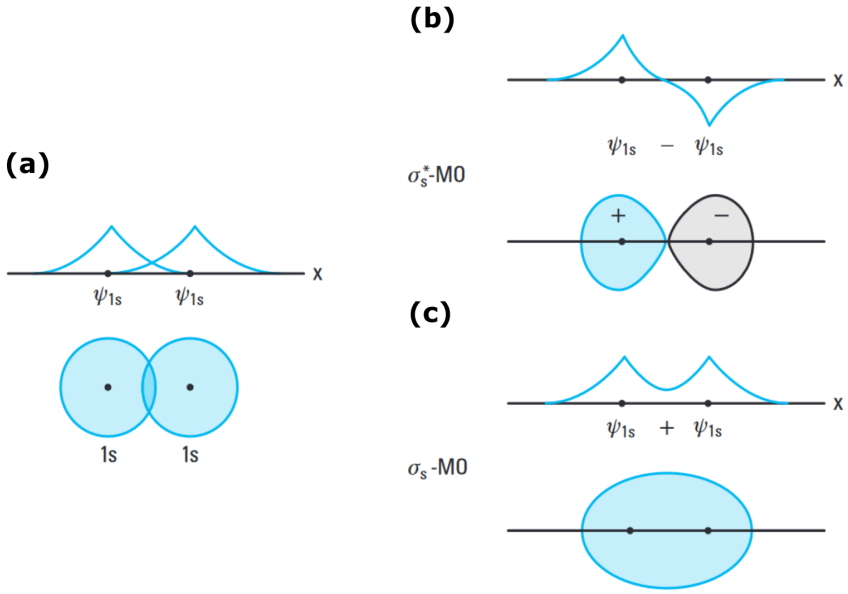

Figure 2.2.: Linear combination of two 1s-atomic orbitals forming the molecular σ_s-orbitals. Depicted are the two individual wave functions Ψ_{1s}, as well as the probability density of the electron. (a) depicts the two individual wave functions of the 1s hydrogen orbital Ψ_{1s} and corresponding electron density. The linear combinations of the two wave functions are shown in panels (b) and (c). While (b) shows the linear combination Ψ_-, which results in the anti-bonding σ_s^* molecular orbital, (c) depicts the combination Ψ_+ leading to the bonding σ_s-MO. Image adapted from [56].

Using the LCAO method and expanding it to all atomic orbitals one key rule needs to be taken into consideration: Only atomic orbitals with similar energy and the same symmetry along the internuclear axis can form a molecular orbital, since for the combination of two orbitals with different symmetry (as for example p_x and p_z) the overlap integral S_{12} equals zero. Is the created molecular orbital rotationally symmetric to the internuclear axis, it is called a σ-orbital, while molecular orbitals that do not fulfill this condition are referred to as π-orbitals. The optical transition which will be investigated in this thesis is a transition between π- and π^*-orbitals. In the skeletal formula notation which is common in chemistry, single bonds which consist of a σ-bond are denoted with a dash ("–"), e.g. the bond between two carbon atoms by "C–C", while a double bond is denoted with a double dash ("=") (e.g. the double bond between two carbon atoms "C=C") and consists of a σ- and a π-bond. The electrons involved in a π-bond are spatially delocalized compared to the internuclear axis, as can be seen on the exemplary binding π_z molecular orbital in Figure 2.3.

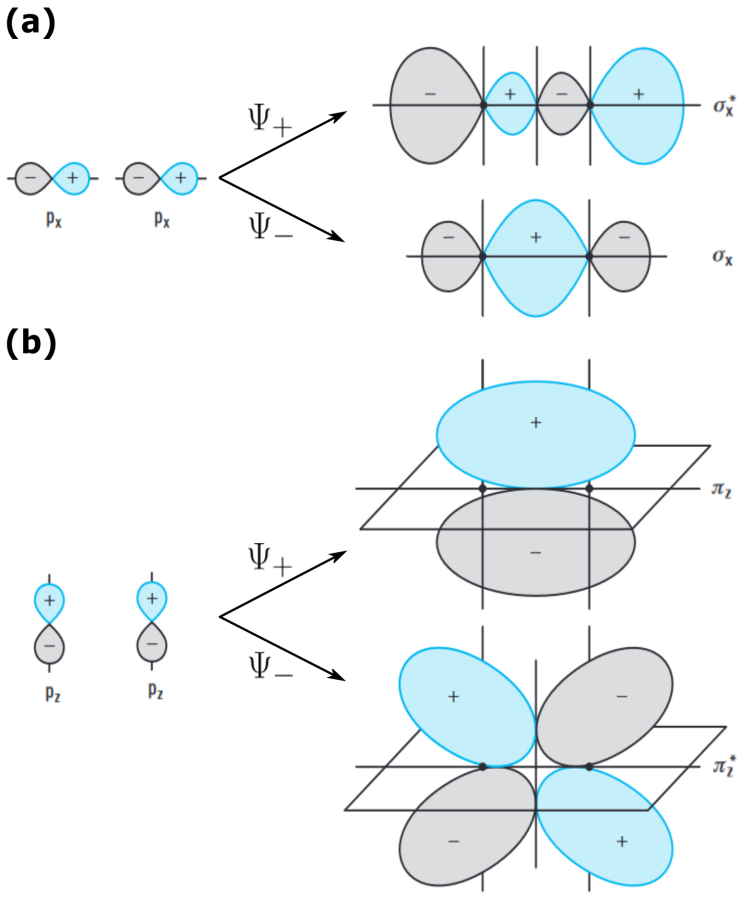

Figure 2.3.: Molecular orbitals formed by $1p$ atomic orbitals p_x and p_z. The internuclear axis in this scheme is the x-axis. (a) shows the two possible linear combinations of two p_x atomic orbitals, leading to the two σ molecular orbitals: σ_x^* (anti-bonding) and σ_x (bonding). The two linear combinations of the p_z-orbitals are depicted in panel (b). They lead to the formation of π molecular orbitals π_z (bonding) and π_z^* (anti-bonding). Image adapted from [56].

With increasing number of atoms forming a molecule, the complexity of the molecular orbitals spreading along the molecule increases. A rather simple molecular system with a ring structure similar to the later-on investigated phthalocyanine, is the benzene molecule. Benzene (C_6H_6) is an organic chemical compound which is composed of six carbon atoms joined in a planar ring with one hydrogen attached to every carbon. The benzene ring consists of alternating single and double bonds, also known as conjugated bonds. The, thereby, involved π-electrons are fully delocalized over the entire ring structure. To give an insight in how a π - π^* electron transition changes the electron-density of complex molecular ring structures, a simplified picture of benzene is shown in Figure 2.4.

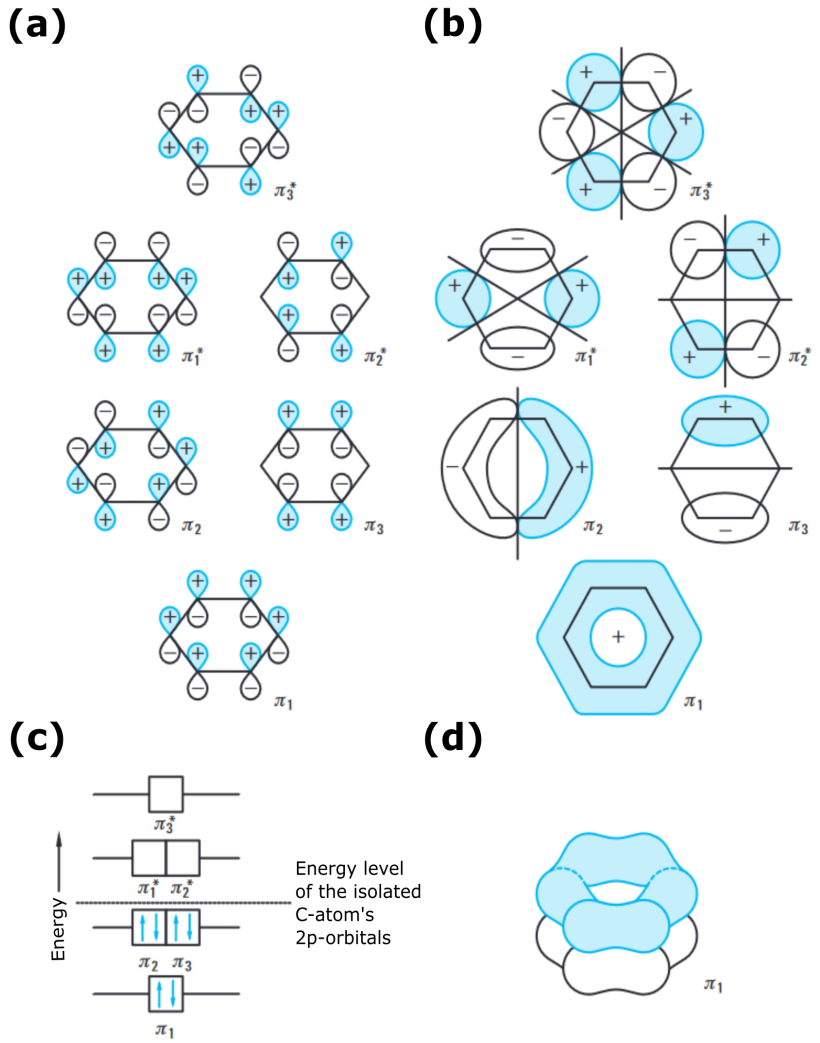

Figure 2.4.: π molecular orbitals of the benzene molecule. (a) depicts the p atomic orbitals of the benzene molecule that are suitable for the combination into the π molecular orbitals shown in panel (b). (c) depicts the energy level scheme of benzene's π molecular orbitals and (d) is an illustration of the 3D electronic density of the delocalized π_1 molecular orbital. Image adapted from [56].

Electronic transitions Electronic transitions can in general be performed between the binding σ- and π-orbitals as well as the n-orbitals of the free electron pairs into the empty antibonding orbitals σ^* and π^*. The possible transitions are therefore called $\sigma \rightarrow \sigma^*$, $\pi \rightarrow \pi^*$, $n \rightarrow \pi^*$ and $n \rightarrow \sigma^*$. A simplified picture of the electronic levels named after the involved molecular orbitals and possible electronic transitions are depicted in Figure 2.5.

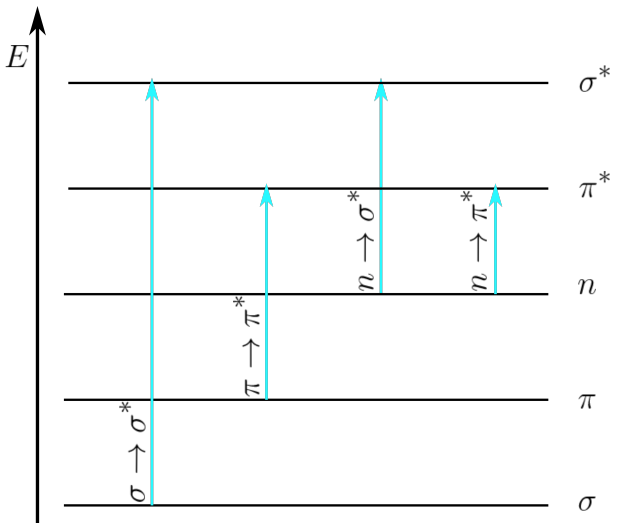

Figure 2.5.: Energetic level structure of molecular orbitals. Dipole allowed electronic transition between the molecular orbitals are depicted by blue arrows. Note: This scheme is a very simplified picture and only has the task to illustrate the relative energy level ordering of the molecular orbitals and the possible electronic transitions. The absolute energy level spacings are molecule specific and can be further degenerated.

A list of the different nomenclatures for electronic transitions in molecules can be found in the Appendix A.2. Within the scope of this thesis the nomenclature by Kasha [58] based on the molecular orbitals will be used.

Absorption band structure in molecules So far only electronic transitions under the assumption of a rigid core structure were considered. Now, in addition the oscillations/vibrations of the atomic cores shall be taken into consideration. For this, the Born-Oppenheimer (BO) approximation can be used, considering that the molecular energy is a sum of independent terms given by:

$$E_{total} = E_{electronic} + E_{vibrational} + E_{rotational} + E_{nuclear\ spin}. \tag{2.67}$$

Based on the fact that the nuclei are much heavier than the electrons, the general assumption can be made to treat the wave functions of the atomic nuclei and electrons in a molecule separately. Due to the larger mass of a nucleus compared to an electron, the coordinates of the nuclei are considered as fixed, while the coordinates of the electrons are dynamic. The terms in equation 2.67 are of different orders of magnitude, such that the energy term associated with nuclear spin is often omitted:

$$\Delta E_{electronic} >> \Delta E_{vibrational} >> \Delta E_{rotational} >> \Delta E_{nuclear\ spin}. \tag{2.68}$$

In this paragraph the electronic bands of molecules will be treated. In general this refers to electronic transitions which are accompanied by changes in the molecular vibrational state. Looking at the absorption of light by a molecule, an electronic transition from the ground state of a molecule with electronic energy E''_{el} with the vibrational quantum number $v'' = 0$ into an electronically excited state leads not to a single absorption line, but to a multitude of lines, known as an absorption band. The band structure arises since the electronic transition is accompanied by a change in the vibrational quantum number $E''_{el}(v'') \rightarrow E'_{el}(v')$. Furthermore these vibronical transitions are superimposed by a rotational structure. (Note: Since rotational transitions cannot be observed in liquid phase targets, only the vibrational transitions will be considered in the following.)

In the classical model of the Franck-Condon principle, the absorption of a photon occurs within a time interval that is short compared to the vibrational period T_{vib} of the molecule. Therefore, electronic transitions between the two states can be represented by vertical arrows in a potential energy diagram (cf. Fig. 2.6). In turn, this means that the internuclear distance R keeps unchanged during the transition.

The intensity of the individual vibrational transitions within an electronic transition is governed by the Franck–Condon factor (FCF):

$$FCF(v_i, v_k) = \left| \int \psi_{vib}(v_i)\psi_{vib}(v_k)dR \right|^2, \tag{2.69}$$

which in turn depends on the overlap of the vibrational wave functions $\psi_{vib}(v_i)$ and $\psi_{vib}(v_k)$ of the upper and lower electronic states.

While the probability for a transition $v' \leftrightarrow v''$ is given by the Franck-Condon factor, the ratio

$$\mathcal{P}(R)dR = \frac{\psi'_{vib}(R)\psi''_{vib}dR}{\int \psi'_{vib}(R)\psi'_{vib}dR} \tag{2.70}$$

defines the probability that the transitions takes place in the interval dR around R. Therefore, if the two potential curves $E'_{pot}(R)$ and $E''_{pot}(R)$ have a similar R-dependence and equilibrium distances $R'_e \approx R''_e$, the Franck-Condon factor is maximal for transitions with $\Delta v = 0$ and small for $\Delta v \neq 0$. The larger the shift between the equilibrium distances R'_e and R''_e of the two electronic levels, the larger becomes the difference for Δv for the maximum Franck-Condon factor. Since the probabilities of the vibrational transitions are not equal for the vibronic states, a fine structure in the electronic absorption spectrum emerges. Three graphical examples are shown in Figure 2.6.

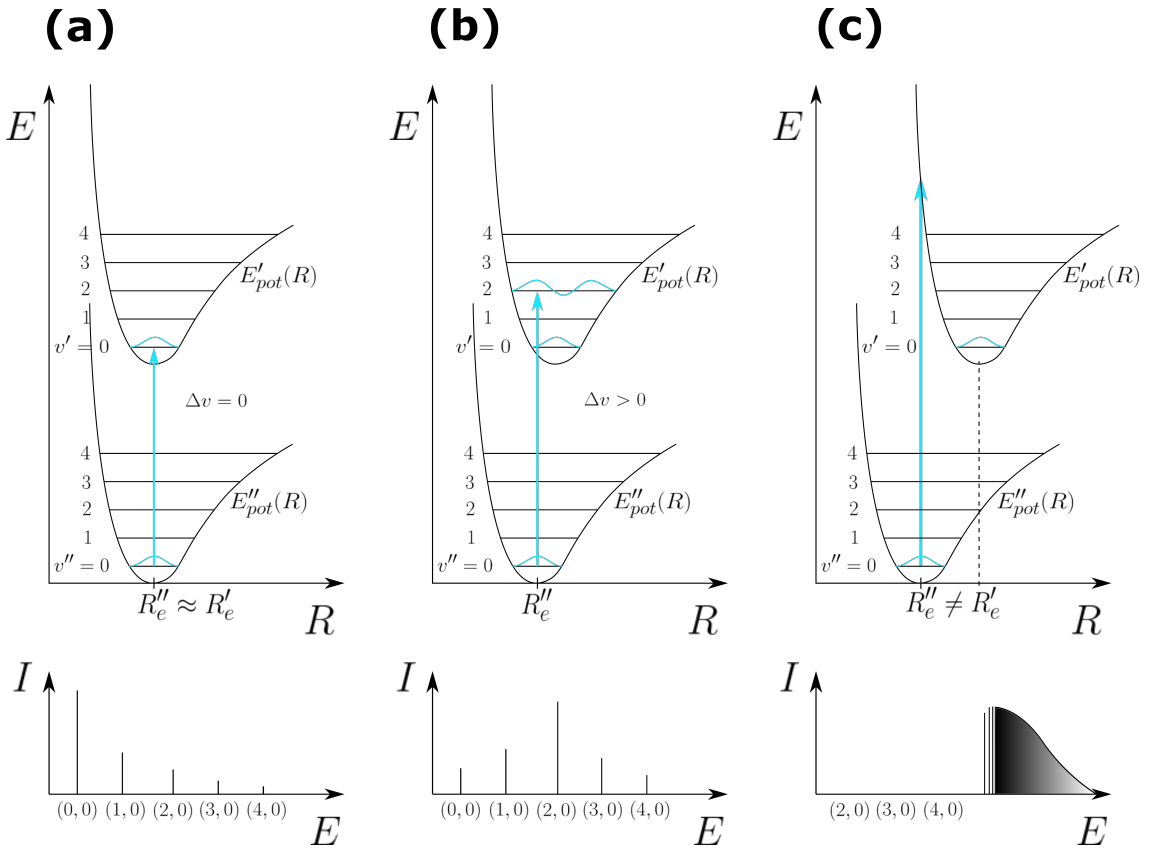

Figure 2.6.: Illustration of the Franck-Condon principle for vertical transitions with $\Delta v = 0$ (a) and $\Delta v > 0$ (b) and $\Delta v >> 0$(c) in case of potential curves $E''_{pot}(R)$ and $E'_{pot}(R)$ with $R''_e = R'_e$ (a), $R''_e < R'_e$ (b) and $R''_e << R'_e$. Dependend on the behaviour of the nuclear distance R at an electronic transition, the intensity ratio of the vibronic bands which participate within the electronic transition change. Only the transition which starts at the area of the highest probability density in state $v' = 0$ is depicted (by a light-blue arrow). In the spectrum this results in the maximum intensity for the transition (0,0) for $R'_e \approx R''_e$ depicted in panel (a). In (b) the highest intensity is reached for the transition (2,0). Is the displacement of both potential curves large enough, the highers contribution can also be given by the dissociation, as shown in (c).

$\pi \rightarrow \pi^*$ transitions show a pronounced vibrational structure. The reason for this is the following: Since the excitation occurs between bound states of the molecule in which the bond as such remains, also the probability of the molecule to oscillate sustains. This is the case because the delocalized π-orbitals are not relevant for the cohesion of the molecule. This can also be clearly seen by taking a look at the UV-VIS absorption spectrum of AlClPc depicted in Figure 2.8.

The vibrational structures are characteristic for each molecule and highly dependent on the molecule's symmetry. They can be best observed when molecules are in the gas phase, but remain also in liquid and condensed phase. Spectral lines associated to rotations and vibrations are though broadened in liquids and solids. Especially

absorption features caused by rotational excitations of the molecule keep hidden in the liquid and condensed phase due to the line- respectively bandwidth broadening so that rotational features are smeared out or completely hidden. [59]

When dissolving molecules the solvent can have an influence on the central energy and the substructure of the absorption band. The effects of the solvent upon the absorbtion spectrum of AlClPc are presented in chapter 4.

2.4.2. Aluminum Phthalocyanine Choride (AlClPc)

Now that the basis of how molecular bonds are formed and how molecules in general can be treated while absorbing light is laid out, this subsection focuses on the target of interest - namely aluminum phthalocyanine chloride ($C_{32}H_{16}AlClN_8$, abbreviated in the following by AlClPc).

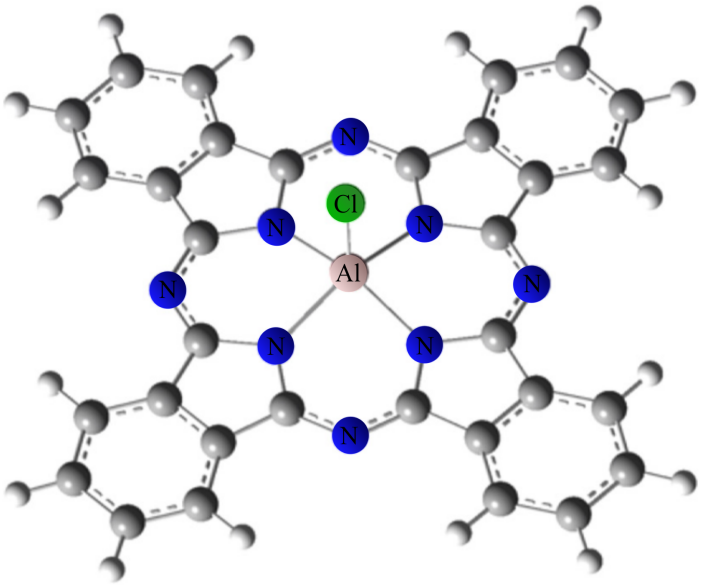

Figure 2.7.: Molecular structure of AlClPc, with conventional color scheme, carbon in gray, hydrogen in white, nitrogen in blue, aluminum in light pink and chlorine in green. The macrocyclic phthalocyanine ring lies in a plane with the aluminum atom in its center, while the chlorine sticks out perpendicular to the plane. Molecular single bonds are represented by sticks, while delocalized π-electrons originating from the double bonds are represented as dotted lines. Image adapted from [60].

AlClPc is a versatile molecule which, after its discovery was first used as a blue dye. Nowadays, phthalocyanines in general enjoy a variety of industrial and medical applications such as in solar cells [45, 46] and photo-dynamic therapy (PDT) of tumors

[47–49] due to their outstanding electronic and optical properties. Since phthalocyanines are thermally and chemically stable, they can sustain intense electromagnetic radiation to some extent, which makes them good candidates for the envisioned experiment with strong-fields in the liquid phase.

AlClPc consists of a phthalocyanine ring, which is centrally substituted with an aluminum atom, in turn bound to a chlorine atom. Its structure is dominated by a macrocyclic phthalocyanine ring with the aluminum atom in its center and the chlorine sticking out of the plane (see Figure 2.7). By looking at the molecular structure one notices straight away the amount of π-electrons delocalized over the phthalocyanine ring. It's these 18 delocalized π-electrons that govern the electronic absorption spectrum of AlClPc. The UV-VIS absorption spectrum of in ethanol dissolved AlClPc is depicted in Figure 2.8.

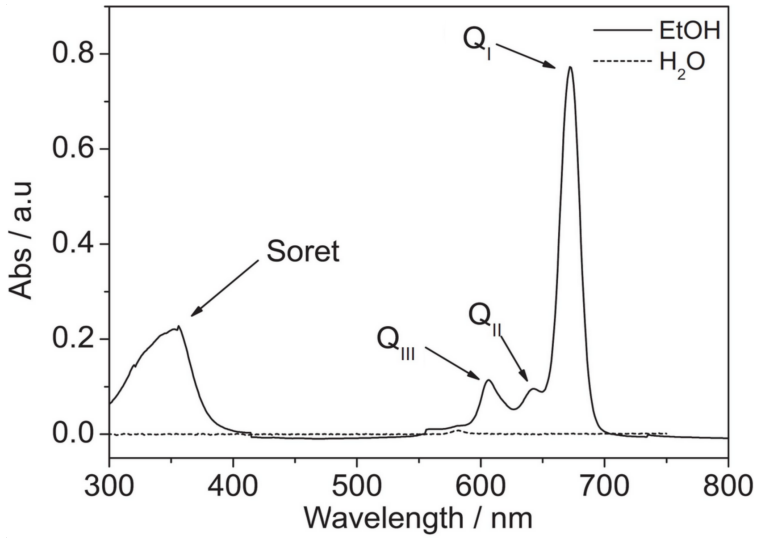

Figure 2.8.: UV-VIS absorption spectrum of AlClPc in the solvents ethanol (straight line) and water (dotted line). Dissolved in ethanol, AlClPc shows a broad featureless absorption band at around 350nm (called, Soret band) and three narrow bands at 606nm (Q_{III}), 640nm (Q_{II}) and 672nm (Q_I) due to transitions from the ground state to vibrational states of the Q-band. Using water as a solvent results in a vanishing absorbance in this spectral region. Image adapted from [61]

The absorption spectrum in ethanol shows two characteristic absorption bands, which are governed by a π-π^* transition of the 18 delocalized π-electrons of the phthalocyanine ring. These two absorption bands are called the Soret-band (centered at 350nm) and the Q-band (600-700 nm) [50]. The Q-band of AlClPc shows a vibrational structure upon the spectral lines which can be seen in Figure 2.8 when using ethanol as a solvent. These spectral lines are strongly broadened and further modified by their interaction with the solvent [49, 61]. The Q-band of AlClPc can

be divided into the most prominent Q_I-band centered at 672 nm (equals to 1.85 eV) which dominates the absorption in the visible region and the Q_{II}- and Q_{III}-bands at 640 nm (1.93 eV) and 606 nm (2.05 eV), which only absorb weakly.

The Soret band, arises due to the electronic transition $S_0 \rightarrow S_2$ from the ground state S_0 to the second excited state S_2, while the Q-band stems from the $S_0 \rightarrow S_1$ transitions between the ground and the first electronically excited state, both of which are characteristic of phthalocyanines in a monomeric state. Besides the Q_I-band with $a_u^1 \rightarrow e_g$ symmetry, the two other Q-bands, labeled Q_I and Q_{II}, can be assigned to vibrational transitions, Q(2,0) and Q(1,0), respectively (cf. Fig. 2.6).

Referring to Figure 2.8, it can also be seen that AlClPc is strongly hydrophobic, which has a direct impact on its water solubility and, therefore, on the absorption. AlClPc forms aggregates in water instead of going into solution. Since aggregation has a direct impact on the photo-chemical properties of the monomer, new absorption bands appear. To characterize this behavior and to avoid aggregation, different water-ethanol ratios were tried out in the course of this work, the results of which are presented in chapter 4.

3. Experimental setup

Now that the theoretical physical concepts that are needed to understand and interpret the experiments performed within this work are laid out, chapter 3 presents the setups used to perform the experiments. Since one of the main key components are ultrashort laser pulses used to initiate and control the optical response of AlClPc, this chapter starts with introducing the laser system in 3.1, followed by the technique used to generate ultrashort broadband light pulses (section 3.2). In addition, the pulse characterization technique dispersion scan (D-Scan) is presented in section 3.3. Last but not least, the experimental setups are presented for the strong-field coherent-control of absorption spectra in section 3.4, as well as for the white-light weak-field characterization of the liquid-phase targets in section 3.5.

3.1. The laser system

To investigate ultrashort dynamic processes, it is beneficial to use laser pulses with a short temporal duration. As the starting point in their generation the commercial laser system FEMTOPOWER™ HE/HR CEP4 from the company Femtolasers is used. This system consists of a combination of a laser oscillator and a chirped-pulse amplifier, which can generate 20 fs pulses with up to 3 mJ pulse energy at a repetition rate of 3 kHz. Both, oscillator and amplifier use a titanium-doped sapphire (Ti:Sa) crystal as a gain medium, which results in pulses at a central wavelength of 790 nm in the near-infrared (NIR) spectral region. The oscillator is a dispersion-stabilized, Kerr-lens mode-locked laser [6, 7], which is internally pumped by a Spectra Physics Millenia diode-pumped solid-state pump laser with 3.4 W continuous power at a central wavelength of 532 nm. The oscillator delivers output pulses with a pulse energy of 3.5 nJ at a repetition rate of 75 MHz. These are sent to the adjacent CEP4 module where their carrier-envelope phase (CEP) is measured by a f–2f interferometer, consisting of a periodically-poled lithium niobate (PPLN) crystal to generate the required second harmonic signal. The CEP is subsequently stabilized by an acousto-

optic frequency shifter (AOFS). This feed-forward scheme can be used to set the CEP to any desired value and makes the complete laser system passively CEP-stable. The oscillator pulses are thereafter used to seed the chirped-pulse amplifier (CPA) [8]. Therein, the seed pulses are first stretched to picosecond timescales via the dispersion in fused silica slabs before they are amplified by propagating through the amplifier crystal ten times, which is externally pumped by a Q-switched pump laser (DM-50 Photonic Industries) at 50 W average power. The amplifier Ti:Sa crystal is cryogenically cooled in a vacuum chamber at a maximum gas pressure of 10^{-5} mbar. To prevent destruction of the amplifier crystal, but at the same time reach maximum peak intensities of the amplified pulses, the quantity of amplified pulses is reduced after four passes through the gain medium. Therefore the beam is guided through a Pockel's cell, which selects only every 25000th pulse, resulting in the final repetition rate of the laser system, of 3 kHz. The selected pulses are thereafter amplitude- and phase shaped by an acousto-optic programmable filter called Dazzler [62], which is used to reduce the gain-narrowing in the amplification process, as well as to change the spectral phase of the pulses to some extent. In the last stage of the amplifier, the amplified, but still temporally stretched pulses are re-compressed in a grating compressor. To account for beam drifts, two sets of beam-align modules consisting of position sensitive diodes and motorized mirrors are used to stabilize the pointing of the beam. One to stabilize the seed in front of the amplifier and the second to stabilize the output of the amplifier. A simplified sketch of the laser system is shown in Figure 3.1.

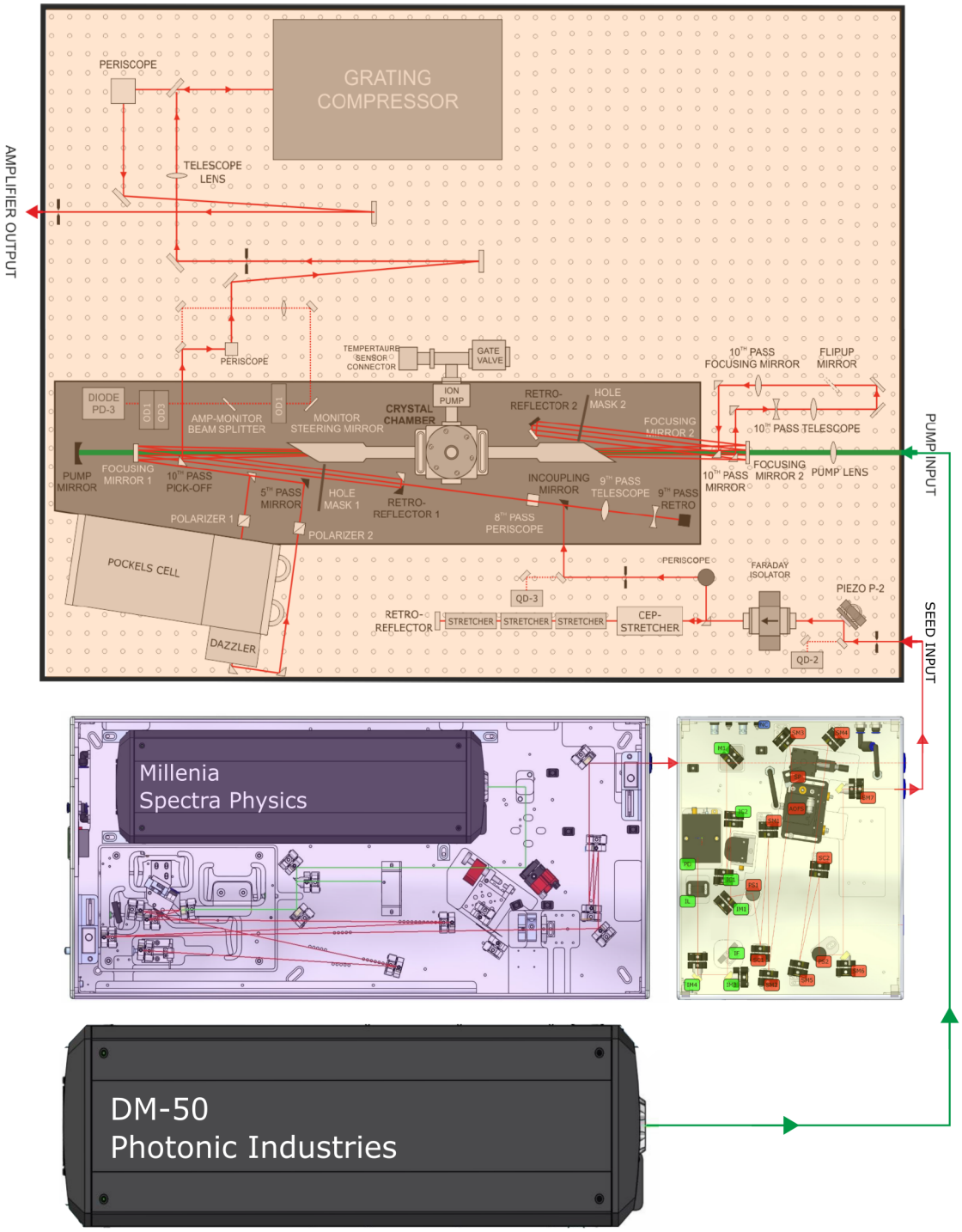

Figure 3.1.: Schematic of the laser system FEMTOPOWER™ HE/HR CEP4. The different parts are highlighted in different colors. The oscillator is highlighted in lilac, the CEP4 module in yellow and the multi-pass amplifier in orange. Image adapted from [62–64].

3.2. Generating ultrashort broadband light pulses

Since the pulses provided by the laser system do not have enough bandwidth to cover the frequency range of typical molecular absorption bands, the pulses need to be spectrally broadened. Therefore, a gas-filled hollow-core fiber is used to increase the bandwidth of the stretched pulses, followed by subsequent compression of the pulses by a chirped-mirror compressor.

3.2.1. The double-differentially pumped hollow-core fiber

Due to the high pulse energy of the laser system, a double-differentially pumped hollow-core fiber is used for the spectral broadening of the laser pulses. The spectral broadening occurs due to self-phase modulation in the gas-filled fiber. This experimental technique was first reported in [65, 66] and is nowadays well established.

Filling the fiber from the middle, while simultaneously pumping both the entrance and exit of the hollow fiber leads to a pressure gradient which helps to reduce plasma generation at the entrance and exit of the fiber, as well as damage of the fiber surface. This fiber design was inspired by the work at the MPQ in Munich [67] and is operated with helium gas as the nonlinear medium. The fiber design can be seen in Figure 3.2.

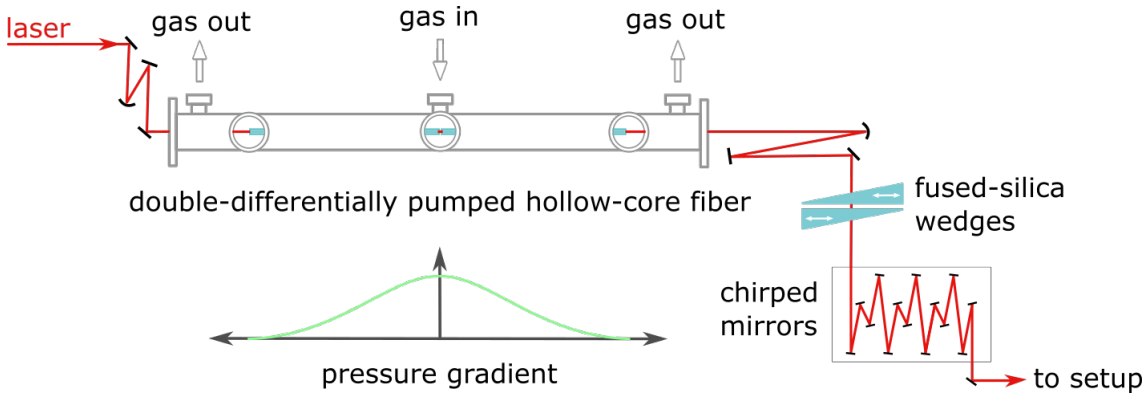

Figure 3.2.: Schematic of the components used to generate broadband ultrashort light pulses. Composed of a double-differentially pumped hollow-core fiber, followed by a pair of fused-silica wedges and a chirped-mirror assembly for subsequent pulse compression.

The capillary itself is a 1.5 meter long glass fiber with an inner diameter of (310 $\pm$ 10) μm. To demonstrate the amount of spectral broadening achievable with this design a pressure scan was conducted and is shown in Figure 3.3.

The most critical part in the fiber installation is the incision in the center of the fiber in order to be able to let the helium gas enter the capillary. After cutting, both

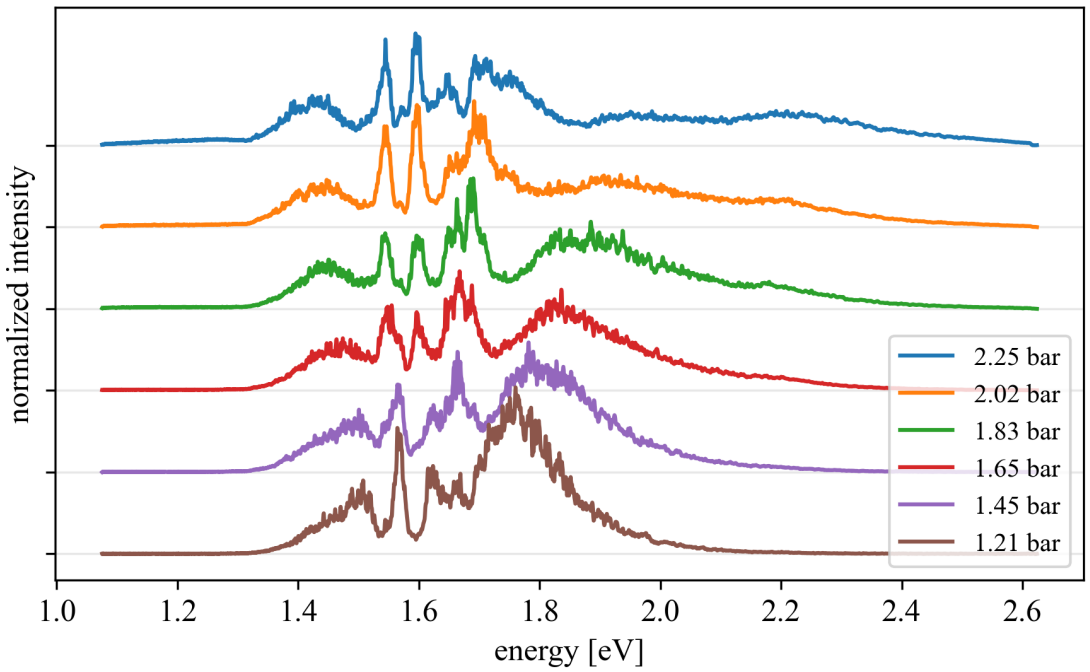

Figure 3.3.: Fiber pressure scan. Shown are the normalized spectra obtained with the doubly-differentially pumped hollow-core fiber for different input helium pressures.

interfaces need to be well aligned to each other to prevent partial out-coupling of the laser beam at the incision point. In addition, both sides of the incision need to be sealed with Torr seal vacuum epoxy glue to prevent gas leaking to the ends of the fiber.

To ensure proper operation of the fiber, it is helpful to first optimize the orientation of the uncut fiber with regard to the laser beam by monitoring the throughput of the attenuated laser. Since individual fibers have different transmission efficiencies due to inaccuracies of the core diameter in the manufacturing process, it is recommended to do this step each time before cutting a new fiber in the center. In addition, one should avoid to turn or rub both interfaces on each other after cutting, since this can lead to a decrease of the maximum accessible throughput. After cutting and sealing both parts, it is necessary to repeat the alignment of the fiber orientation using the attenuated laser beam until a new optimum of the throughput is found before coupling in the full laser beam. With this procedure two different fibers were installed during this thesis, one with 60% and one with 45% transmission, both with a stable beam mode.

3.2.2. Pulse compression

The self-phase modulation in the helium gas not only leads to the spectral broadening, but to an additional chirp of the pulses. This chirp has to be compensated for. To achieve this, a chirped mirror compressor is used consisting of seven pairs of double-angle chirped mirrors (type PC70 from Ultrafast Innovations), which introduce a negative group delay dispersion of -40 fs^2 per pair. To fine-tune the dispersion of the entire beam path, including transmission through air and additional optics, a pair of motorized fused silica glass wedges is used which can be moved in and out of the beam, thereby introducing a variable amount of dispersion to the pulses. With this, pulse durations down to 4.6 fs have been achieved [68]. Further compression of the pulses is limited to higher-order chirp. It is known for setups like this, to produce pulses with negative third-order dispersion, which leads to pre-pulses (see [68, 69]).

It has been demonstrated that introducing more TOD by replacing part of the fused-silica wedges by a material with higher TOD/GDD ratio compared to glass - as, for instance, ammonium dihydrogen phosphate or water - can lead to near perfect pulse compression [70, 71].

3.3. Pulse characterization technique - the dispersion scan (D-Scan)

The difficulty of measuring and characterizing ultrashort laser pulses directly in the time domain is, that one would need to exploit a mechanism with a duration even shorter than that of the pulse itself. This would, in the case of fs-laser pulses, require e.g. a detector with an attosecond response time, which are commercially not available, so far. Hence, most techniques developed in the last decades to characterize fs-laser pulses rely on self-referencing schemes using nonlinear optical processes. Since the observable in those self-referencing schemes are intensities and not the electric fields themselves, a nonlinear process is necessary to measure the pulses' spectral phase. The common principle of established techniques [72–74], therefore, relies on the measurement of spectra generated in a nonlinear process as a function of a control parameter that encodes the spectral phase and subsequent calculations of the pulses' electric field and phase via iterative algorithms and Fourier transformation [75, 76]. In this chapter, the dispersion scan (D-Scan) is introduced, which is used to characterize the generated broadband ultrashort laser pulses.

In the dispersion scan (D-scan), the ultrafast laser pulses are characterized by a controlled change of the pulses' dispersion introduced by the addition of glass within the beam path [77, 78]. Therefore, spectra of a nonlinear process e.g. SHG [79], THG [80] or also self-diffraction [81] are recorded as a function of the glass insertion z, resulting in a 2D trace S(ω,z). To invert these D-Scan traces, different algorithms have been established, such as generalized-projections [82], evolutionary algorithms [83] and deep neural networks [84].

In this work, a SHG D-Scan with a conjugate gradient descent algorithm is performed since no additional optics are needed, as the total beam path already includes a pair of glass wedges for the fine tuning of the pulse duration. For more details on the gradient descent algorithm and its robustness see [85]. For the calculation of the theoretical D-Scan trace, the algorithm demands an independent measurement of the pulse's fundamental spectrum $|F(\omega_f)|^2$:

$$S_{DSCAN}(\omega, z) \propto \left| \int_{-\infty}^{\infty} \left(\int_{-\infty}^{\infty} F(\omega_f) e^{ik(\omega_f)z} e^{i\omega_f t} d\omega_f \right)^2 e^{i\omega t} dt \right|^2 . \tag{3.1}$$

The retrieval will iteratively change the spectral phase until the difference between theoretical and experimental trace are minimized. An exemplary experimental trace and the determined theoretical results are shown in Fig. 5.6 and Fig. 5.7.

3.4. Experimental setup for the coherent control of transient absorption spectra

The experimental setup used for the coherent control of the absorption spectra of AlClPc in the liquid phase was altered during the course of this work. Since measurements were performed with both versions and data evaluation and measurement scheme depend on the setup version used, both versions are presented here. The two variations are, in the following, named after their individual advantages. It has to be noted that both versions do offer advantages and disantvantages, such that no version is strictly better than the other.

3.4.1. Version 1: Direct reference method

To get an impression of the direct reference method, a sketch is shown in Figure 3.4.

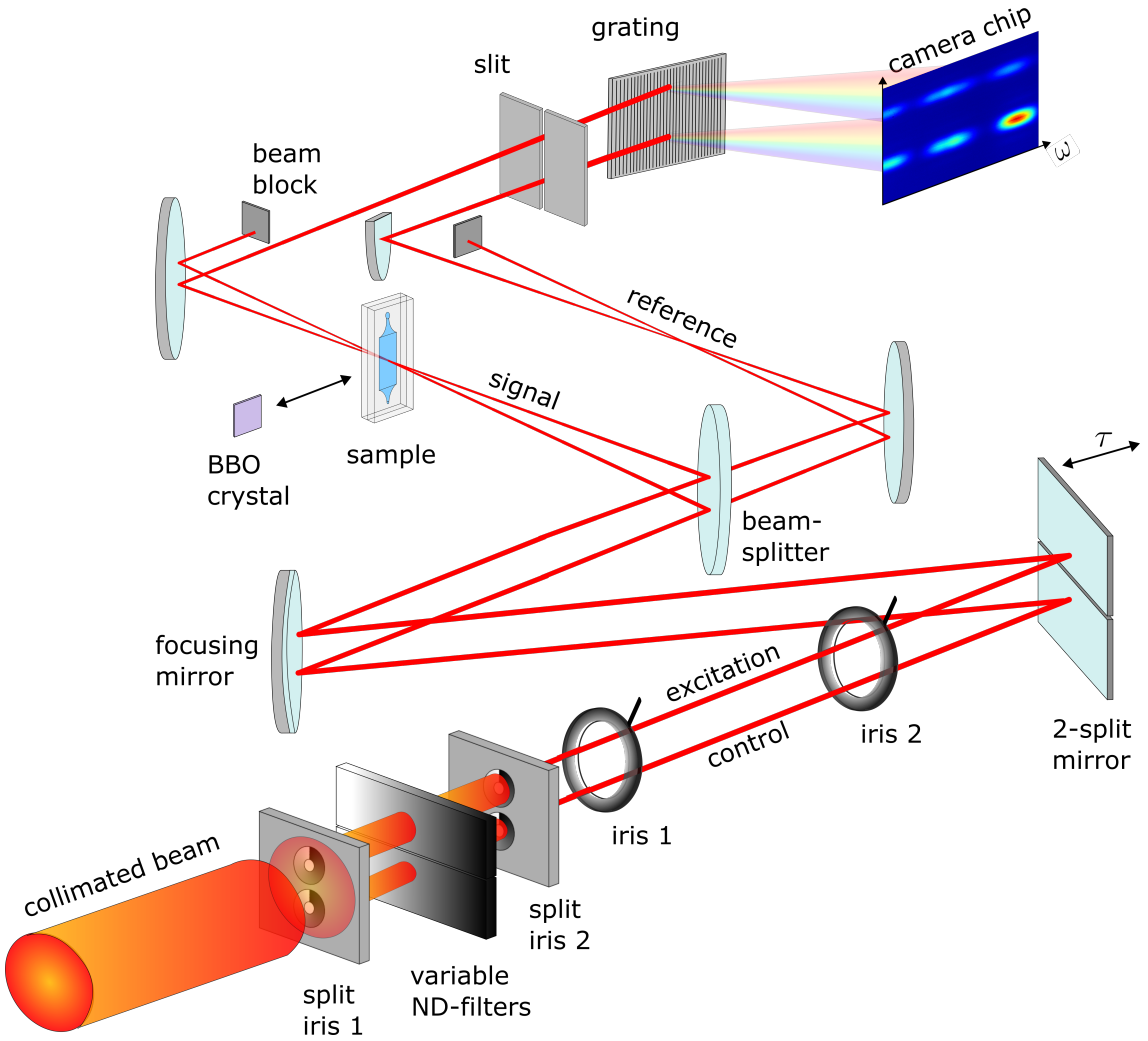

Figure 3.4.: Simplified sketch of the experimental coherent-control setup. See text for details. — Note: Both, the 2-split mirror and the focusing mirror are experimentally hit under close-to-normal angle of incidence. Increased angles are depicted in the illustration for a better schematic overview.

The broadband ultrashort laser pulses enter the setup as a collimated beam. Since the aim is to conduct time-dependent measurements on the absorption of liquid targets, the beam is divided into two phase-synchronized excitation and control beams by a custom-built split-iris consisting of an array of two iris apertures (Thorlabs ID5MS). The beamlet diameters can, in this way, be independently set in a range between 1.0 mm and 5.1 mm, which has a direct impact on their individual focus sizes. When conducting an experiment, the iris parameters are adjusted such that the control beam has a bigger focus diameter than the excitation beam. This ensures that the area illuminated by the excitation pulse experiences a control pulse with minimal intensity gradient within the excitation-pulse illumination area. In the next step, both beamlets

pass two independently adjustable fused silica variable neutral density (ND) filters (Thorlabs NDL-25C-4), which allow for an independent attenuation between OD 0.04 and OD 4 for each beamlet. The filter which regulates the intensity of the control beam is, additionally, placed on a motorized 60 mm linear translation stage with resonant Piezoelectric motors (Thorlabs Elliptec ELL20/M) to allow for automatized intensity scans, while the other filter is placed on a manual one-axis translation mount (Thorlabs XF100/M). After this, both beamlets pass a second split iris. These iris apertures have the purpose to cut out the interference rings on both beamlets due to the first split iris. Looking at Figure 3.4, the reader might notice two additional "normal" iris apertures. These are mounted at fixed positions and represent the two fixed points for proper alignment of the complete collimated beam into the setup. Note that these iris apertures are only used for the in-coupling of the collimated beam into the setup and are kept open during a measurement. The time delay between both, excitation and control beam, is introduced by a home-built two-component mirror consisting of two rectangular silver mirrors separately mounted on piezo micrometer delay stages (PIHera Piezo Linearstage P-622.1CD, Physik Instrumente). The 2-split mirror is hit by the laser beams under close-to-normal angle of incidence, allowing to access time delays of up to +/- 1.7 ps. Shortly after the focusing mirror with a focal length of 500 mm, both beams pass a broadband beamsplitter (Layertech 110105), reflecting 80% and transmitting 20% of the two beamlets. The transmitted part is used as a direct reference, while the reflected part is guided into the target where both, excitation and control beam spatially overlap. In this focal plane, the liquid sample of interest, as well as a BBO crystal (Newlight Photonics Inc., BTC5002-SHG800(I)-P) for direct pulse characterization can be placed. This allows to estimate the pulse duration and its spectral phase to which the target is exposed to. In both pathways, the strong-field control beams are blocked and only the two excitation beams are refocused ($f = 250$ mm) with a spatial offset onto the slit of a Czerny-Turner-type spectrometer (Acton SpectraPro, Princeton Instruments), allowing for the simultaneous measurement of both the transmitted light through the sample and the unchanged reference beam on the same camera chip (first: CCD camera CoolSnap K4, Teledyne Photometrics, later: sCMOS camera Zyla 5.5, Andor Oxford Instruments) as a function of the excitation-control time delay. The spectrometer is equipped with two 500 nm blaze concave gratings: 600 grooves/mm and 150 grooves/mm making two operation modes possible. The 600 groves/mm grating provides a resolution of 1.7 meV, while the 150 groves/mm grating provides a resolution of 7.4 meV. Taking the size of the camera

chip along the dispersion axis of the gratings into account, this leads to a "spectral" observation area of 605.2 nm and 136.7 nm for the use of the CoolSnap K4 camera and 662.7 nm and 148.7 nm for the Zyla 5.5 sCMOS camera, respectively. The gratings within the spectrometer can be rotated to allow for the measurement of different spectral ranges on the camera chip.

As a sample container for the liquid phase targets, cyclic olefin copolymer cuvettes (SpecVette™ manufactured by Aline Inc.) with 0.5 mm path length and 25 μL volume are used. The BBO crystal (Newlight Photonics Inc., BTC5002-SHG800(I)-P) used for in-situ pulse characterization has a thickness of 20 μm to allow for the SHG generation of the complete input spectrum. For the measurement of the SHG signal, the grating within the spectrometer is rotated to a central wavelength of 400 nm (corresponding to 3.1 eV), thereby spatially cutting out the fundamental light. It has to be noted that the in-situ pulse characterization comes with a tradeoff. The main disadvantage lies in the bad spectrometer and camera efficiency for wavelengths below 350 nm, which can be seen in the corresponding efficiency curves provided in the appendix A.3 of this thesis. This means, that even though the BBO crystal is able to generate the second harmonic of the entire spectrum, the combination of spectrometer and camera is not able to detect it completely. In the future, this can be improved by measuring the SHG light by a UV-enhanced fiber spectrometer.

3.4.2. Version 2: Low dispersion method

The experimental setup was further improved in terms of allowing for even shorter laser pulses. Therefore, the beamsplitter presented in section 3.4.1 was removed such that a simultaneous measurement of the transmitted light through the target and the incoming reference is no longer feasible. Thus, the setup was equipped with an additional 28 mm linear translation stage with resonant Piezoelectric motors (Thorlabs Elliptec ELL17/M) in the focal plane to allow for alternating between references and absorption spectra by moving the sample of interest in and out during a measurement run. In addition, the old CCD camera was replaced with a new sCMOS camera (Zyla 5.5 sCMOS, Andor Oxford Instruments), which allows for significantly higher frame rates up to 3 kHz. With this, single-shot measurements can be conducted in the future, provided a perfect synchronization between camera and laser system is achieved. A schematic of the modified experimental coherent-control setup is presented in Figure 3.5.

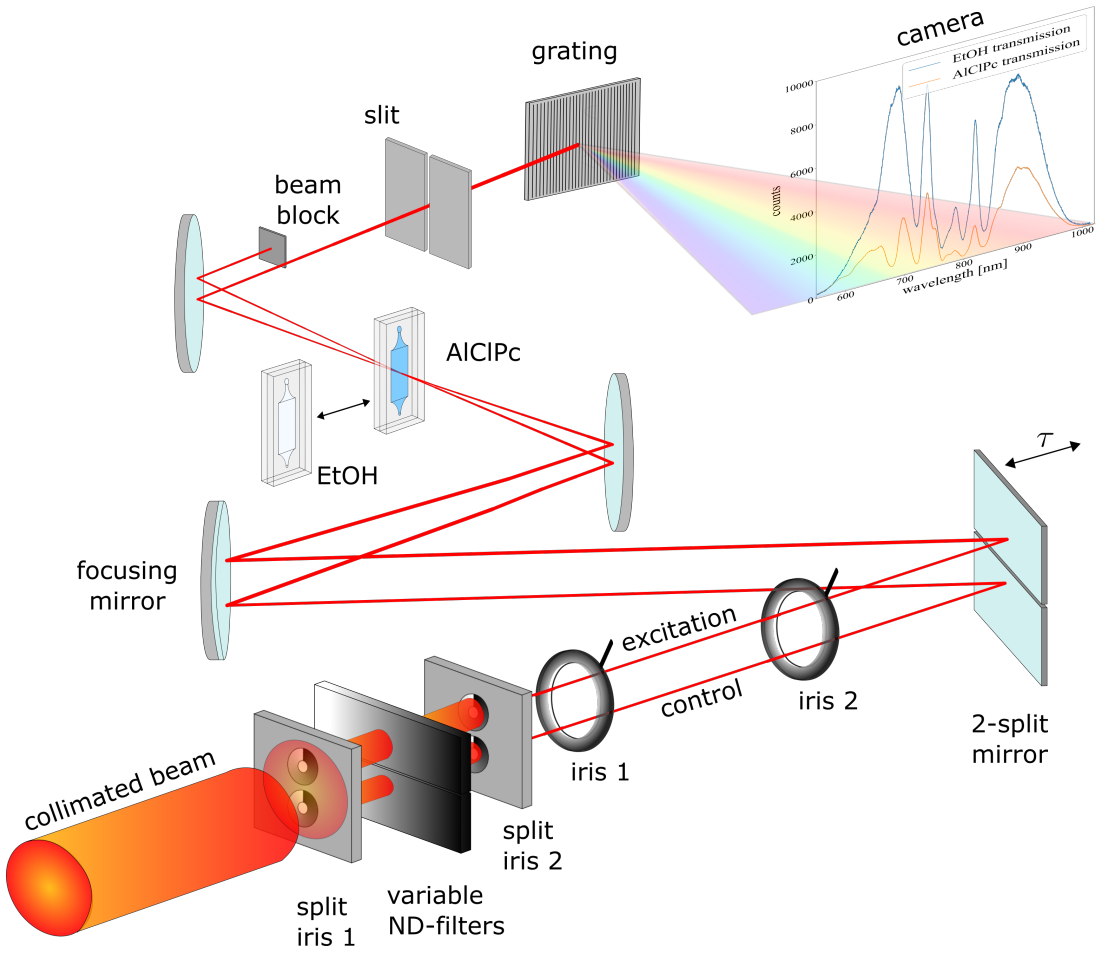

Figure 3.5.: Scheme of the experimental setup optimized for ultrashort laser pulses. The inlet shows two transmission spectra, once the transmission through (in the optical regime) transparent ethanol and once through dissolved AlClPc molecules.

3.5. Experimental setup for sample characterization

In order to prepare samples suitable for the measurement technique, meaning samples with an optical density of approximate OD 1, a portable setup was built, such that samples could be characterized in the chemistry lab and, in addition directly before (and after) the actual measurement run. The two main reasons to aim for a sample with approximately OD 1 are the following: First of all one aims for an optical density with a high signal-to-noise ratio, but at the same time one needs to make sure, that there is still enough light transmitted through the sample which can be detected to make a statement about the absorption line shape at all. Since the thin sample containers cannot be flushed to change the target density during an experiment, it is important to optimize and characterize the liquid samples beforehand. A schematic

overview of the white-light characterization setup constructed for this purpose is shown in Figure 3.6.

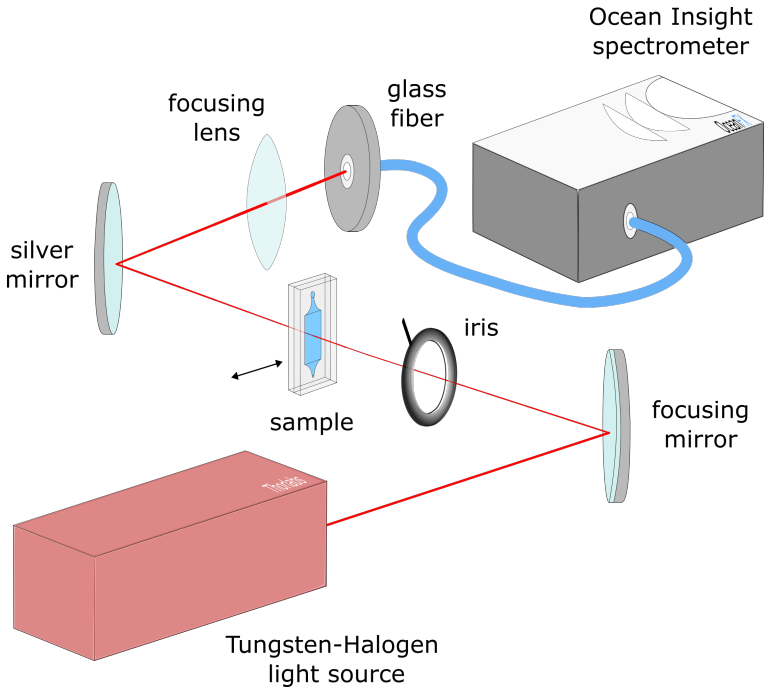

Figure 3.6.: White-light setup for sample characterization. For simplicity, only the important components are shown. Additional deflection mirrors are not shown for better visibility.

As a light source, a compact stabilized Tungsten-Halogen light source from Thorlabs (SLS201L/M) is used, providing a constant-intensity 10 mW black-body radiation spectrum between 360 and 2600 nm. This light hits a spherical mirror with a focusing length of 250 mm under close-to-normal incidence (not to scale in Figure 3.6). The sample is placed in the focus of this mirror. Since the focus has a bigger diameter than the sample container, an iris is placed directly in front of the target to further reduce the beam diameter such that only the target and not the complete sample container is illuminated. The sample holder in the focal plane is mounted on a manual micrometer translation stage, allowing to move the sample in and out of the beam. After passing the target, the beam is focused into an mounted optical glass-fiber which serves as a waveguide into the Ocean FX-XR1 extended-range spectrometer (Ocean Insight), which supports the spectral region between 200 nm and 1025 nm.

4. Target preparation, optimization and white-light characterization

Now that the experimental setups have been presented, it is time to dive into the target preparation. When measuring the absorption spectrum of AlClPc in the liquid phase, a few parameters have to be taken into consideration, such as the choice of the appropriate solvent and desirable target densities. Since the target container is a closed system, these parameters cannot be tuned during the experiment. Therefore, they need to be optimized prior to placing the sample in the intense laser field. In addition, it is convenient to characterize the sample using a weak white-light source before placing it into the intense laser field provided by the Ti:Sa laser. As intense fields can introduce instantaneous changes in the target, such as ground-state bleaching or the destruction of the molecule, which have a direct impact on the optical density and would lead to wrong conclusions.

4.1. Solvent compatibility

To measure and control the absorption spectrum in the liquid phase, an appropriate solvent is required, such that the optical properties of the solvent do not dominate the molecular absorption of AlClPc. Recent research [49, 61] shows, that the choice of the solvent is crucial to obtain a reliable spectrum and avoid self-aggregation of the molecules, as it happens if they are dissolved in pure water. On the same hand, the solvent needs to be compatible with the sample container, such that it does not damage its material. Furthermore, using inappropriate solvents leads to insolubility which results in the formation of aggregates and, therefore, a change in the absorption spectrum. Since ethanol is non-poisonous, transparent in the visible regime and gives rise to a clear absorption spectrum of AlClPc, it was used as the main solvent within this thesis. The absorption spectrum of AlClPc in pure ethanol (and pure water) can be seen in Figure 2.8.

As a sample container, cyclic olefin copolymer (COC) cuvettes (SpecVette™ manufactured by Aline Inc.) with 0.5 mm path length and 25 μl volume were used. This specific choice is made because of two main reasons: First, the sample thickness should be as thin as possible, to impede the re-absorption of the induced polarization of the first molecule by a second (all molecules "see" the same incoming electric field). And second, since the sample thickness is chosen to be as small as possible, the window material of the sample container will automatically be placed near the focus of the intense laser beam. Therefore, the windows of the sample container have to be as thin as possible to avoid strong-field effects occuring in the window material. Conventional quarz cuvettes with a standard window thickness of 1.25 mm are, therefore, not suitable for the used measurement concept. The window thickness of the used SpecVette™ cuvettes was estimated to be approximately 100 μm by a measurement of the in-house precision mechanics workshop. The design of the copolymer cuvettes is such that the container itself consists of two thin copolymer films that are glued to each other. Unfortunately, the used adhesive is attacked by most solvents in high concentration, such that by filling the cuvette with 100 percent ethanol would dissolve the adhesive, leading to a leaking cuvette. To overcome this problem, a compromise was made by diluting the ethanol-AlClPc mixture with different percentages of water, even though water might quench the absorption and supports the creation of AlClPc aggregates. The dilution with other solvents instead of water was not possible, due to the sensitive adhesive between the cuvette windows. To ensure proper absorption spectra of AlClPc diluted in a mixture of ethanol and water, a solvent compatibility study of different ethanol-water percentages was made, where the absorption of the diluted complex was measured with the white-light characterization setup presented in section 3.5. The results are summarized in section 4.4.

In the future the experiment could be further improved by using a liquid jet instead of a sample container, thereby getting rid of additional material near the target focus, as well as opening up the possibility of using 100 percent ethanol as a solvent leading to improved absorption spectra.

4.2. Calculations of the optimal sample density

As already mentioned in the introduction of this chapter, tuning the target density during a measurement is not possible, due to the closed system target cell. Therefore, estimating/calculating the optimal target densities for the envisioned absorption

measurements is crucial. There are two constraining limits upon the target density. First of all, the density needs to be high enough, such that the absorption bands can be detected with a decent signal-to-noise ratio. On the other hand the density should not exceed the dynamic range of the cameras, since this would lead to a loss of information on the exact shape of the absorption bands. Especially, since the Q_I-band is very pronounced compared to the Q_{II}- and Q_{III}-band, a balance needs to be found for which all three absorption bands can be nicely detected. The goal is, therefore, to prepare a sample with an optical density between 1 and 2. The optical density is defined by Beer-Lambert's law via

$$OD(\omega) = -\log_{10}\left(\frac{I(\omega)}{I_0(\omega)}\right) = \epsilon(\omega)Cd, \tag{4.1}$$

with the sample-specific molar extinction coefficient $\epsilon(\omega)$, the molar concentration C and target thickness d. The molar concentration is in turn defined as

$$C = \frac{n}{V}, \text{ with } n = \frac{m}{M}, \tag{4.2}$$

where the amount of substance n can be expressed as the ration between the mass of the sample m and its specific molar mass M. Using equation 4.1 and 4.2 the amount of AlClPc powder, which needs to be dissolved to produce a sample with a desired optical density is given by

$$m = \frac{OD(\omega)VM}{\epsilon(\omega)d}. \tag{4.3}$$

The specific molar mass M of AlClPc is 574.96 g/mol [86]. The extinction coefficient of AlClPc in ethanol at the wavelength 672 nm was experimentally determined in reference [49] to be 293.9 ($\pm$ 0.9) $\cdot 10^3$ L /(mol·cm). With equation 4.3 in hand, the amount of compound needed for any experimental parameters of the desired optical density $OD(\omega)$, with specific target thickness d and total volume V can be calculated.

4.3. Sample preparation

Throughout this thesis AlClPc (purchased from Sigma-Aldrich) with a purity of 85% [86], spectroscopic ethanol (Uvasol® from Sigma-Aldrich) with a purity of 99.9% and distilled (Milli-Q) water were used. The AlClPc powder and solutions were kept refrigerated and protected from light, to prevent bleaching.

For an optical density of 1 with a target volume of 1mL and a propagation thickness

of 500 μm, the amount of AlClPc powder needed for the solution is (according to equation 4.3): $m = 3.9$ μg. Since the chemical laboratory is not equipped with a scale precise enough to measure such small quantities, a 1 mL stock solution with an optical density of OD = 100 is produced by weighing 3.9 mg instead and dissolving this in 1 mL Uvasol® ethanol. An optical density of 1 can then be produced by diluting the stock solution at a ratio of 1 to 100.

The first sample, which was used for the measurement shown in subsection 5.3.1, was prepared by dissolving 4.2 mg of AlClPc in 0.01 mL of Uvasol® ethanol, which was in turn further diluted with distilled water with a ratio of 3:1 resulting in a solution with a concentration of 55 nmol/mL.

For the second measurement, the results of which are shown in subsection 5.3.2, the sample was prepared by dissolving 3.8 mg of AlClPc in 1 mL of Uvasol® ethanol, which was further diluted in a second step in a ratio of 1:10 ethanol, obtaining 1 mL of OD 10 solution. This stock solution was further diluted in a ratio of 1:10 with a solvent mixture of 70% ethanol and 30% of milli-Q water.

4.4. Sample characterization - AlClPc in binary ethanol-water solutions

This section focuses on the weak-field white-light characterization of different AlClPc liquid-phase targets. First of all, the absorption of AlClPc samples with varying solvent, consisting of ethanol and water in different relative percentages are presented to show which impact the additional water has on the absorption properties of the complex molecule. Secondly, the absorption spectra of AlClPc in a solvent consisting of 80% ethanol and 20% water with varying AlClPc target densities are measured to obtain which maximum densities can be used before the aggregation of the complexes dominates the monomeric state. Finally, the bleaching properties of AlClPc are investigated under the long-term irradiation of weak light. For further details on the sample characterization the reader is referred to [87].

Variation of the solvent The weak-field white-light absorption spectra of AlClPc in aqueous ethanol solutions with varying ethanol/water percentages are presented in Figure 4.1.

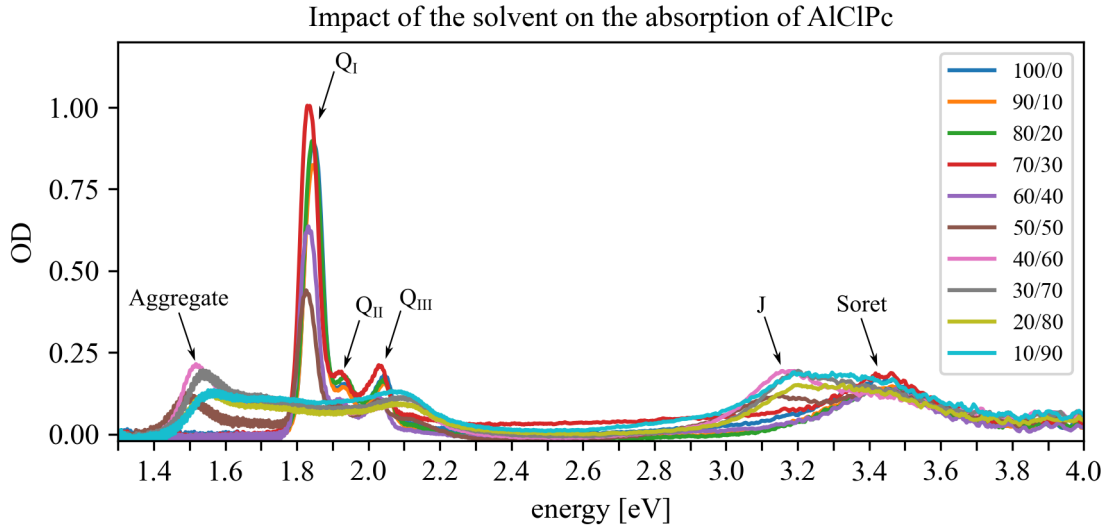

Figure 4.1.: UV-VIS absorption spectrum of AlClPc for different solvent ratios. The label notation refers to the ethanol/water ratio - meaning 100/0 equals to a pure ethanol solvent, while 60/40 refers to a solvent consisting of 60% ethanol and 40% water.

As can be directly seen, the solvent has a large impact on the absorption properties of AlClPc. The Q_I-band is only present down to a solvent percentage of 50/50 and vanishes beyond this. At the same time, the emergence of the aggregation-associated band at approximately 1.5 eV for water concentrations higher than 40% can be observed. Furthermore, also the Soret-band changes with the solvent, but stays present throughout all chosen solvent ratios. To quantify the solvent-induced changes in the absorption of AlClPc, the three aforementioned bands are analyzed in their amplitude and central energy as a function of the used water percentage.

Figure 4.2 shows a maximum of the optical density of the Q_I-band for a solvent consisting of 70% ethanol and 30% water. When increasing the water percentage further, the absorbance drops followed by the complete suppression of the absorption peak. At the same time, it can be observed that the increase of water ratio consistently shifts the central energy of the absorption band to lower energies. As a result, for the investigation of AlClPc in the monomeric state, a solvent should be chosen with a water percentage smaller than 40%.

If one is specifically interested in investigating the aggregates, Figure 4.3(A) emphasizes a solvent consisting of 40% ethanol and 60% of water. In this case the aggregation band is most pronounced. The aggregate's absorption-band center energy is found to increase with the water in the solvent used.

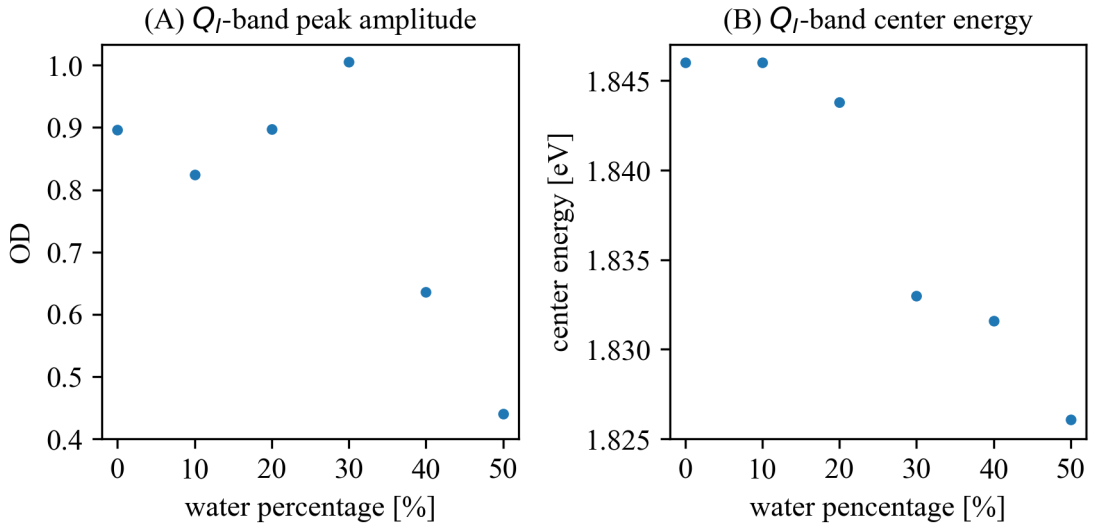

Figure 4.2.: Q_I-band peak amplitude (A) and center energy (B) for a water percentage between 0% and 50%. Since the absorption band vanishes for higher water percentages, these have been excluded in this analysis.

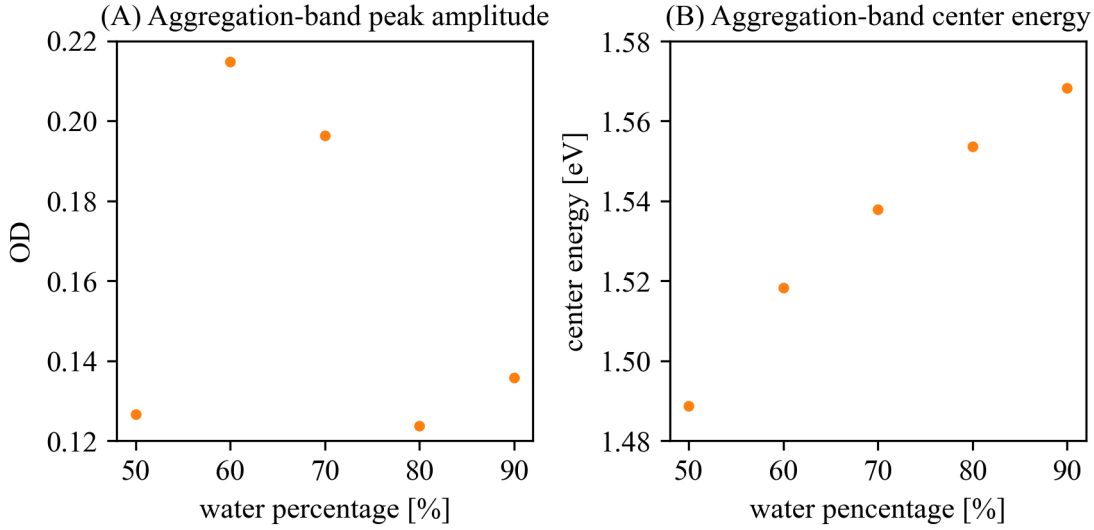

Figure 4.3.: Water-dependent absorption-band properties of the emerging aggregation-band. Since this absorption band only starts to emerge at a water percentage of 50%, lower values were not taken into consideration.

In contrast to both, the monomeric Q-bands and the aggregate's absorption band, the Soret-band remains present for all water percentages investigated. When analyzing the Soret-band's amplitude (see Figure 4.4(A)), it can be found that in accordance to the Q_I-band it is most pronounced in a solvent consisting of 70% ethanol and 30%

water. Therefore, this solvent ratio seems to be the best choice to investigate the absorption of monomeric AlClPc. For the solvent ratios that promote the presence of aggregates (starting from 50% to 90% water in the solvent), the Soret-band peak amplitude seems to increase again. This increase is mostly due to the emergence of the aggregate J-band, which overlaps with the Soret-band energetically (cf. Fig. 4.1), making it difficult to determine the partial peak amplitude of the monomeric state. On the same hand, the center energy of the Soret-band exhibits an instantaneous drop in the presence of aggregation, as can be seen in Figure 4.4(B)).

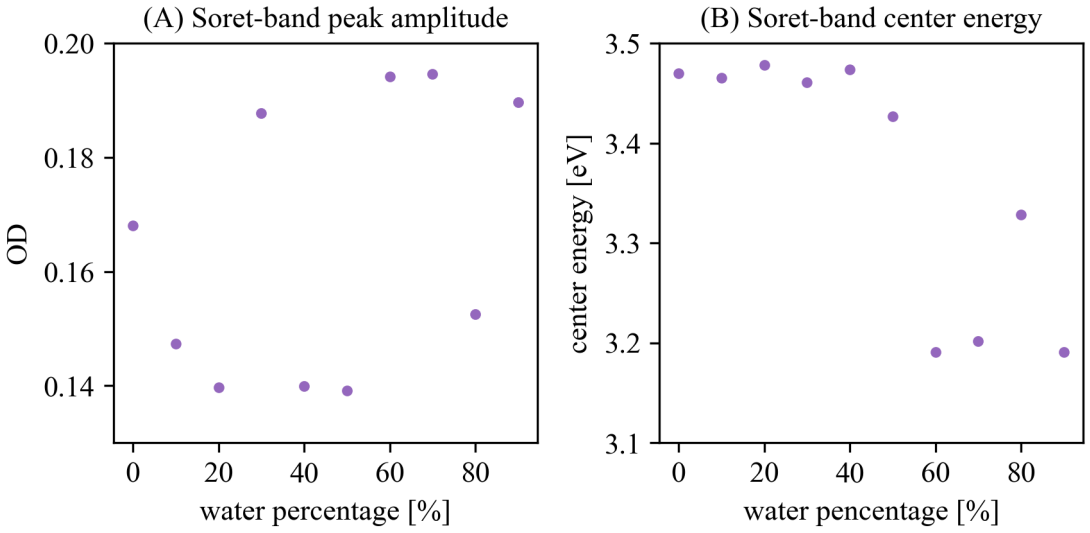

Figure 4.4.: Impact of water on the absorption band properties of AlClPc's Soret-band. Panel (A) depicts the maximum peak value and (B) the center energy of the absorption band.

The overall increase in absorption of the monomeric state for the solvent consisting of 70% ethanol and 30% water is higher than reported in reference [49]. The reason for this could lie in the interaction of the highly concentrated ethanol with the adhesive of the used COC cuvette, resulting in an overall decrease in the absorbance of the AlClPc molecules for water percentages $\leq 20\%$.

Variation of the target density Now that the impact of the solvent on the absorption spectrum of AlClPc is determined, the target densities are varied in a range from 22 nmol/mL up to 444 nmol/mL, in a solvent consisting of 80% of ethanol and 20% water. The aim of this density scan is to quantify up to which densities the complex molecule is still predominant in the monomeric state and when the aggregation of the target starts to become significant. For this, a dilution series is prepared for COC

cuvettes with a path length of 250 μm. Using these relatively thin cuvettes enables the possibility to use higher target densities while still keeping the transmittance through the sample higher than the detection limit of the spectrometer. The measured weak-field white-light absorption spectra of AlClPc in a solvent consisting of 80% ethanol and 20% water for different target densities are shown in Figure 4.5.

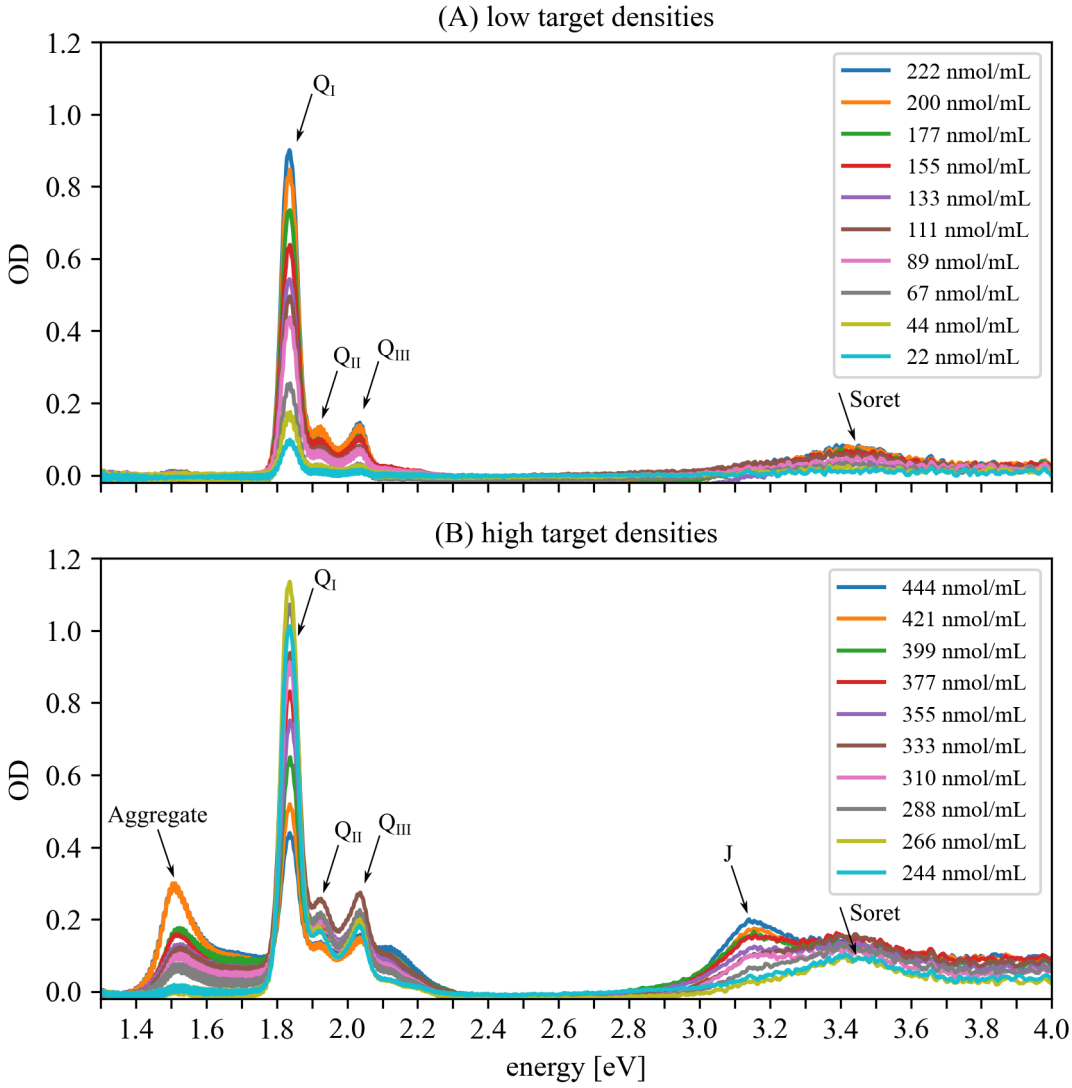

Figure 4.5.: Weak-field white-light absorption of AlClPc for varying target densities. The solvent was chosen to consist of 80% ethanol and 20% water. Panel (A) shows target densities from 22 nmol/L to 222 nmol/L, leading to ODs below 1 where only the monomeric state is present. Panel (B) shows target densities above 244 nmol/mL. The absorbance of the Q-band is maximized for a target density of 266 nmol/mL. Higher target densities lead to a decrease of the Q-band which is accompanied by a simultaneous increase of the aggregate's absorption band at approximately 1.5 eV.

Figure 4.5(A) shows the 10 lowest target densities. In this regime, a linear relation

between the target concentration and the target density can be found. The maximum optical density is achieved for a target density of 266 nmol/mL (see Figure 4.5(B)). Higher target densities lead to a decrease of the Q-band which is accompanied by a simultaneous increase of the aggregate's absorption band at approximately 1.5 eV. In addition, a splitting of the Soret-band at 3.2 eV can be seen. This in turn, can be associated to the J-band, confirming the presence of the aggregate state [49].

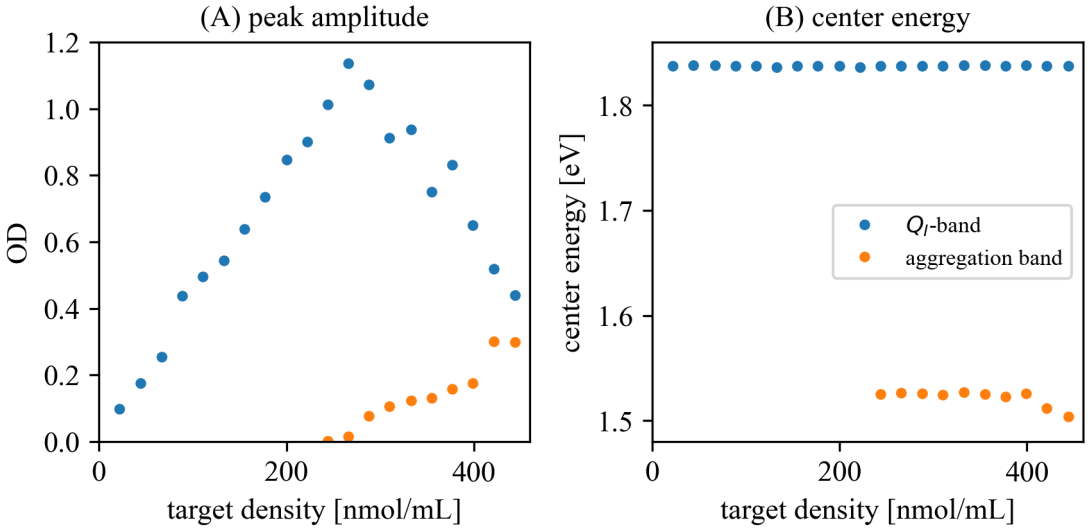

Figure 4.6.: Peak amplitudes (A) of the Q_I-, as well as the aggregation band as a function of the target density. The linear relation between the optical density and the target density given by Beer-Lambert's law is only valid for concentrations up to approximately 266 nmol/mL. For higher target densities, the optical density of the Q_I-band decreases. Simultaneously, the buildup of the aggregation band centered at an energy of 1.52 eV can be observed. In contrast to the solvent scan, the center energies of both absorption bands remain almost unchanged, as can be seen in Fig. 4.6(B).

Figure 4.6 shows the amplitude (A), as well as the center energy (B) of the Q_I-absorption band as a function of the target density. From Fig. 4.6(A) it can be seen, that for the calculation of the monomeric OD Beer-Lambert's law can only be applied up to a concentration of approximately 266 nmol/mL, since for higher concentrations the aggregation of the molecules dominates the change in absorbance. The absorption-bands center energy remains unchanged for all measured target densities.

Long-term measurement of the absorption Since AlClPc is an unstable dye under the impact of intense light, its bleaching properties due to light irradiation are investigated in this paragraph. Therefore, a sample with a concentration of c = (4.9 $\pm$ 0.2) $\cdot 10^{-5}$ mol/L is prepared with the solvent consisting of 80% ethanol and 20%

water. The transmitted light through the sample is measured with an interval of 10 minutes for the total duration of 20 hours. The peak amplitude of the Q_I-band's optical density is depicted in Figure 4.7 over the course of time. An exponential decrease of the OD can be observed for the first 8 hours. After 10 hours, the optical density slowly increases. This can be explained by a slight evaporation of the solvent leading to a relative increase in the concentration, due to the reduced total volume of the sample. To get a rough estimate on the bleaching properties, the peak amplitude values were fitted with the exponential function

$$F(t) = A \cdot e^{-t/\tau} + b, \tag{4.4}$$

with decay time τ and additional fit constants A and b. The best fit to the data, was obtained with the following values: $A = (58.5 \pm 1.4) \cdot 10^{-3}$, $\tau = (125 \pm 7)$ min and $b = 1.0470 \pm 0.0005$. During this long-term measurement, the optical density dropped by 9%. Though this seems to be negligible, one should keep bleaching in mind, since it might have a bigger impact when performing experiments with even stronger laser fields.

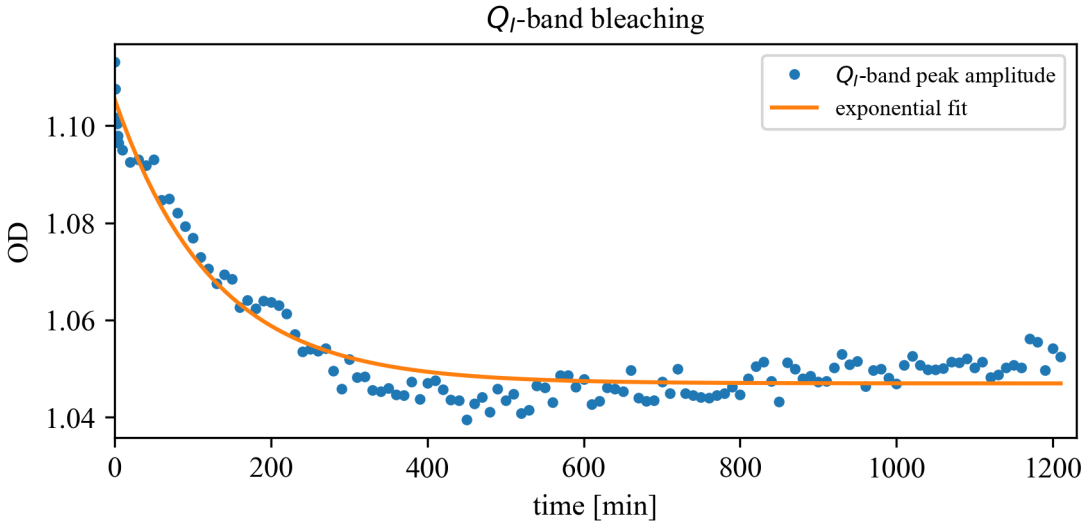

Figure 4.7.: Peak amplitude of the Q_I-band over a time-duration of 20 hours, depicted by blue dots. Over the course of time, the peak amplitude decreases following an exponential decay (see orange fit to the data). This can be explained by a bleaching of the dye due to the uninterrupted irradiation by the white-light source. For this measurement, the white-light source was attenuated to an average power of 200 μW.

Results To summarize, there are three main effects that can distort the absorption properties of AlClPc: solvent, aggregation and bleaching. To avoid distortion of the absorption spectrum, a scan of the solvent ratio was performed, resulting in an optimal working range between 10% and 30% of water in the ethanol solvent as a compromise to the experimentally not feasible solvent consisting of 100% ethanol. Furthermore, the absorbance as a function of the target density was measured to give an estimate on the maximum target density at which solely the monomeric AlClPc is present. Since the AlClPc dimers might react differently under the influence of strong laser fields, it is convenient to choose a concentration where only the monomer is present. Last but not least, the bleaching of AlClPc under weak-field irradiation was measured over a course of 20 hours. This measurement suggests that absorption spectra might differ in amplitude when performing long-term measurements. Bleaching can, in the future, be avoided by the implementation of a flow cell or a liquid jet, providing efficient refreshing of the sample, while solvent effects and aggregation are both interesting for future measurement campaigns. However, this work focuses on gaining an understanding of the strong-field induced control of the optical response of AlClPc in the liquid phase. Therefore further complications due to aggregation and solvent effects on the weak-field absorption of AlClPc are avoided.

5. Strong-field coherent control of AlClPc's optical response in ethanol-water solution

After the characterization of the absorption properties of the liquid target, the experiments can be performed. This chapter starts with explaining the measurement concept used within this thesis in section 5.1, followed by the experimental setup (version-specific) data evaluation in section 5.2 and closing with a presentation of the experimental results in 5.3.

5.1. Measurement concept

The goal of this work is to expand the dynamic control of absorption spectra - which have been established in the XUV-NIR spectral region on gas phase targets [14, 31, 32, 40] - to the liquid phase using time-resolved absorption spectroscopy in the visible (VIS) to near-infrared (NIR) regime. Therefore, the conceptual idea of modifying and controlling the target's optical dipole response with intense laser fields is used. A schematic of how the optical response can be affected by an electric field is shown in Figure 5.1. By the interaction of a weak excitation light/laser pulse at time $t = 0$ with a medium, a freely decaying dipole response is induced, which in turn interferes with the electric field of the excitation pulse, leading to the target's characteristic unperturbed absorption spectrum imprinted on the excitation pulse spectrum (see equations 2.41 and 2.42). In the presence of a second laser field – which, in the following, will be referred to as the control pulse – at a time $\tau > 0$, the initially induced dipole response can be coherently modified by the control pulse. This scenario is also known from literature as the "perturbed free-induction decay" [41–43]. A direct comparison between the temporal evolution of an exemplary unperturbed and a perturbed dipole response in the time domain is depicted in

Figure 5.1. This change of the temporal evolution of the dipole response leads to characteristic spectral modifications of the system's absorption spectrum imprinted on the excitation pulse [22, 24, 31]. Due to the measurement of the observable in the spectral regime via a grating-based spectrometer, the Fourier transform of the real-time dipole response is intrinsically performed, resulting in a time-integrated spectral measurement. Therefore, it includes both, the excitation pulse at $t = 0$ and its (in the presence of the control pulse, perturbed) dipole response for $t > 0$. This concept presents a time-domain picture of the light-matter interaction where the absorption of light is understood in the impulsive limit of a time-domain dipole response function. This response function can be laser-controlled while the system is still reacting coherently upon the initial impulsive stimulus. It has been shown in previous work [32] that the full real-time action of the control pulse on the target's dynamics can be retrieved from the experimentally measured absorption spectra, provided sufficiently short pulses.

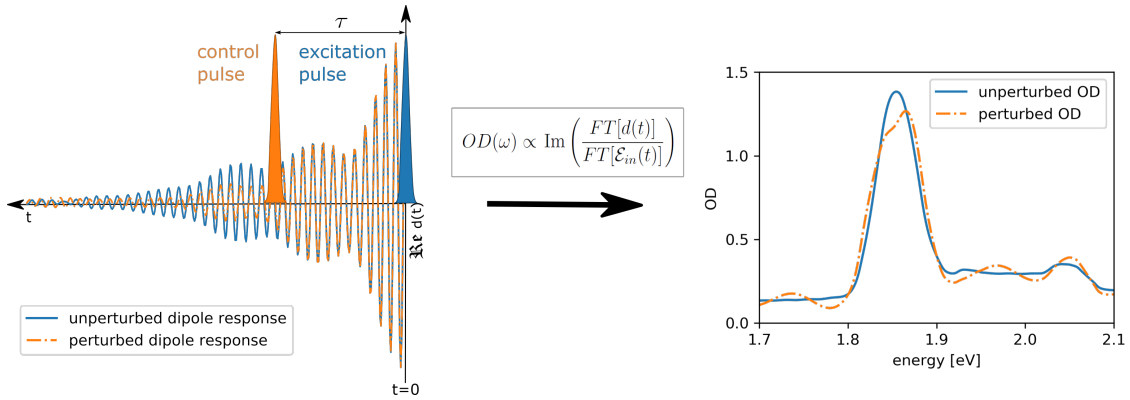

Figure 5.1.: Schematic illustration of the time-domain control of the optical dipole response. The excitation pulse (illustrated in blue) initiates the system's dipole response $d(t)$ at time $t = 0$. The dipole response subsequently evolves freely in time for $t > 0$ (blue solid curve). At a time $t = \tau$ a second pulse, denoted here as the control pulse (orange), interacts with the dipole response, resulting in a perturbed dipole response (orange dashed curve) which deviates from the unperturbed dipole response for $t > \tau$. The system's absorbance can be obtained via Fourier transformation of the real-time dipole response. For further discussions of this concept the reader is referred to [31]. Image adapted from [88].

To coherently control the dipole response, a conventional pump-probe transient-absorption scheme "in reverse" is used. In this case, the weak pulse fulfills the task to excite the system of interest (it will, therefore, be called excitation pulse in the following), while the (more intense) second pulse — referred to as the control pulse — arrives later and has the possibility to perturb the excitation-pulse induced target-specific dipole response. A schematic illustration of the measurement concept used

within this thesis is depicted in Figure 5.2.

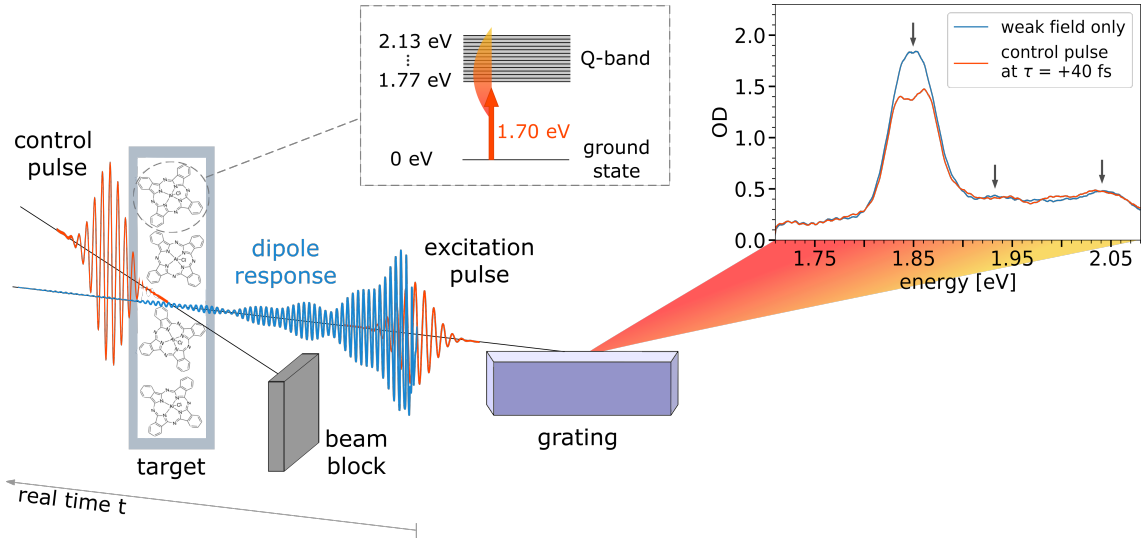

Figure 5.2.: Schematic illustration of the measurement concept. Pulses propagate from left to right, so the elapsed real time increases from right to left. The pulse configuration is depicted for positive delay times, where the time-delayed control pulse modifies the induced dipole response (depicted in blue). Exemplary absorption spectra are shown for the case of very late control delays in blue (effectively "weak field only"), where the control pulse does not change the dipole response anymore, as well as for the time delay $\tau = +40$ fs, where the control pulse significantly perturbs the probe-induced dipole response. Black arrows denote the position of the Q_I-, Q_{II}- and Q_{III}-band. The inset shows an atom-like level scheme which is used for modeling the absorption bands of AlClPc. Image adapted from [88].

The preceding weak excitation pulse induces a freely decaying dipole response (depicted in blue) in the target, which in turn can be understood as the coupling between the ground state and the excited states of the Q-band (shown as a level-scheme in the inlet of Figure 5.2). The interference of both, the dipole response in time with the excitation pulse itself, is dispersed by a grating and measured as a function of energy, leading to the (unperturbed) absorption spectrum depicted in blue. Provided the control pulse arrives in a time window between the generation and the complete decay of the dipole response, it is able to disturb the system by modifying the dipole response, resulting in changes upon the measured weak-field absorption spectrum (depicted in red color). In the case the control pulse interacts with the target first, it can also induce a dipole response with which the now succeeding weak pulse can interact. Nevertheless, since the control pulse (and its co-propagating control-pulse induced dipole response) is blocked after the target, only the weak-field induced dipole response is detected in the experiment. Spatially separating excitation and control pulse is possible due to the non-collinear focusing geometry of the experimental setup

presented in chapter 3.

5.2. Data evaluation

5.2.1. Method 1 - Direct reference method : transient correction function

Since for the measurement performed using method 1 no proper in-situ pulse characterization was conducted, the pulse duration was estimated by fitting the instrument response function (IRF) on the lineout of the ground-state bleach of the Q_I-band over the time delay, leading to a response time/pulse duration of 32.7 fs +/- 0.8 fs (FWHM). The knowledge of the pulse duration is important, since too high peak intensities of the laser pulses have to be avoided as they could damage the sample. In addition, the knowledge of the pulse duration is important for the interpretation of the measurement data. The lineout of the Q_I-band, as well as the corresponding fit to extract the pulse duration can be seen in Figure 5.3 as a function of the time delay between excitation and control pulse.

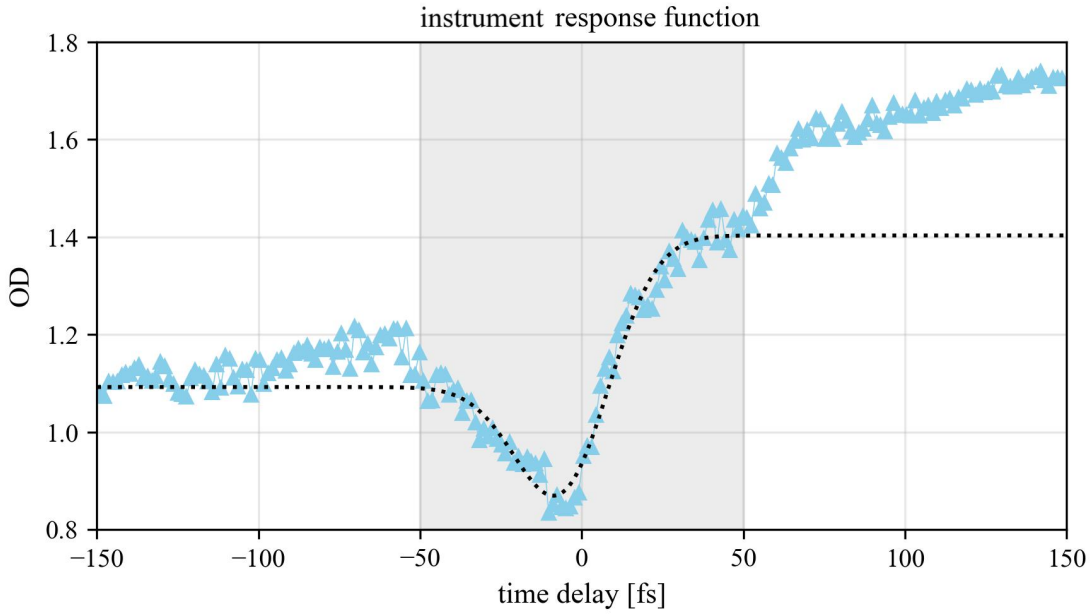

Figure 5.3.: Fit of the instrument response function on the lineout of the Q_I-band as a function of the excitation-control pulse time delay. The fit function (5.1) was applied in the gray shaded pulse-overlap area. Negative time delays denote control pulse first, positive times denote excitation pulse first. Image adapted from [88].

As a fit function, a convolution between a Gaussian, a Heaviside and an exponential function for the instrument response function is used:

$$f_{\mathrm{IRF}}(t) = \left(\left(\frac{A}{\sqrt{2\pi\sigma^2}} e^{-\frac{t^2}{2\sigma^2}} \right) * \left(\Theta(t) \cdot \left(c + B \cdot e^{-\frac{t}{\tau}} \right) \right) \right) + b, \tag{5.1}$$

with constants b and c, representing the total offset and the height of the step, while A and B are constants for the amplitude of the IRF and the exponential decay, respectively. σ describes the width of the instrument response function and τ its exponential relaxation time. The fit was applied on the gray shaded area around the temporal overlap of the pulses as depicted in Figure 5.3.

As already mentioned in chapter 3, the referencing in measurement method 1 is realized for each individual spectrum by the presence of the beamsplitter which transmits 80% and reflects 20% of the beams' intensity. Transmitted and reflected beamlets, therefore, differ in their spectral intensity distribution due to an imperfect reflectivity of the beamsplitter. To compensate for this, a calibration factor $c(\omega)$ is implemented, which corrects for the relative intensities between the signal and reference spectra introduced by the beamsplitter. To determine the calibration factor $c(\omega)$, a measurement with an empty cuvette in the target focus was conducted. Thereby, $c(\omega)$ is defined via

$$c(\omega) = \frac{I^0_{sig}(\omega)}{I_{ref}(\omega)}. \tag{5.2}$$

In addition, a time-delay scan with a, solely, solvent-filled cuvette was performed to ensure that the used solvent does not introduce any time-dependent spectro-temporal structures. An overview of the beamsplitters frequency-dependent reflectance is provided in the appendix of this thesis (see A.4).

5.2.2. Method 2 - Low dispersion method : alternative referencing

Since direct referencing is not possible with the low dispersion measurement scheme, the liquid sample was characterized before exposing it to the strong-field laser. By characterizing the weak field absorption beforehand, one gets an unperturbed estimate of the absorption which can later-on be modified using the strong laser fields. Furthermore, it can be estimated whether the sample was properly created, such that only the monomeric state is present. The white-light weak-field ground state absorption of the sample (green curve), as well as the pure solvent used (orange curve) are depicted in Figure 5.4. As can directly be seen, both ODs show an off-resonant absorption

background of approximately 0.25, which is flat and featureless. The dissolved AlCPc molecules show a clean absorption spectrum indicating that the monomeric state is prominent.

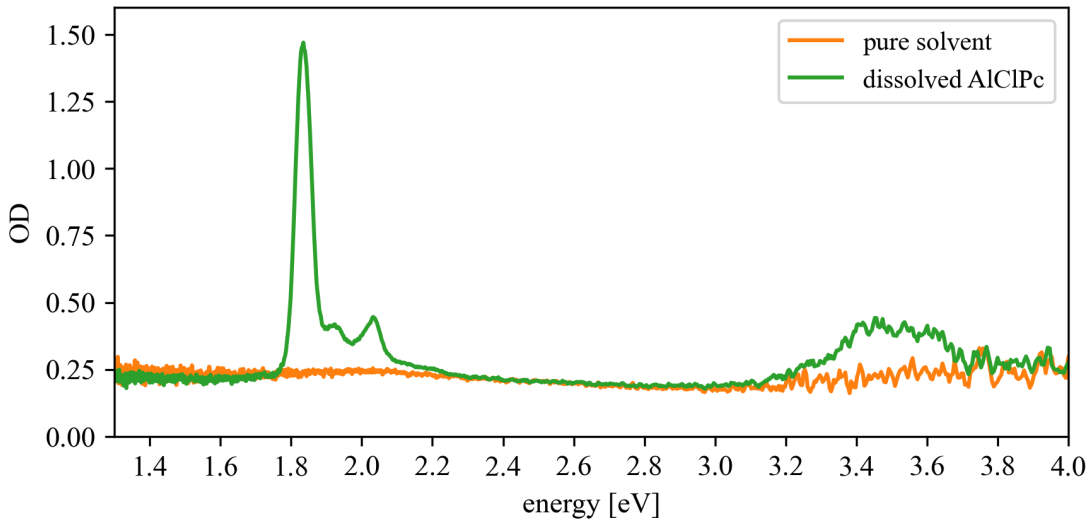

Figure 5.4.: White-light weak-field ground state absorption of the pure solvent (orange curve) and the dissolved AlClPc molecules (green curve) determined with the characterization setup presented in chapter 5.4. Both absorption spectra show a non-resonant featureless absorption background of approximately 0.25 OD. The shape of the AlClPc absorption suggests that the molecules are present in the monomeric state.

The importance of the characterization of the weak-field absorption becomes clear when taking a look at Figure 5.5, which shows the ground state absorption of the same pure solvent cuvette in the presence of the intense white-light generated in the hollow-core fiber. Here, the laser spectrum is depicted as a re-scaled blue curve together with the gathered solvent absorbance. It can be seen that the, beforehand, structureless non-resonant absorbance gets imprinted by the structured laser spectrum. Such artifacts may arise since the alternative referencing scheme cannot compensate for intensity and spectral fluctuations, as the transmitted spectra through the target and the reference spectra are measured in succession and not simultaneously.

Next to the pulse's spectrum, its temporal duration and structure (pre-/post-pulses, pedestals, etc.) are important key parameters when performing time-dependent absorption spectroscopy. For the determination of the pulse's temporal duration, defined by its FWHM, an in-situ D-Scan measurement was performed.

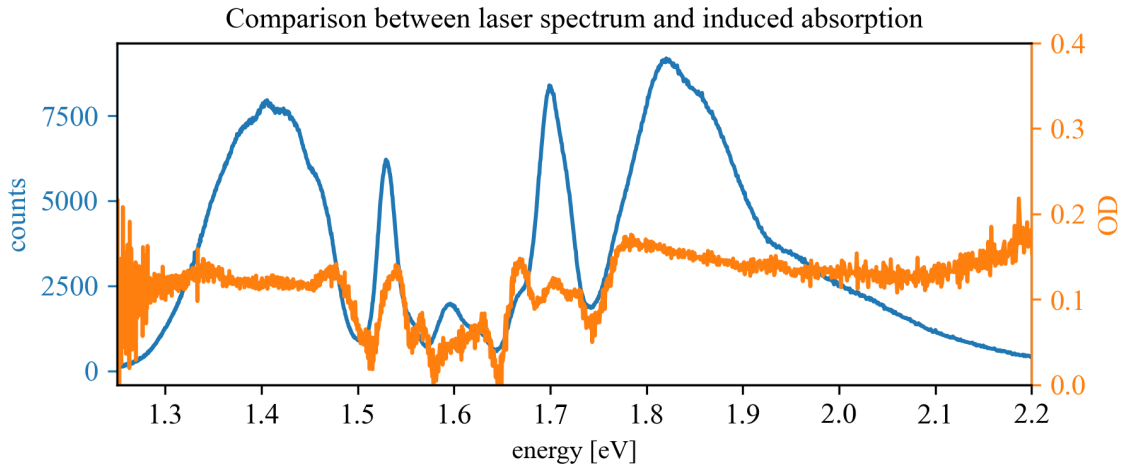

Figure 5.5.: Comparison between the white-light spectrum generated in the hollow-core fiber (blue) and the "induced" modulation on the OD of the pure solvent (orange). Due to the different referencing scheme, intensity as well as spectral fluctuations of the hollow-core fiber generated spectrum can imprint on the absorbance, leading to artifacts shaped in the manner of the input spectrum.

Therefore, the BBO-crystal was placed in the focal plane of the experimental setup and both attenuators adjusted, such, that an SHG-signal could only be generated when both beams overlap in time and space. In spite of the detection limit of both camera and spectrometer, which prohibit the detection of the complete spectral range of the SHG-signal, good qualitative agreement can be found between the measured and the retrieved D-Scan trace, as can be seen in Figure 5.6.

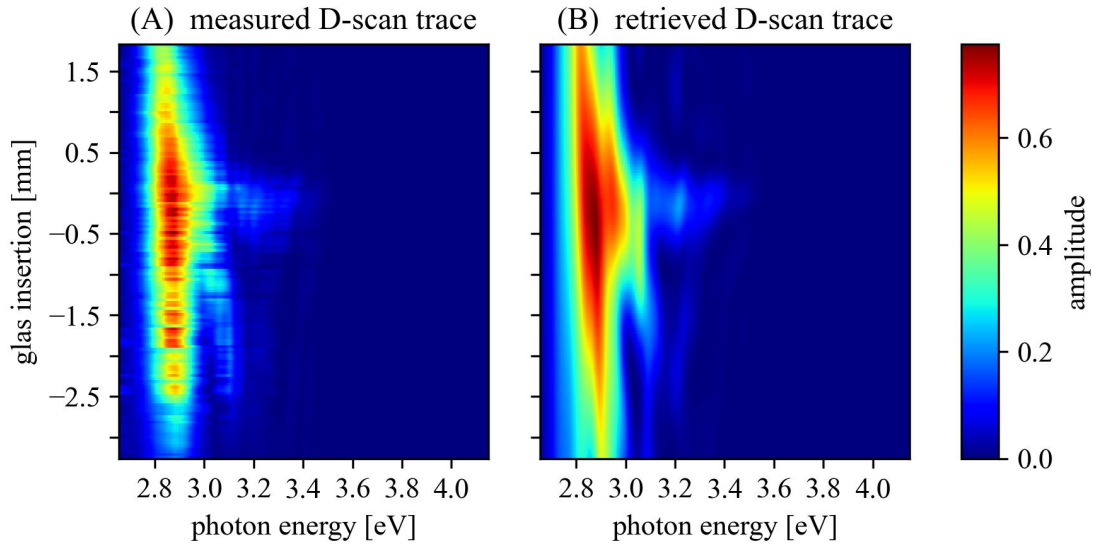

Figure 5.6.: Experimental and retrieved D-Scan traces. The in-situ measured D-Scan trace is depicted in panel (A), while the retrieved trace is shown in panel (B). The theoretically determined D-Scan trace shows good qualitative agreement with the experimental data.

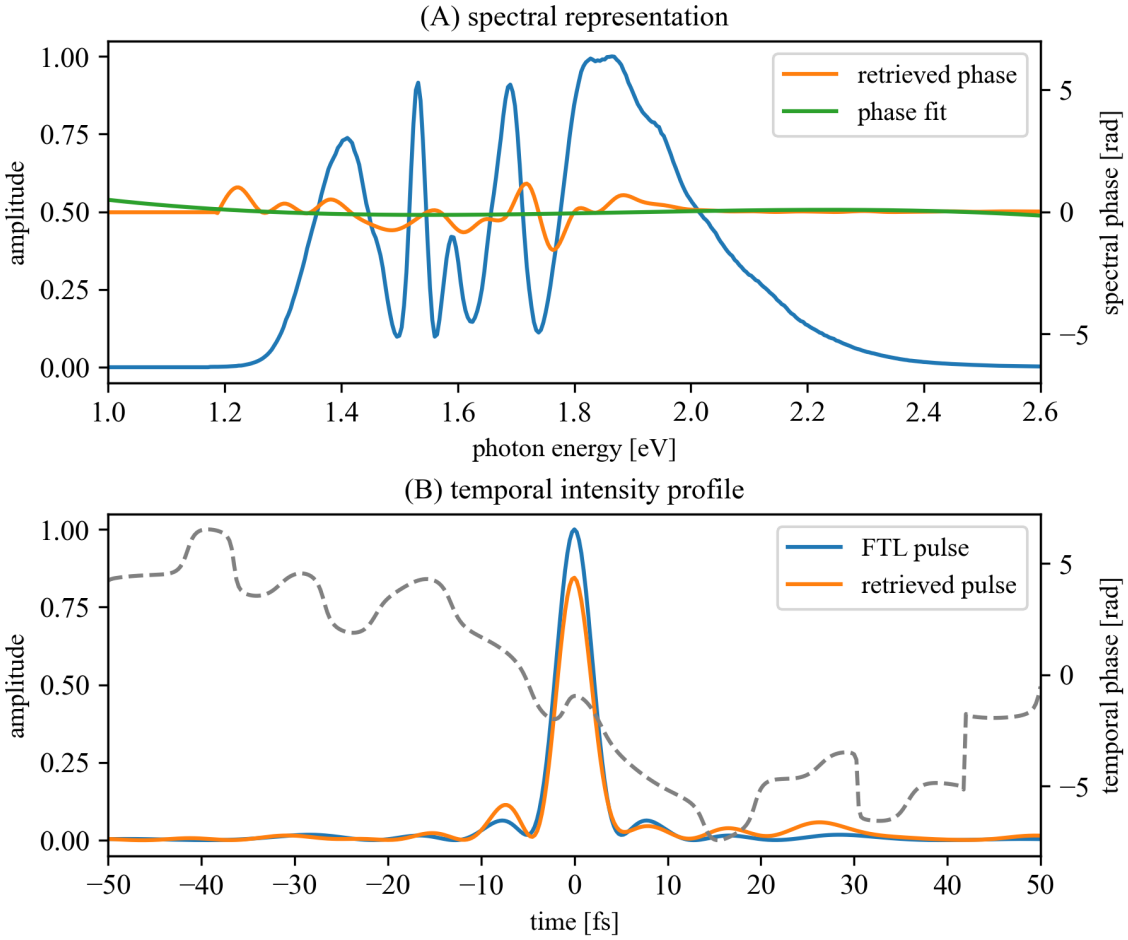

Figure 5.7.: Results obtained via the D-Scan retrieval algorithm. Fig. 5.7(A) shows the measured fundamental spectrum in blue, as well as the retrieved spectral phase in orange. By fitting the spectral phase, the green transient can be obtained, indicating a residual third-order dispersion. In Fig. 5.7(B) the intensity profile of the retrieved temporal pulses are shown. The intensity profile of the Fourier transform limited (FTL) pulse is depicted in blue, which is obtained by the measured fundamental spectrum under the assumption of a flat spectral phase. The orange transient shows the optimum pulse which can be achieved when the spectral phase equals the retrieved phase (depicted in orange in Fig. 5.7(A)). In addition the temporal phase is displayed as a gray dashed line.

The retrieval (see chapter 3.3) obtains a complex spectral phase with a frequent fast modulation over the pulses' spectral energy range, depicted as orange curve in Figure 5.7(A). Fitting the retrieved phase with a polynomial of order 3, the green curve can be obtained with the fit parameters: GDD = 0.436 fs^2 and TOD = -2.436 fs^3. Figure 5.7(B) displays the retrieved temporal structure of the pulse. The blue curve shows the intensity profile of the Fourier transform limited (FTL) pulse. This is provided by the measured fundamental spectrum under the assumption of a flat spectral phase. As can be seen the FTL pulse shows already pre- and post-pulses,

which are linked to the non-Gaussian fundamental pulse spectrum. The orange curve shows the shortest pulse which can be achieved when the spectral phase equals the retrieved phase. As can be seen there are minor deviations from the FTL case due to higher-order phase contributions. In addition, the temporal phase is depicted as a dashed gray line. By performing a Gaussian fit on both, the blue and orange intensity profile, the respective pulse durations (FWHM) can be obtained. The FWHM of the FTL pulse is 4.1 fs, while the FWHM of the optimum retrieved pulse is 4.4 fs with a pulse contrast of 7.4. The pulse contrast is defined as a measure of the intensity ratio between the main pulse (centered at 0 fs) and its most intense pre-/post-pulse.

5.3. Results

After presenting both types of data evaluation, including their advantages and disadvantages, the experimental results are summarized in this section separated by the used measurement method. An overview of the method-specific laser-pulse parameter is given in Table 5.1:

method	pulse duration (FWHM)	excitation pulse peak power	control pulse peak power
1	32.7 fs	$3.2{\cdot}10^{10}$ W/cm^2	$1.7{\cdot}10^{11}$ W/cm^2
2	4.4 fs	$4.2{\cdot}10^{10}$ W/cm^2	$(3.3 \cdot 10^{11}$ - $2.9 \cdot 10^{12})$ W/cm^2

Table 5.1.: Individual method-specific laser-pulse parameter. Please note that the presented pulse durations were estimated with different characterization techniques.

5.3.1. Method 1: Direct reference method

For the presented measurement, the excitation-beam average power was set to 0.28 mW and the control average power to 4.0 mW, which correspond to on-target peak intensities of $3.2 \cdot 10^{10}$ W/cm^2 and $1.7 \cdot 10^{11}$ W/cm^2, respectively. Both transmitted signal through the target as well as the corresponding reference spectra were recorded for excitation-control time delays between -180 fs and +150 fs with an incremental step size of 1.33 fs. Positive time delays denote the weak excitation pulse preceding the intense control pulse. Laser-induced control of the dipole response induced by the weak excitation pulse is, therefore, only possible for positive time delays $\tau > 0$. Taking

the calibration factor $c(\omega)$ into account, the optical density is calculated according to Beer-Lambert's law for each excitation-control pulse time delay τ by:

$$\mathrm{OD}(\omega,\tau) = -\log_{10}\frac{I_{\mathrm{sig}}(\omega,\tau)}{c(\omega)\cdot I_{\mathrm{ref}}(\omega,\tau)}, \tag{5.3}$$

where I_{sig} and I_{ref} are the frequency- and time-delay dependent signal and reference spectral intensities.

The measured weak-field static absorption of AlClPc's Q-band is shown in blue in the inset of Figure 5.2. It spans the spectral range between 1.80 eV and 2.08 eV, while the highest contribution to the ground-state absorption is given by the Q_I-band, centered at 1.85 eV. The other two Q-bands, Q_{III} (centered at 2.04 eV) and Q_{II} (at 1.93 eV) are only faintly visible, as expected from literature [49].

Using equation 5.3, the time-delay-dependent absorption $\mathrm{OD}(\omega,\tau)$ is calculated and depicted in Figure 5.8. For a better contrast of the induced dynamics, the relative optical density ($\Delta\mathrm{OD}(\omega,\tau)$) was calculated by subtracting the weak-field static absorption spectrum from the time-delay-dependent absorption trace. Thereby, the weak-field static absorption was determined by the average of the optical density for the time delays between +140 fs and +150 fs, where the influence of the control pulse on the absorption cannot be observed. For these late time delays, the laser control of the excitation-pulse induced dipole response is no longer possible, since it has decayed completely.

The most pronounced feature that can be seen in the time-delay-dependent absorption (depicted in Fig. 5.8) is the decrease of the Q_I-band for negative time delays (control pulse passes through the target first). This effect can simply be explained by a ground-state bleach [89, 90]. Since the control pulse passes through the target first, it transfers a significant amount of population from the ground to the excited states, which in turn results in a lowered ground-state absorption of the (measured) excitation pulse. This effect is known and expected in pump-probe transient absorption spectroscopy. For positive time delays, where the control pulse arrives after the excitation pulse, a time-delay dependent modulation on the absorption spectrum can be seen between 1.85 eV and 2.10 eV. Which is exactly what has been expected and already motivated in the measurement concept (see section 5.1). To guide the reader's eye, the area of interest is marked in Figure 5.8(B) with a white box. The slow spectral modulations, which are a result of the perturbation of the dipole response by the control pulse in the time domain, can be observed for positive time delays

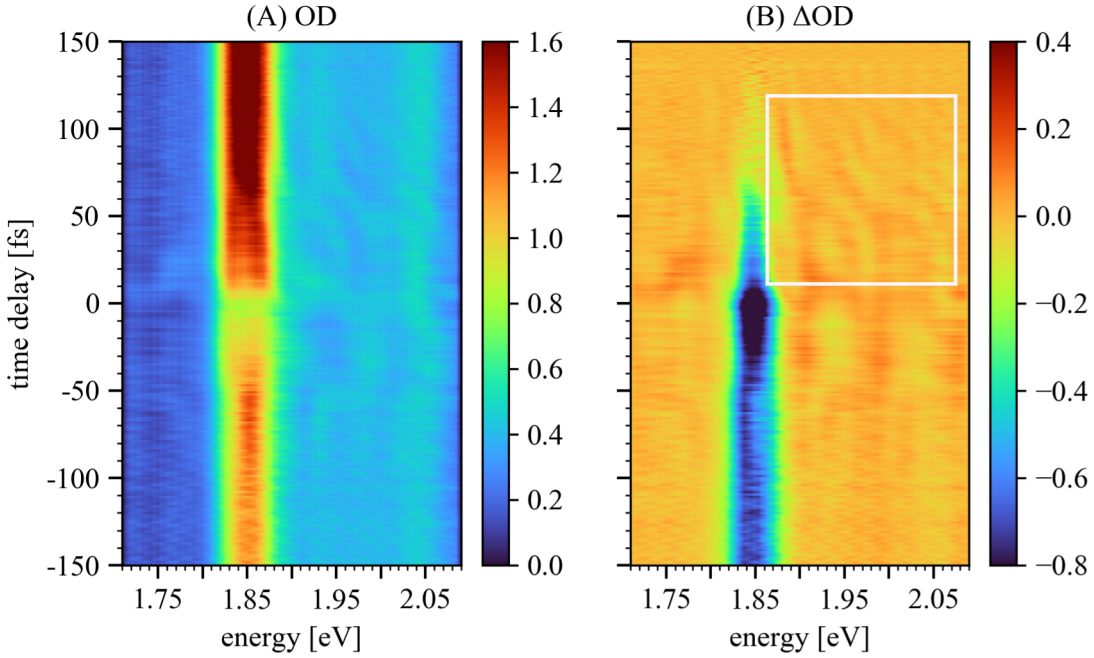

Figure 5.8.: Time-delay-dependent absorption $\mathrm{OD}(\omega, \tau)$ (A) and relative absorption $\Delta\mathrm{OD}(\omega, \tau)$ (B) of AlClPc's Q-bands. A solvent consisting of 2/3 ethanol and 1/3 water was used. In the presented ΔOD (B), the control-induced changes of the excitation-pulse induced dipole response in AlClPc are highlighted with a white box. At negative/positive times, the control pulse arrives before/after the excitation pulse, which is centered at time $\tau = 0$ and induces a coherent dipole response for times $\tau > 0$. The color bars represent the magnitude of the optical density. Image adapted from [88].

only and approximately up to a time delay of +100 fs. This implies that coherent manipulation of the excitation-pulse induced dipole response is still possible at these relatively long time scales even in the liquid phase. Furthermore, a slight splitting of the Q_I-absorption band can be observed for positive time delays between 0 fs and approximately 50 fs. In addition to the aforementioned features, faint rapid fringes can be seen symmetrically for both positive and negative time delays centered around the pulse overlap at $\tau = 0$. These occur due to white-light interference of residual stray light of the control beam with the excitation beam.

To verify the origin of the observed spectro-temporal effects, a Fourier transform along the delay axis of the ΔOD trace is performed for positive and negative time delays separately. The results are shown in Figure 5.9. This procedure is commonly used in atomic targets to reveal the couplings of different states by plotting the Fourier energy over the absorption's spectral energy [31, 40, 44]. In these 2D representations, diagonals with slopes of +/-1 intersecting the spectral energy axis, have been identified

to indicate the manipulation of the coherent dipole response of this particular state for a variable time delay between excitation and control pulses [31]. In addition, coherent couplings between different states can be seen by enhancements in the Fourier amplitude along these diagonals [44]. Looking at Figure 5.9(A) the aforementioned diagonals with a slope of +/-1 arising at a spectral energy of approximately 1.85 eV can be observed, which can be associated with the Q_I-band. While the Fourier energy plot, calculated for positive time delays only, shows a rich and complex structure in general, thereby, indicating that coherent control is taking place within this time-delay window, the plot for negative time delays only shows a globally enhanced signal around the Q_I-band indicating that the aforementioned couplings do not take place for negative time delays.

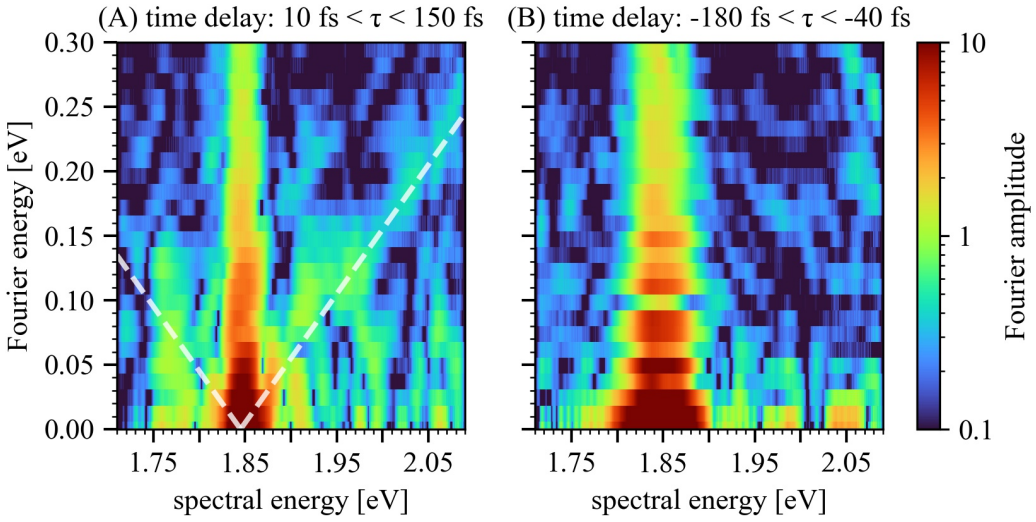

Figure 5.9.: Fourier energy plot for positive (A) and negative (B) time delays of the $\Delta\mathrm{OD}(\omega, \tau)$ shown in Figure 5.8(B). Diagonals with a slope of +/- 1 pointing at the spectral energy of the Q_I-band can be observed only for positive time delays. The diagonals are highlighted via white semitransparent dotted lines in panel (A). Image adapted from [88].

The pinpointed significant differences between both Fourier energy plots confirm that the observed diagonals are associated with the laser-driven dipoles. For positive time delays, the control pulse is able to perturb the excitation-pulse induced dipole response of the target, leading to the diagonal features in the Fourier plot for positive time delays. A further confirmation of the underlying origin of the observed effects in the time-delay trace, as well as their corresponding Fourier energy plot will be discussed in chapter 6.1 by employing an atom-like multi-level model calculation.

5.3.2. Method 2: Low dispersion method

For the measurement conducted via method 2, the excitation-beam's average power was set to 0.075 mW. Given the focal size of 120 μm and the pulse duration of 4.4 fs, as retrieved via the D-scan method described in section 5.2.2, this corresponds to an on-target peak intensity of $4.2 \cdot 10^{10}$ W/cm^2, which is comparable to the peak intensity used for the previous measurement. To get an insight on how the control-pulse intensity might change the excitation-induced dipole moment, the aforementioned measurement routine was conducted for different control-pulse intensities. For a better overview, the different time-delay scans are denoted from case **A**-**E** where **A** denotes the lowest and **E** the highest control-pulse intensity. The average power, as well as the peak intensity (taking into account the control-beam focal size of 130 μm and the pulse duration of 4.4 fs) are summarized in Table 5.2. The lowest chosen control-pulse intensity of 3.32 $\cdot 10^{11}$ W/cm^2 (case **A**) is comparable to the measurement shown in method 1, while (case **B**-**E**) extend the measurement to higher on-target peak intensities.

case	control pulse average power	control pulse peak intensity
A	0.520 mW	3.32 $\cdot 10^{11}$ W/cm^2
B	0.835 mW	5.32 $\cdot 10^{11}$ W/cm^2
C	1.640 mW	1.05 $\cdot 10^{12}$ W/cm^2
D	2.800 mW	1.79 $\cdot 10^{12}$ W/cm^2
E	4.500 mW	2.87 $\cdot 10^{12}$ W/cm^2

Table 5.2.: Chart with the control pulse's chosen average power, corresponding to the different Subfigures **A**-**E** in Fig. 5.10 and Fig. 5.11, as well as the calculated respective peak intensities.

The transmitted signal (consisting of the excitation field superimposed with the sample's response) is recorded for excitation–control time delays between -200 fs and + 200fs with an incremental step size of 0.665 fs, while the control beam is spatially blocked after the sample. The same time-delay scans are conducted for each intensity with a cuvette filled with the pure solvent to get the corresponding reference spectra once, while the scans with the dissolved AlClPc molecules were conducted five times. Positive time delays denote the weak excitation pulse preceding the intense control pulse. The laser-induced control of the dipole response induced by the weak excitation pulse is only possible for positive time delays $\tau > 0$. Besides the different incremental time-delay step size, also the spectrometer settings where changed (compared to the

previous measurement) by using the overview grating, enabling the possibility to measure the complete broadband spectrum that surpasses the target.

The optical density is calculated according to Beer-Lambert's law for each excitation-control pulse time delay τ by:

$$\mathrm{OD}(\omega, \tau) = -\log_{10} \frac{I_{\mathrm{sig}}(\omega, \tau)}{I_0(\omega)}, \tag{5.4}$$

where I_{sig} is the frequency- and time-delay dependent spectral intensity and $I_0(\omega)$ the reference spectral intensity, which was estimated by moving the sample out of the focus. Using equation 5.4, the time-delay-dependent absorption $\mathrm{OD}(\omega, \tau)$ is calculated and depicted for the dissolved target, as well as the pure solvent in Figure 5.10 (intensities **A**-**C**) and Figure 5.11 (intensities **D**, **E**).

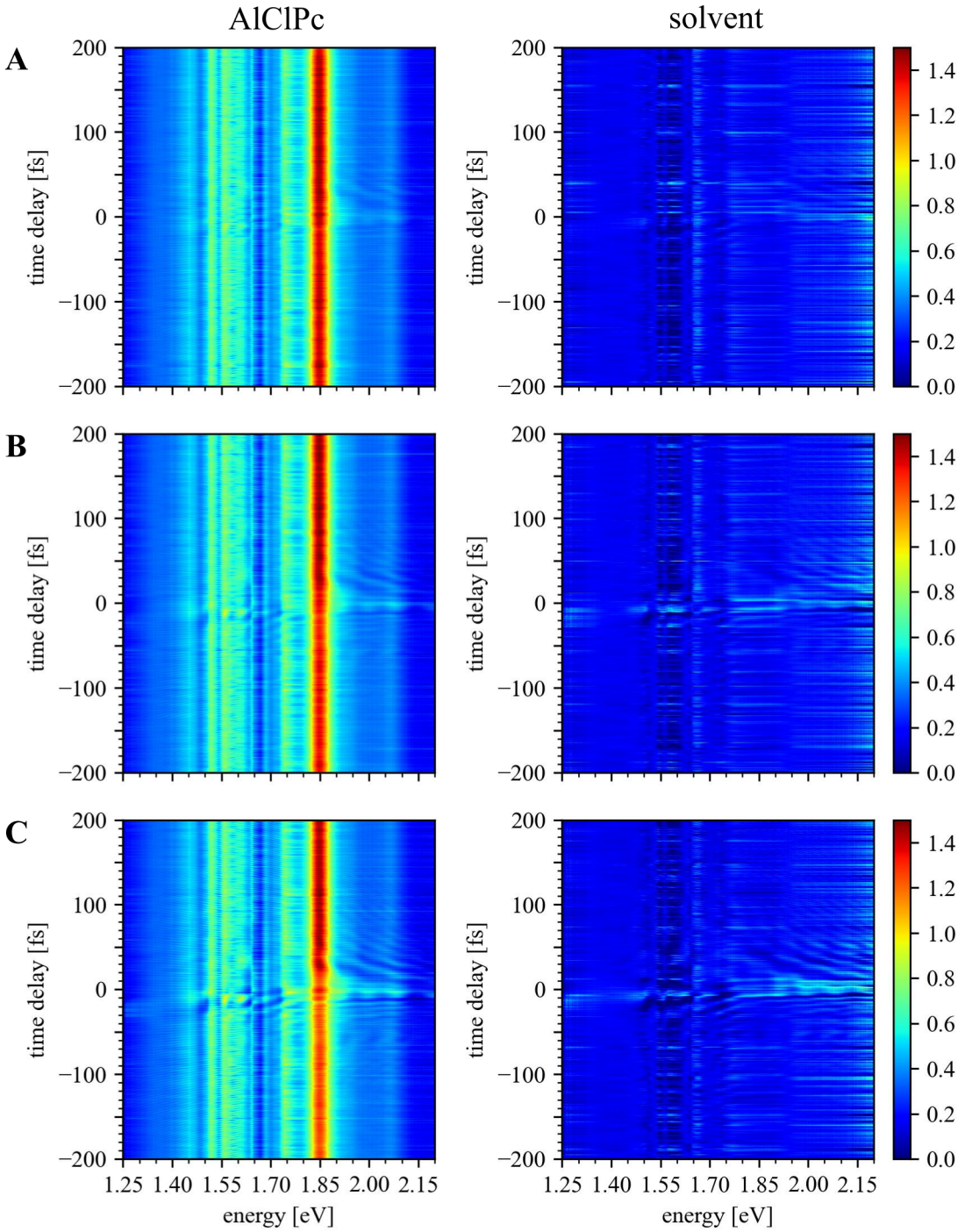

Figure 5.10.: Measured time-delay-dependent absorption $\mathrm{OD}(\omega, \tau)$ for the dissolved AlClPc molecules (first column), as well as the respective measurement conducted in the pure solvent, which consisted of 70% ethanol and 30% water (second column) for the control-pulse intensities **A** to **C**. At negative/positive times, the control pulse arrives before/after the excitation pulse, which is centered at time $\tau = 0$ and induces a coherent dipole response for times $\tau > 0$. The color bars represent the magnitude of the optical density.

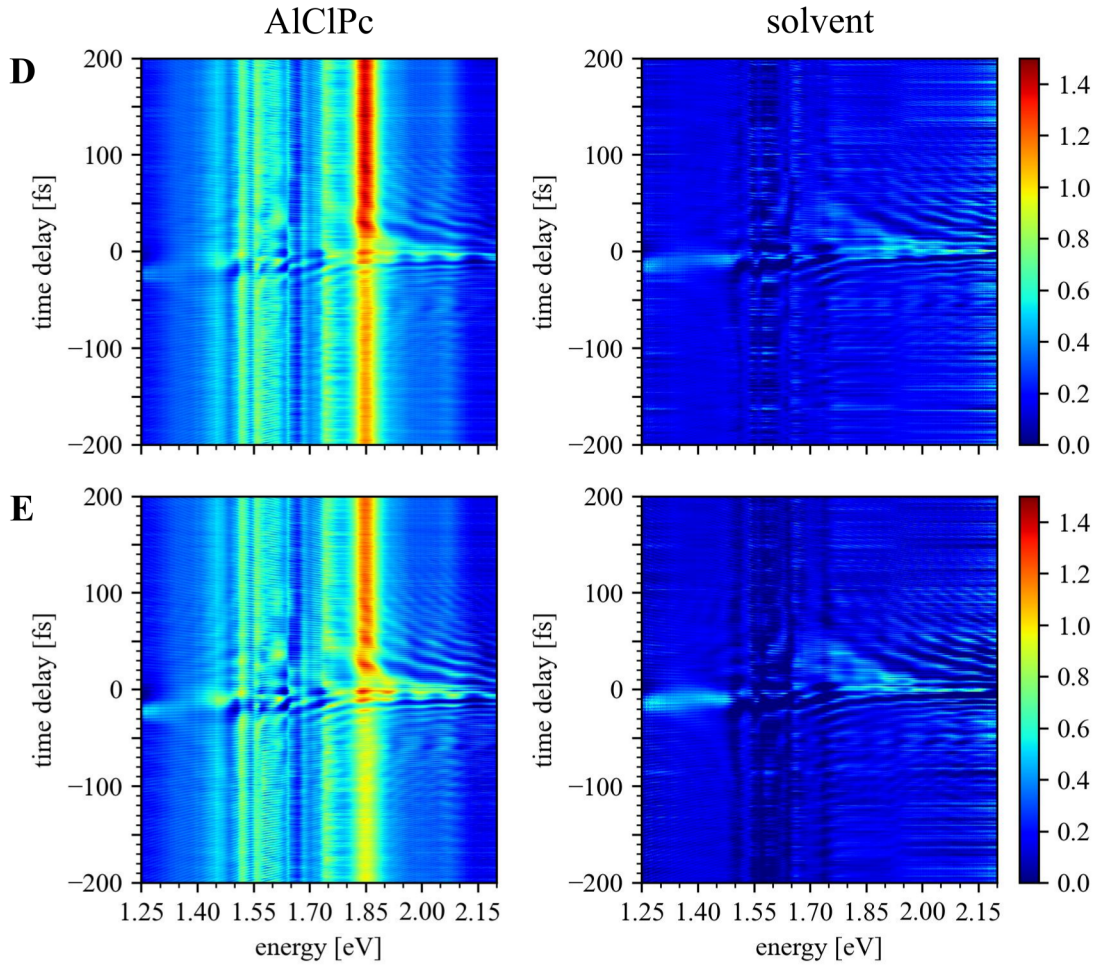

Figure 5.11.: Measured time-delay-dependent absorption $\mathrm{OD}(\omega, \tau)$ for the dissolved AlClPc molecules (first column), as well as the respective measurement conducted in the pure solvent, consisting of 70% of ethanol and 30% of water, depicted in the second column for the intensities **D** and **E**. At negative/positive times, denote the control pulse arriving before/after the excitation pulse, which is centered at time $\tau = 0$ and induces a coherent dipole response for times $\tau > 0$. The color bars represent the magnitude of the optical density.

The sample's weak-field static absorption was measured directly prior to the strong-field measurement campaign using the sample characterization setup and is depicted in subsection 5.2.2. As was shown in Figure 5.4, the sample's Q-band spans the spectral range between 1.80 eV and 2.1 eV, while the highest contribution to the ground-state absorption is given by the Q_I-band, centered at 1.85 eV. The other two Q-bands, Q_{III} (centered at 2.04 eV) and Q_{II} (at 1.93 eV) are only faintly visible, as expected from literature [49]. Since the white-light, generated in the hollow-core fiber, does not exceed the spectral energy range beyond 2.5 eV, the Soret-band is not visible

in the absorption spectra.

The most pronounced absorption feature that can be seen throughout the time-delay-dependent absorption traces, independent of the control-pulse intensity is the Q_I-absorption band centered at a photon energy of 1.85 eV. In addition, all traces show vertical lines for energies smaller than 1.80 eV. It has to be noted, that these lines are no "real" absorption lines but remnants of the pulse spectrum as previously shown in Fig. 5.5. This artifact arises here by a combination of the intensity-dependent remaining off-resonant absorption of the medium itself and the missing of the direct referencing. These "lines" will, therefore, be neglected in the following. As already expected from the results of measurement 1, a decrease of the time-delay-dependent absorption of the Q_I-absorption band for negative time delays can be seen. When comparing the traces for different control-pulse intensities, it can be seen that this ground-state bleach becomes more pronounced for higher intensities, as expected. The higher the control-pulse intensity the more population is transferred from the ground- to higher excited states, resulting in a lowered ground-state absorption of the (measured) excitation pulse.

For positive time delays, where the control pulse arrives after the excitation pulse, a time-delay-dependent modulation on the absorption spectrum can be seen between 1.85 eV and 2.20 eV, which get's more pronounced for increasing control-pulse intensities. These spectro-temporal modulations are what has been expected and motivated in the measurement concept (see section 5.1). The slow spectral modulations, which are a result of the perturbation of the dipole response by the control pulse in the time domain, can be observed for positive time delays only. What is intriguing though, are similar spectral modulations on the time-delay dependent absorption of the pure solvent, which start to appear for control-pulse intensities **B** and higher. Especially, since neither ethanol nor water have spectral absorption lines in this energy region.

Further analysis in the time domain is difficult due to the similar features present in the OD of the dissolved AlClPc molecules and the pure solvent. To verify the origin, as well as separate the observed spectro-temporal effects, a Fourier transform along the time-delay axis of the OD traces for the lowest intensity is performed for positive and negative time delays, separately. This procedure helps to separate overlapping spectro-temporal modulations, as the resulting diagonals have a different spectral energy position in the Fourier energy plots. Therefore, further data analysis and interpretation is conducted on the corresponding Fourier energy plots, instead of directly in the time domain. The results for AlClPc and the pure solvent (for the

control-pulse intensity **A**) are shown in 5.12 and Figure 5.13, respectively.

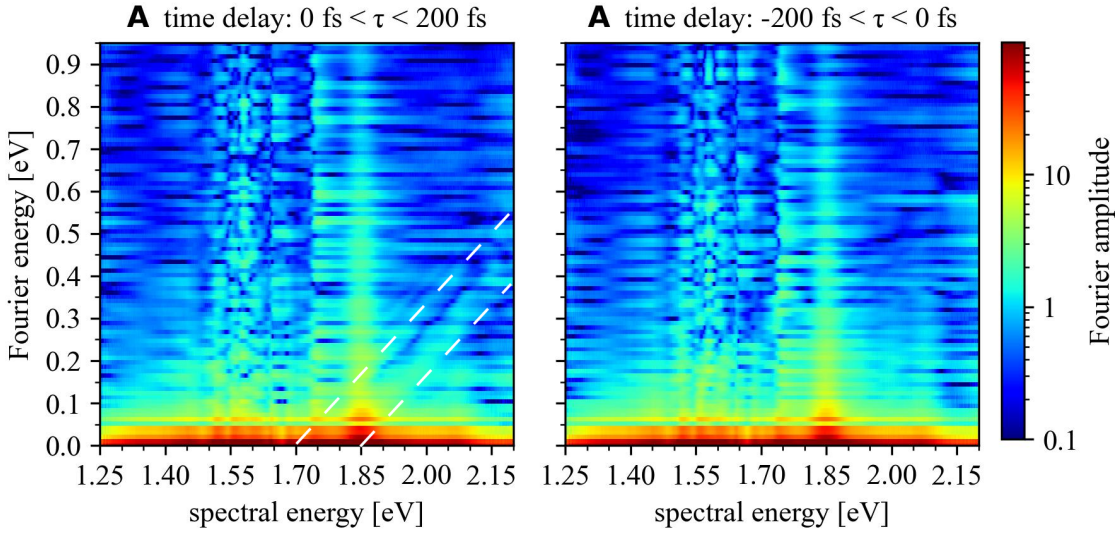

Figure 5.12.: Fourier amplitude for positive and negative time delays separately, of the time-delay-dependent absorption in AlClPc for the lowest control-pulse intensity (case **A**). In agreement with the measurement results from the previous chapter (see Figure 5.9), a diagonal with a slope of + 1 pointing at the spectral energy of the Q_I-band can be seen for positive time delays only.

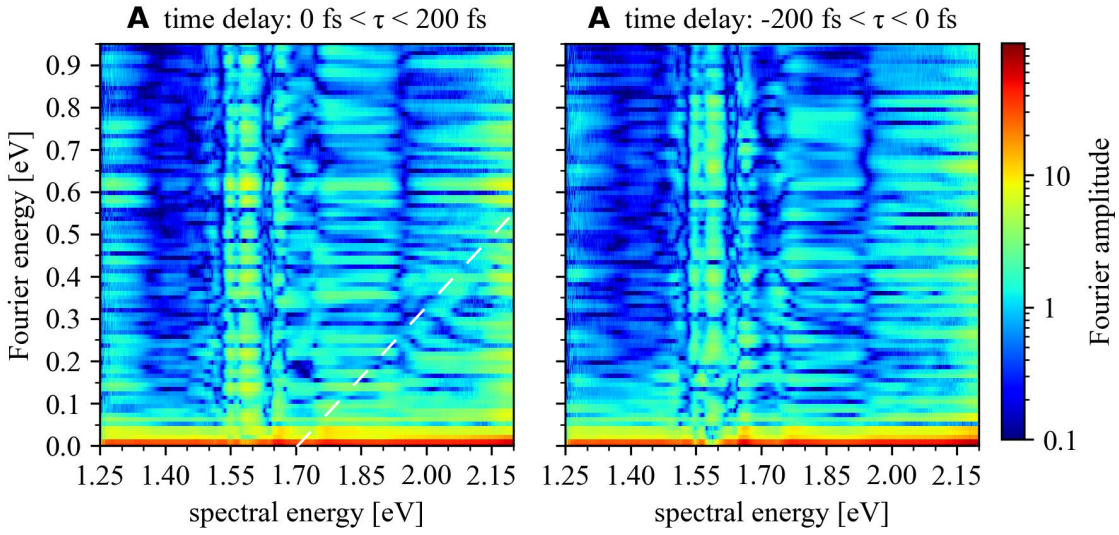

Figure 5.13.: Fourier amplitude for positive and negative time delays separately. This Fourier data belongs to the time-delay-dependent absorption in the pure solvent for the lowest control-pulse intensity **A**. An indicative diagonal with a slope of +1 pointing at a spectral energy of 1.70 eV can be seen for positive time delays only. This faintly visible diagonal can also be seen in Figure 5.12.

Looking at the left panel of Figure 5.12, which shows the Fourier amplitude for positive time delays only, the aforementioned diagonals with a slope of +/-1 arise at a spectral energy of approximately 1.85 eV (which can be associated with the Q_I-band) can be observed. While the Fourier energy plot for positive time delays shows a rich structure of diagonals, the plot for negative time delays shows a globally enhanced signal without any structure. Comparing the Fourier plot of the pure solvent for the same control-pulse intensity, no pronounced structures can be observed for negative time delays, while for positive time delays a faint diagonal with a slope of +1 starting from a spectral energy of 1.70 eV can be seen. Since neither AlClPc, nor the solvent absorb in this region resonantly, the reason for the presence of this diagonal will be investigated in chapter 6.2. As both Fourier energy plots (dissolved AlClPc, as well as pure solvent) do not contain any significant information for the case of negative time-delays only, they will be discarded from here on. In addition to the Fourier amplitude, also the Fourier phase can be retrieved through Fourier transformation of the time-dependent optical density.

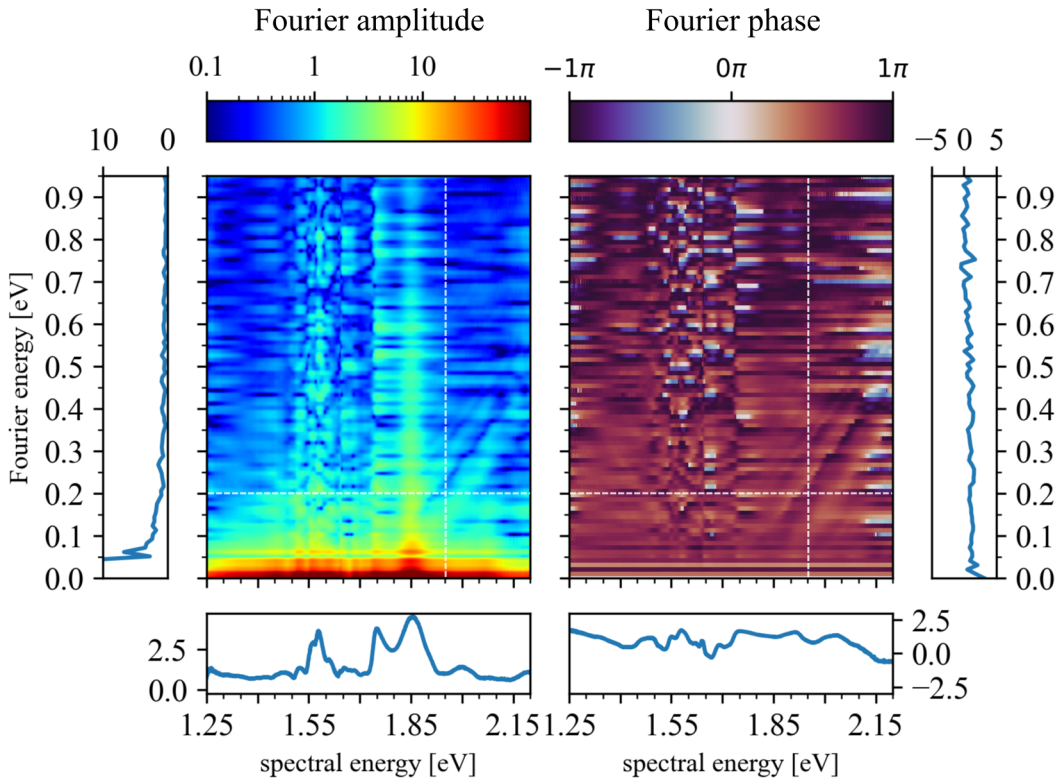

Figure 5.14.: Fourier amplitude and phase for the control-pulse intensity **A** with the dissolved AlCLPc molecules, as well as lineouts in spectral and Fourier energy for both 2D plots. The respective lineout positions are marked by white semi-transparent dotted lines in the color-plots. For the representation of the Fourier phase a cyclic colormap is used.

To allow for a better comparison between the different control-pulse intensity cases **A** to **E**, not only the 2D Fourier amplitude and Fourier phase are determined for both dissolved AlClPc as well as the pure solvent, but also lineouts through Fourier and spectral energy for both Fourier amplitude and phase are taken. Figure 5.14 shows the Fourier amplitude and phase for positive time delays for intensity **A** and AlClPc, while 5.15 shows the reference data taken in the pure solvent. The white dotted lines within the color-plots, mark the positions of the lineouts. The 1D-panels on the bottom of the color-plots show the respective spectral energy lineout at a Fourier energy of 0.2 eV, while the line-plots on the left- and right-hand side of the color-plots show the lineouts along the spectral energy at 1.95 eV.

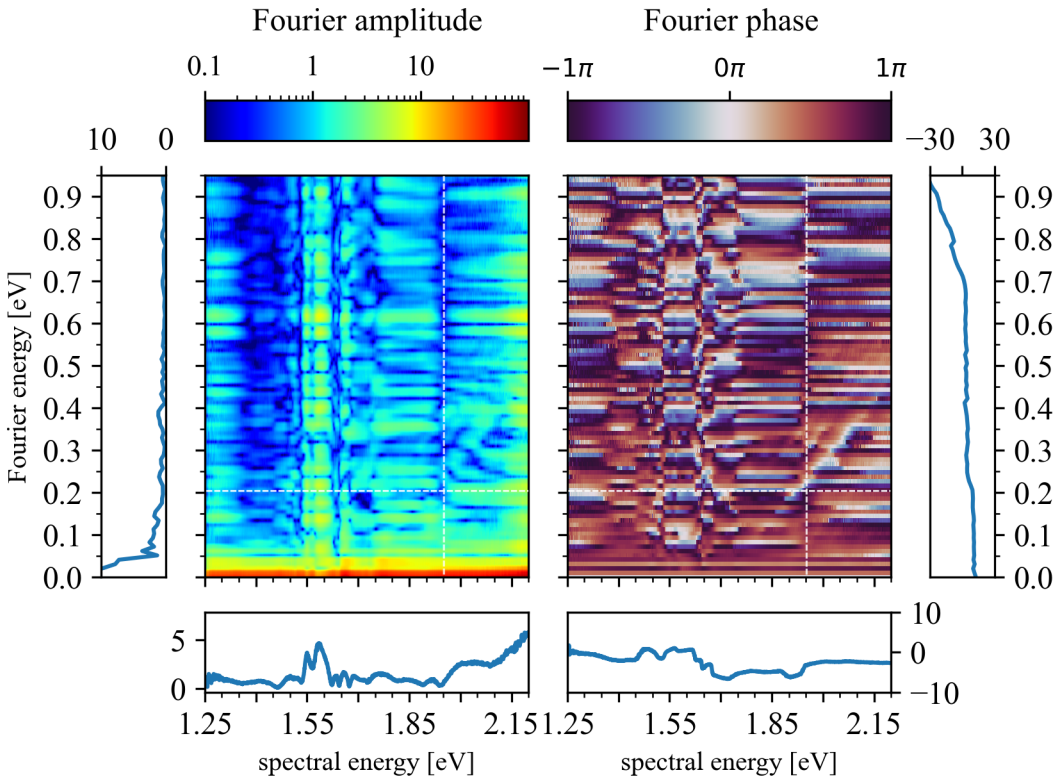

Figure 5.15.: Fourier amplitude and phase for the control-pulse intensity case **A** of the pure solvent, as well as lineouts in spectral and Fourier energy for both 2D plots. The lineout positions are marked by white semi-transparent dotted lines in the color-plots.

Please note that the Fourier phase representation in the 2D-plots is using a cyclic colorbar with a periodicity of 2π. For the lineouts, the Fourier phase is depicted in a linear fashion. Therefore, an unwrapping by 2π was conducted, leading to the phase course within the lineouts spanning several radian. The respective lineouts for all control-pulse intensities will be discussed in detail at the end of this chapter.

The Fourier amplitude and phase (for positive time-delays only) were successively calculated for both dissolved AlClPc, as well as pure solvent for all measured time-delay-dependent absorption traces depicted in Figures 5.10 and 5.11. The results of the Fourier amplitude for positive time-delays only are depicted in Figure 5.16 for the measurement data of the dissolved AlClPc molecules, and in Figure 5.17 for the comparative measurement in the pure solvent.

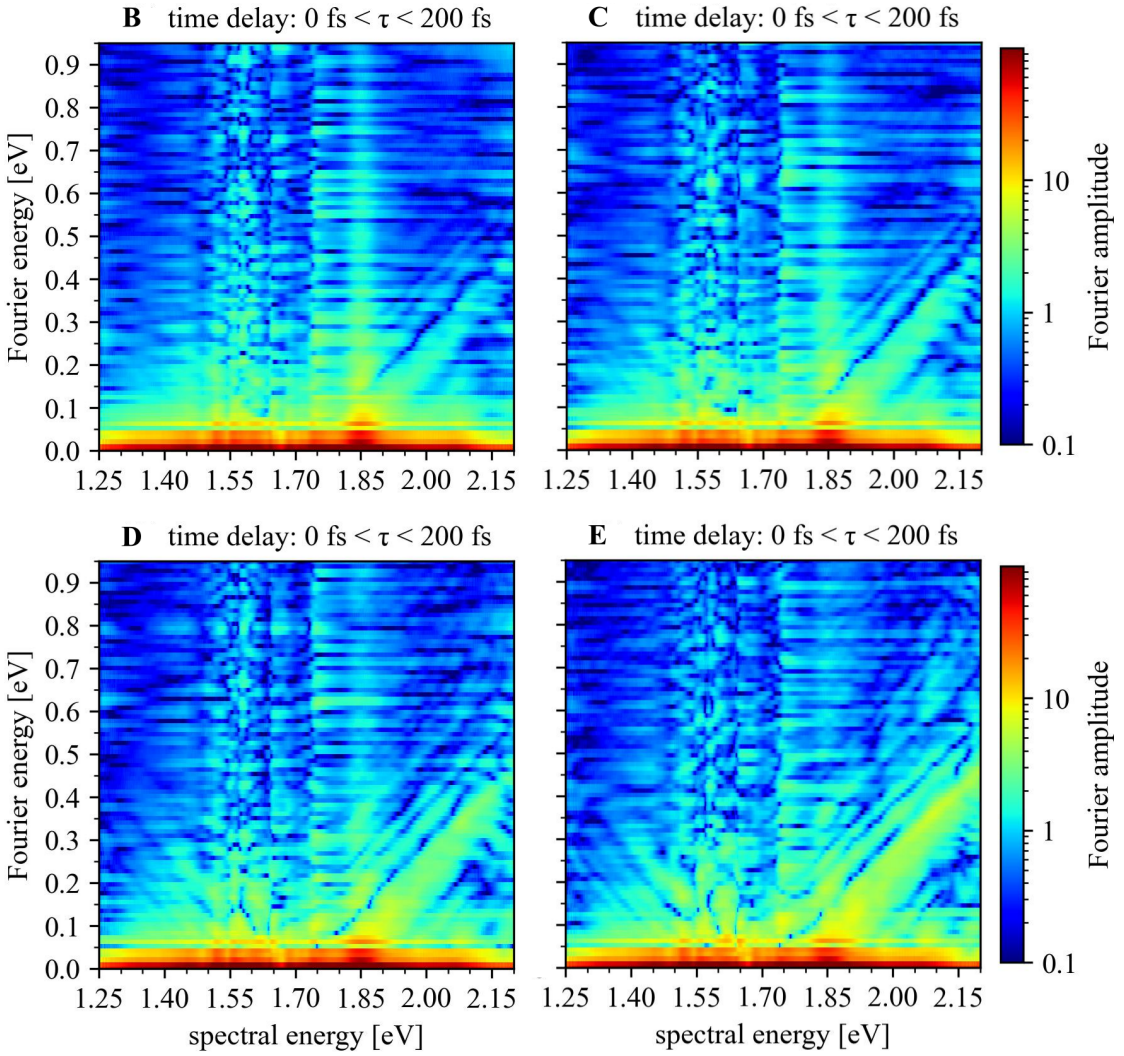

Figure 5.16.: Fourier amplitudes for control-pulse intensities **B** to **E** for the case of AlClPc. It can be seen that the amplitude of the diagonals increase with increasing control-pulse intensity, while a minimum between the two diagonals pointing at 1.70 eV and 1.85 eV emerges.

Taking a look at Figure 5.16, it can be seen that all diagonal structures get more pronounced with increasing control-pulse intensity. While for intensity **B**, the most

prominent structures are diagonals with a slope of +1, for the highest measured intensity **E**, also diagonals with slopes -1 are clearly visible. The question now arises what the specific origin of all additional diagonals is. The broadest diagonal with slope +1 arising at approximately 1.85 eV can be associated with the laser-driven dipoles of the AlClPc molecule. As already pinpointed in the previous section the control pulse is able to perturb the excitation-pulse induced dipole response, leading to the diagonal features in the Fourier plot for positive time delays. The second most pronounced diagonal runs parallel to it with a slope of +1 and intersects the spectral energy axis at 1.70 eV. Following these two diagonals over the increasing control intensity, it can be seen that while both diagonals increase with the intensity, the minimum that runs between both gets sharper and more pronounced for higher intensities (see Fig. 5.16). The aforementioned intensity-dependent effects can in detail be also seen in the lineout plots Fig. 5.20 and Fig. 5.22.

Taking a look at the comparative Fourier amplitude of the pure solvent (Fig. 5.17), it can be said that the already observed faint diagonal with slope +1 intersecting the spectral energy axis at 1.70 eV sustains for all used control-pulse intensities. In general, it can be said that the overall Fourier amplitude contributions increase for increasing control-pulse intensity, though the data of the pure solvent is more noisy (compared to the data of AlClPc) due to the lower statistics and thus makes the overall identification of diagonals more difficult. Nevertheless, the aforementioned pronounced minimum diagonal cannot be observed in the Fourier data of the pure solvent.

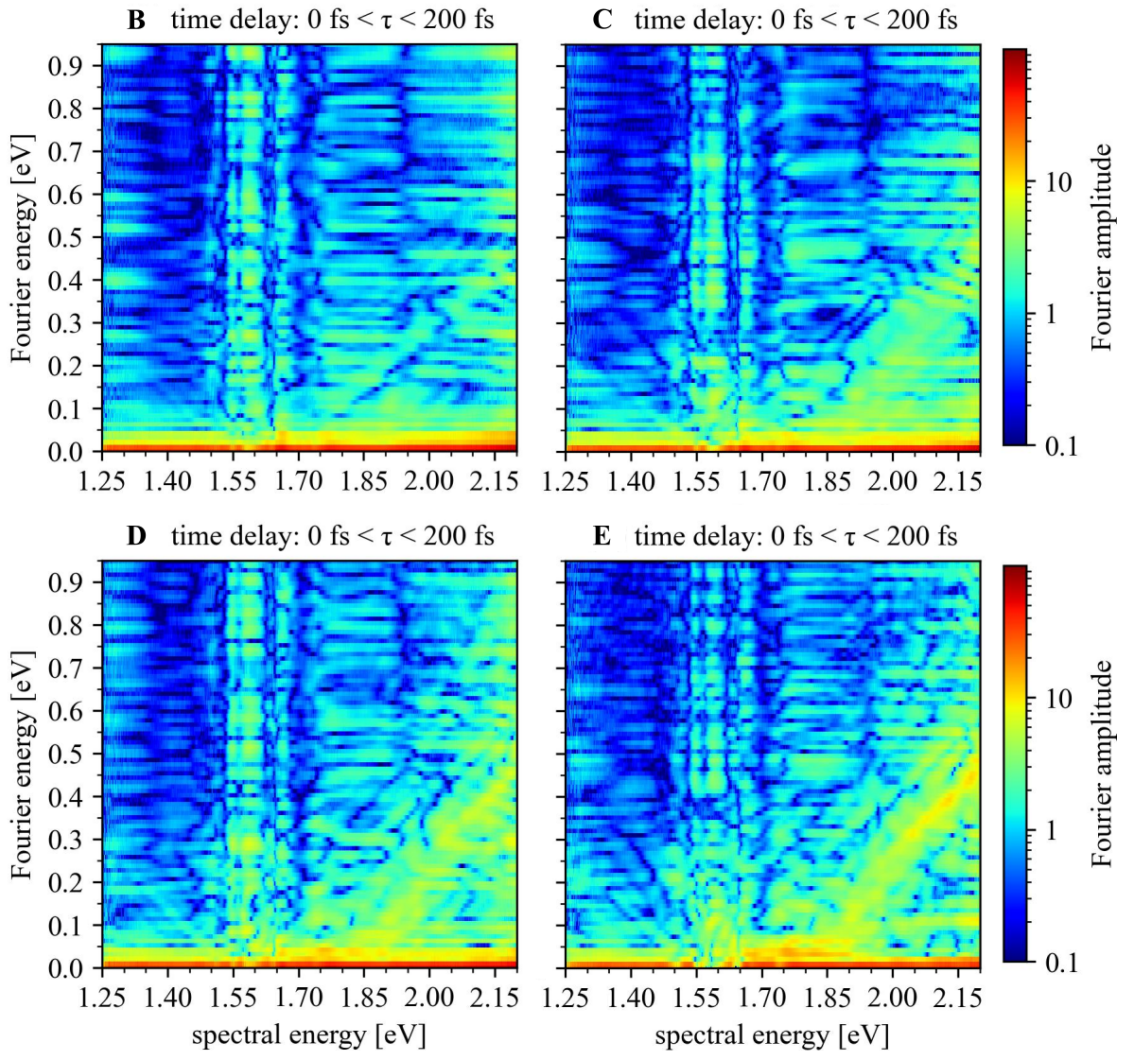

Figure 5.17.: Fourier amplitudes for control-pulse intensities **B** to **E** for the case of the pure solvent. While the overall signal increases with increasing control-pulse intensity, no minimum diagonal can be observed.

To track down possible reasons for the minimum diagonal, also the respective Fourier phases for positive time-delays only were calculated and summarized in Figure 5.18 for the data of the dissolved AlClPc molecules, and in Figure 5.19 for the comparative measurement in the pure solvent. Likewise, the procedure will be to first look at the data of the dissolved AlClPc molecules and afterwards compare it with the pure solvent to help identifying which effects arise from the molecule itself and which are also present in the pure solvent. Taking a look at Figure 5.18, it can be seen that the phase is mostly flat and phase changes are most significant along the diagonals. Especially for the minimum diagonal, which intersects the spectral energy range at

1.75 eV, the difference between the Fourier phase on the diagonal compared to the off-diagonal regions gets more pronounced as a function of the control-pulse intensity.

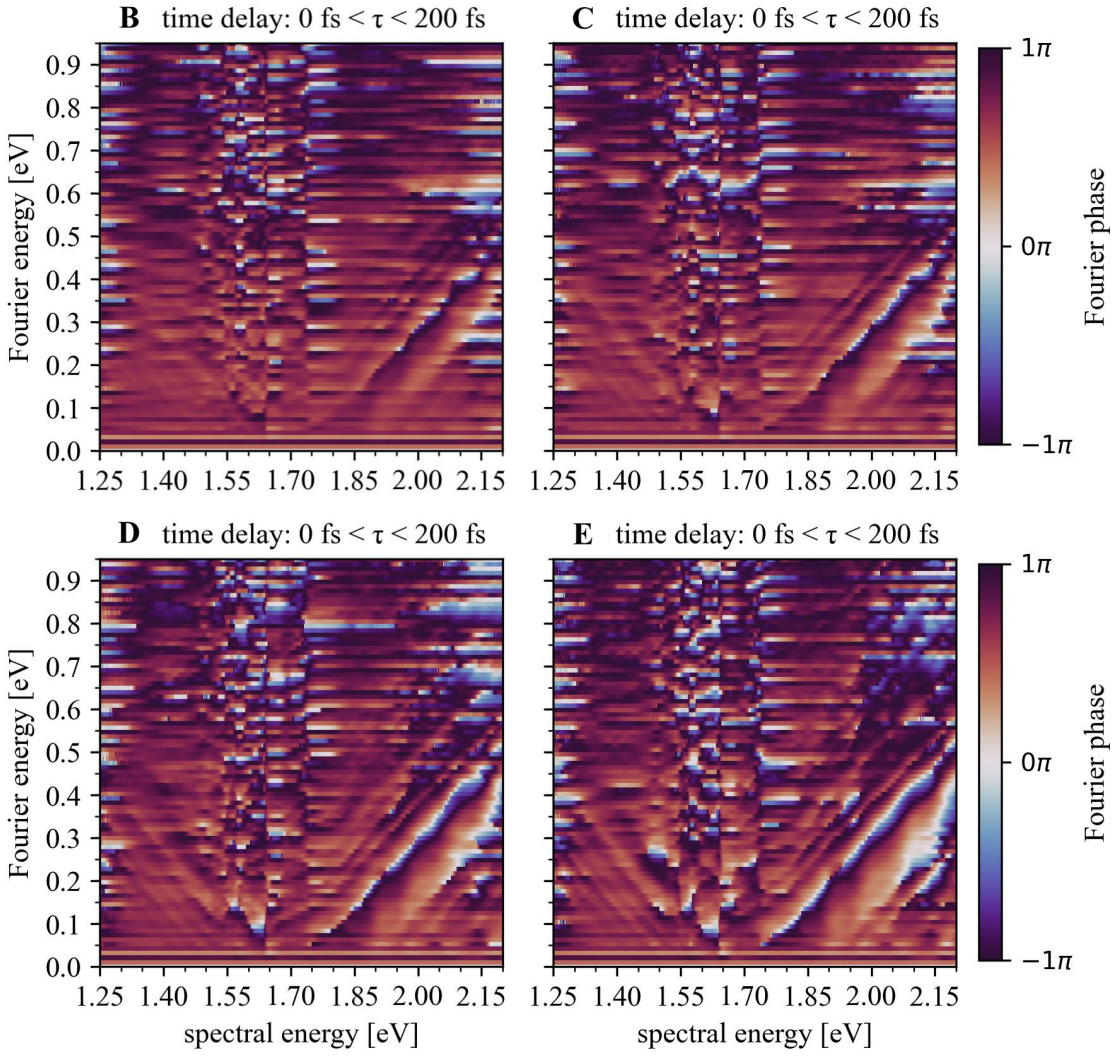

Figure 5.18.: Fourier phases for control-pulse intensities **B** to **E** for the case of the dissolved AlClPc. It can be seen, that the minimum diagonal with slope +1 intersects the spectral energy axis at 1.75 eV. In addition its Fourier phase is contrary to all other visible diagonals which have a non-zero, positive phase.

When looking at the Fourier phases of the comparative measurement in the pure solvent (Fig. 5.19), it can be said in general that the Fourier phases are more noisy (compared to the Fourier phases of AlClPc) due to the lower statistics, which makes the overall interpretation in the Fourier phase more difficult. Diagonals which can still be seen are the diagonal arising at a spectral energy of 1.70 eV with a positive, non-zero phase and directly below, a second diagonal with negative Fourier phase,

intersecting the spectral energy axis at an energy of 1.75 eV. This diagonal gets more pronounced with higher control-pulse intensities. In contrast to the Fourier phases of the dissolved AlClPc molecules, this diagonal is broader and has a more pronounced negative phase throughout all measured intensities.

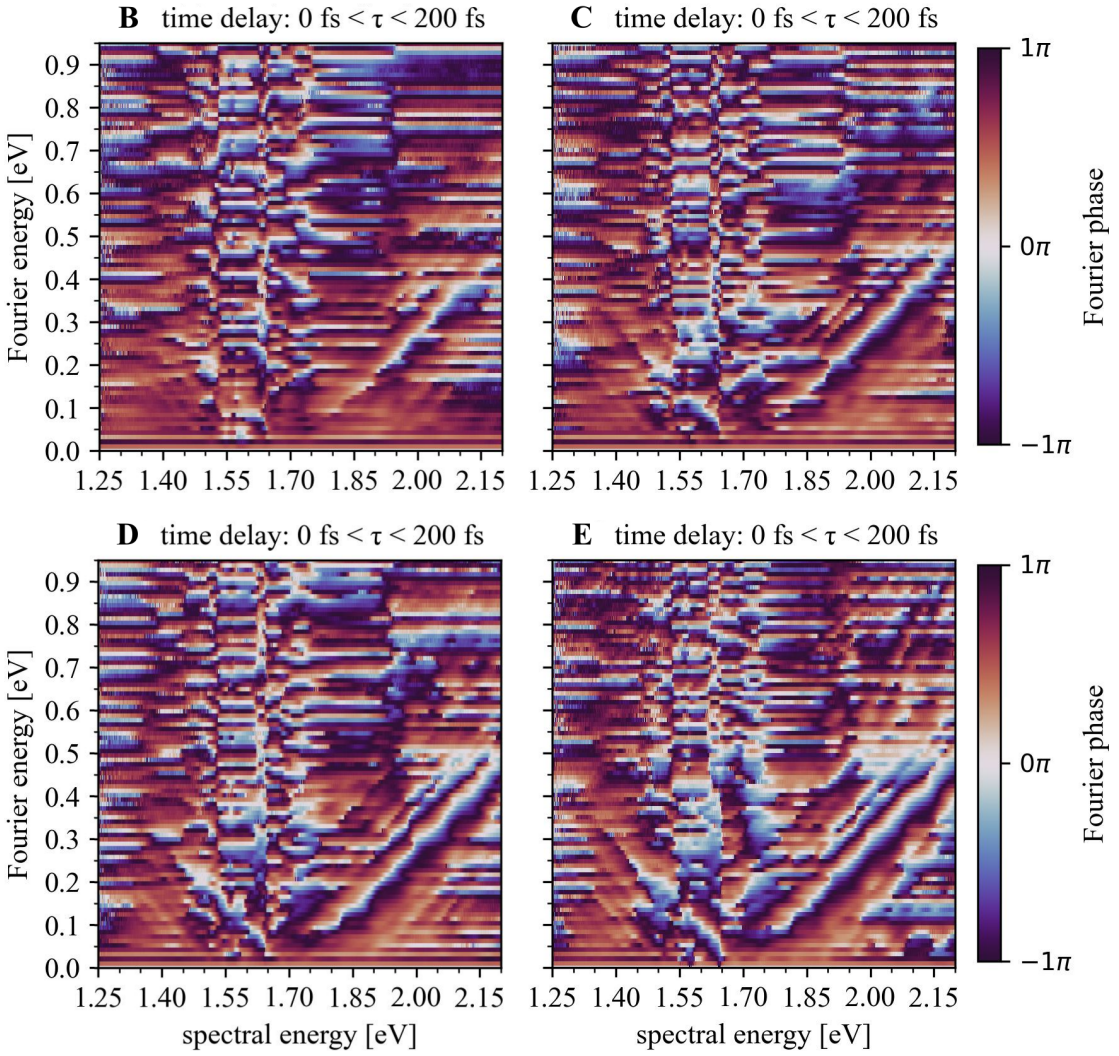

Figure 5.19.: Fourier phases for control-pulse intensities **B** to **E** for the case of the pure solvent. In contrast to the Fourier amplitude, the Fourier phases show a prominent diagonal structure. The diagonal with slope +1 intersecting the spectral energy axis at 1.70 eV has a positive, non-zero phase. Parallel to it a diagonal with negative phase, intersecting the spectral energy axis at 1.75 eV can be seen, which gets more pronounced with increasing control-pulse intensity.

To facilitate the comparison between the different control-pulse intensity cases, as well as between the data of the dissolved AlClPc and the pure solvent, lineouts of the 2D Fourier plots were taken (Figs. 5.20, 5.21, 5.22 and 5.23). The first set of lineouts

was determined by taking a lineout at a Fourier energy of 0.2 eV. Therefore, displaying the Fourier amplitude and corresponding phase as a function of the spectral energy (see Figure 5.20 for the AlClPc lineouts and Figure 5.21 for the comparative pure solvent measurement). While the lineouts along the spectral energy axis at a fixed Fourier energy do offer a higher resolution, the interpretation/readout of the Fourier amplitude is difficult due to the high amount of different diagonal contributions for spectral energies < 1.80 eV. The lineout along the Fourier axis for a fixed spectral energy solves this complexity problem by pre-selecting a spectral energy. The disadvantage lies here in the lower resolution along the Fourier axis. The second set of lineouts was taken at a spectral energy of 1.95 eV, leading to a representation of the Fourier amplitude and phase as a function of the Fourier energy (see Figure 5.22 for AlClPc and 5.23 for the comparative data taken with the pure solvent).

Looking at Figure 5.14 helps to find the most important features in the lineout plots: When taking the lineout at Fourier energy 0.2 eV, the contribution of the resonant diagonal (which arises at a spectral energy of 1.85 eV) starts at approximately 1.95 eV and ends at roughly 2.05 eV. The contribution of the diagonal arising at 1.70 eV cannot be seen clearly in the lineouts, since the contribution overlaps with the DC-component of the absorption line centered at 1.85 eV, as can be seen in the 2D-plot Fig. 5.14. The minimum diagonal can be seen in the lineouts in the spectral energy range between 1.90 eV and 1.95 eV. Contributions of the lineouts below 1.85 eV are neglected, as they are remnants of the DC-peaks form the artifact "absorption" lines (for spectral energies < 1.80 eV) due to the alternating referencing scheme (cf. Fig. 5.10 and Fig. 5.11).

For the second set of lineouts, which are taken for the spectral energy of 1.95 eV, it has to be noted that the Fourier energy components below 0.075 eV are neglected since they bear no other information than the DC-peak and small artifacts due to the Fourier transformation. According to Figure 5.14, contributions from the resonant diagonal are present in the Fourier-energy region between 0.1 eV and 0.2 eV, while the contributions from the minimum diagonal are expected in the region between 0.22 eV and 0.25 eV. Furthermore, the contribution of the diagonal arising at 1.70 eV are represented in the Fourier-energy region between 0.25 eV and 0.3 eV.

When looking at the Fourier phases, it is important to consider the Fourier amplitude at the same time, as the interpretation of a phase is meaningless when the amplitude vanishes. One needs to be especially careful as the Fourier phase can undergo instantaneous phase jumps, which are attributed to the missing amplitude. These

instantaneous jumps (accompanied with a Fourier amplitude of zero) are artifacts and no real phase transitions. To guide the reader's eye, irrelevant regions in both sets of lineouts are grayed out in Figures 5.20-5.23. With this knowledge one can now take a look at Figure 5.20, which shows the spectral lineouts (of the AlClPc dataset) for a Fourier energy of 0.2 eV of both Fourier amplitude and phase.

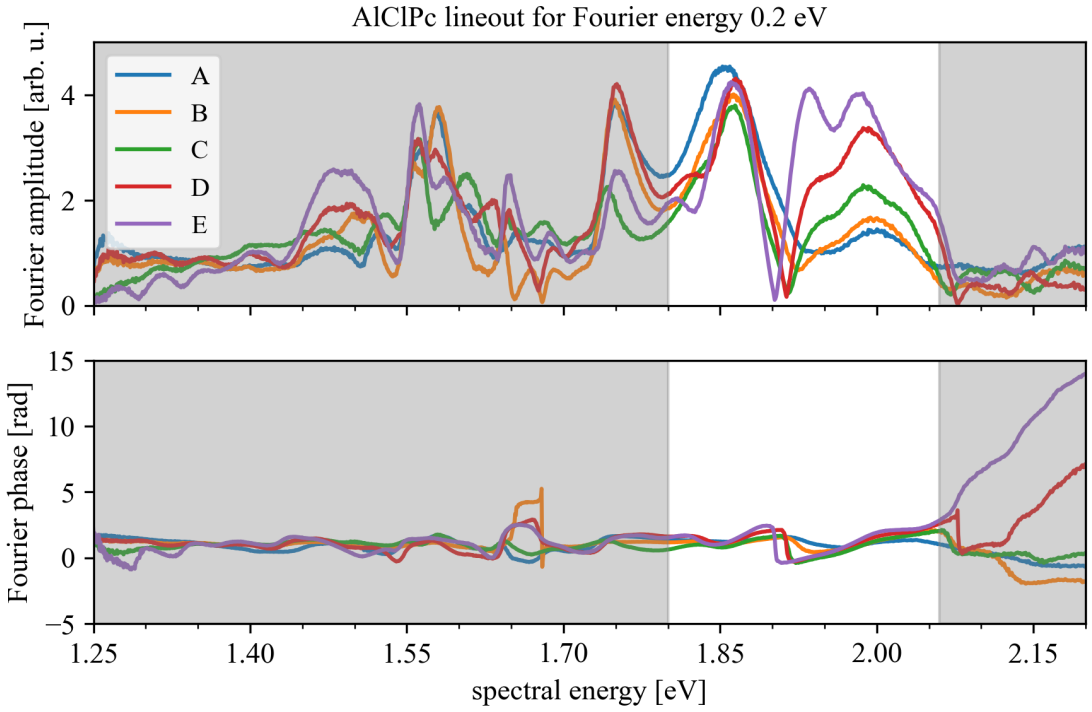

Figure 5.20.: Lineouts of the Fourier amplitudes and phases (of the dissolved AlClPc molecules) depicted in Figure 5.16 and 5.18 respectively, at a Fourier energy of 0.2 eV. Displayed are in the upper panel the lineouts of the Fourier amplitude as a function of the spectral energy for the five different control-pulse intensity settings **A**-**E** and in the lower panel the corresponding Fourier phases.

Looking at the spectral energy region between 1.95 eV and 2.05 eV, an increase in the Fourier amplitude can be seen for increasing control-pulse intensity. This is attributed to the laser-driven dipoles of the AlClPc molecules. At the same time, the minimum at energy range between 1.90 eV and 1.95 eV deepens/sharpens with higher control-pulse intensities. While for intensity case **A**, almost no minimum is visible, it starts to appear fo intensity **B** at approximately 1.92 eV. Further increasing the control-pulse intensity, the minimum gets sharper and shifts to lower energies (1.90 eV for intensity **E**). Taking a look at the corresponding Fourier phases, it can be seen that a phase shift occurs simultaneously to the minimum buildup in the Fourier amplitude. Furthermore, the amount of phase shift coincides with the depth of the minimum. It

can also be seen, that the energy position of the phase shift is identical to the energy position of the minimum in the Fourier amplitude. This further underlines, that the observed minimum in the Fourier amplitude is linked to the phase shift.

Taking a look at the respective lineouts of the pure solvent (depicted in Fig. 5.21), no systematic increase in the Fourier amplitude for increasing control-pulse intensity can be observed. Furthermore, no systematic minimum in the Fourier amplitude sustaining for all control-pulse intensities can be found in the lineouts. This means that the effects observed in Figure 5.20 need the presence of the molecule's resonance to appear.

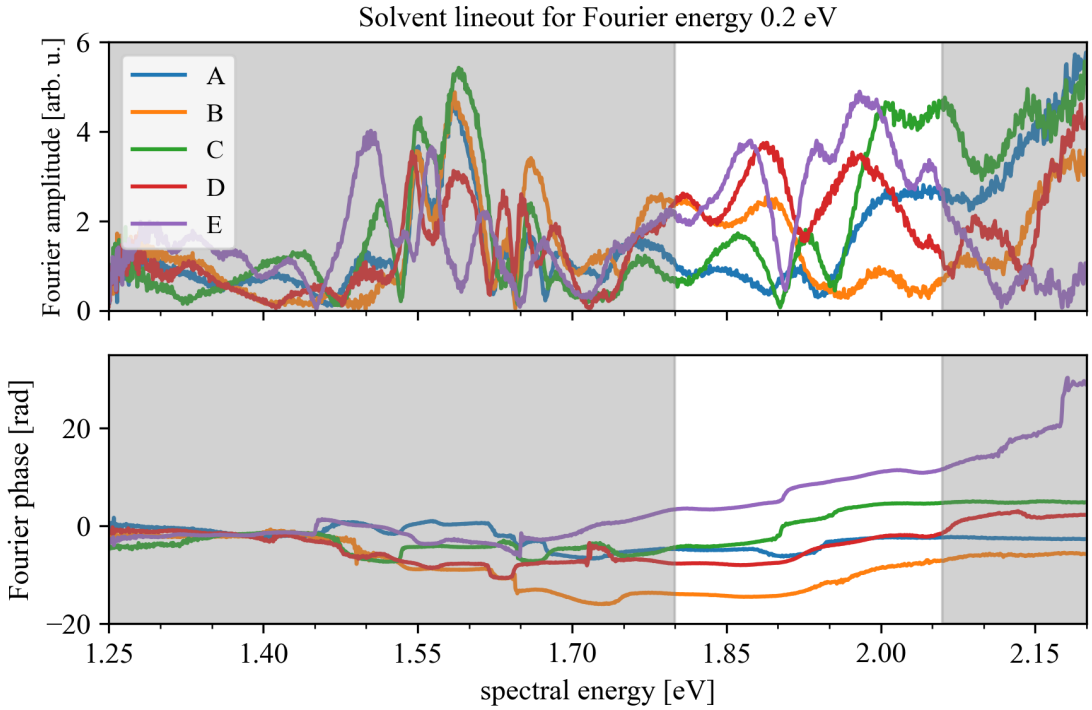

Figure 5.21.: Lineouts of the Fourier amplitudes and phases (of the pure solvent) depicted in Figure 5.17 and 5.19 respectively, at a Fourier energy of 0.2 eV. Depicted are the lineouts of the Fourier amplitude as a function of the spectral energy for the five different control-pulse intensity settings **A**-**E** (upper panel) and in the corresponding Fourier phases (lower panel).

In the next step, the lineouts along the Fourier energy axis for a fixed spectral energy of 1.95 eV are investigated. Again the lineouts of the AlClPc data (cf. Fig. 5.22) are analyzed first, followed by the comparison with the solvent lineouts (Fig. 5.23). Taking a look at the AlClPc lineouts in Fig. 5.22, an increase in amplitude can be observed in the Fourier-energy region between 0.1 eV and 0.2 eV, and between 0.25 eV and 0.3 eV, for increasing control-pulse intensities. Both areas belong to

contributions from the diagonals with slope +1 arising at a spectral energy of 1.85 eV and 1.70 eV, respectively. When comparing both increases in amplitude, it can be seen that the resonant contribution from the molecule is more sensitive to the control-pulse intensity as the other diagonal which also appears in the pure solvent scan. In between both Fourier amplitude contributions, the minimum can be seen. In this representation, it seems to shift to higher Fourier energies when increasing the control-pulse intensity. Taking a look at the respective Fourier phases (bottom panel of Fig. 5.22), a phase jump can be observed when the minimum in the Fourier amplitude starts to appear.

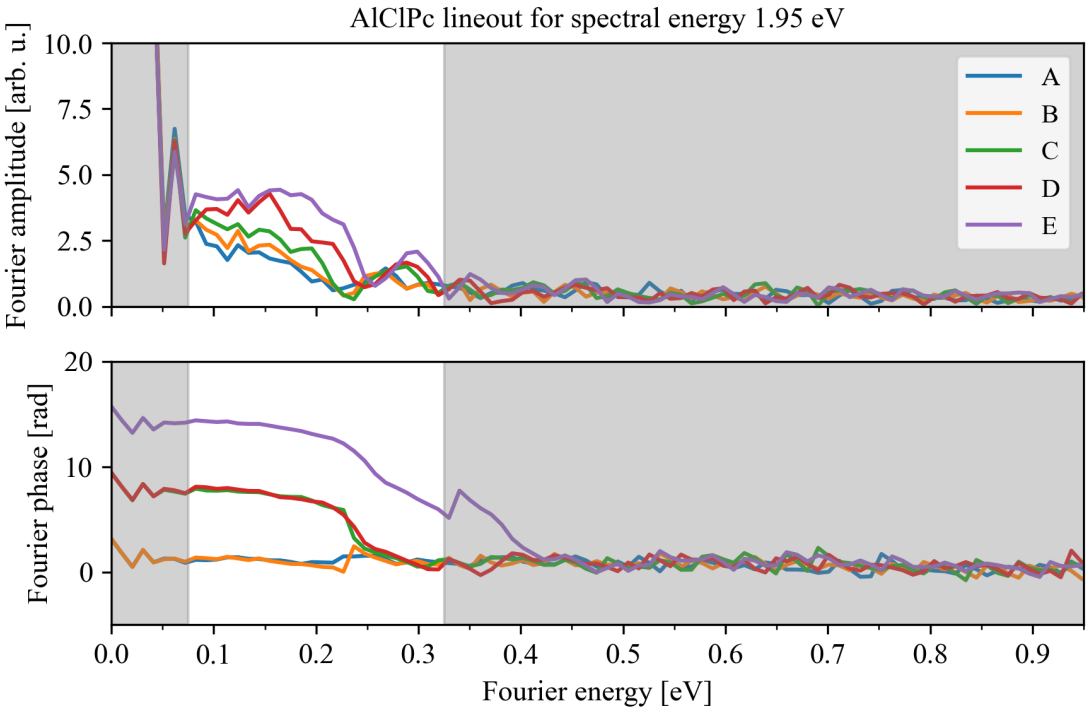

Figure 5.22.: Lineouts of the Fourier amplitudes and phases, of the dissolved AlClPc molecules depicted in Figure 5.16 and 5.18 respectively, at a spectral energy of 1.95 eV. The upper panel shows the lineouts of the Fourier amplitude as a function of the Fourier energy for the five different control-pulse intensity settings **A**-**E**. The lower panel shows the corresponding course of the Fourier phases.

The in Figure 5.23 depicted lineouts of the pure solvent data show an overall increase for the Fourier amplitude with increasing control-pulse intensity. The phase change at a Fourier energy of 0.2 eV, which is only present for the two lowest intensities **A** and **B**, can be identified as an artifact due to the vanishing Fourier amplitude. Furthermore, the Fourier phases of the pure solvent do not show any significant phase

changes.

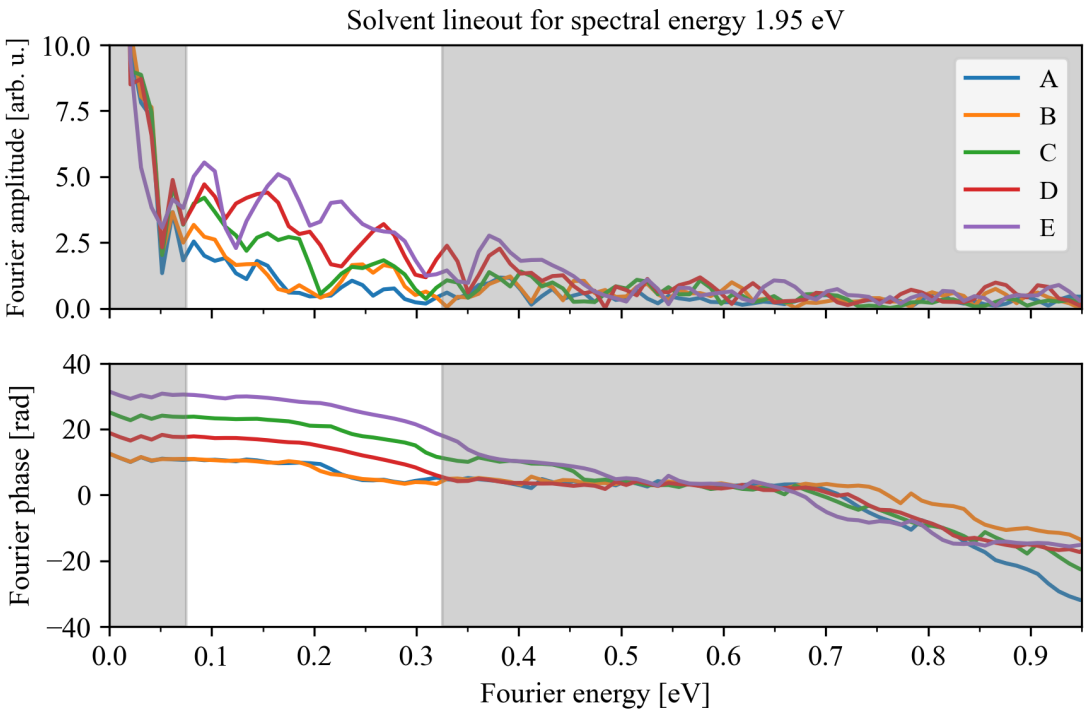

Figure 5.23.: Lineouts of the Fourier amplitudes and phases, of the pure solvent depicted in Figure 5.17 and 5.19 respectively, at a spectral energy of 1.95 eV. The lineouts of the Fourier amplitude as a function of the Fourier energy for the five different control-pulse intensity settings **A**-**E** are shown in the upper panel. The corresponding course of the Fourier phases are depicted in the lower panel.

In summary, it can be said that the diagonal starting from the AlClPc resonance at 1.85 eV only appears in the AlClPc data. On the contrary, the diagonal in the Fourier plots with slope +1 arising at a spectral energy of 1.70 eV is present in both the AlClPc data, as well as in the pure solvent data, even though both targets do not have resonance lines in this specific energy region. The minimum diagonal which lies between both mentioned diagonals only appears in the AlClPc data. Furthermore, it could be shown in the lineouts that the minimum diagonal is accompanied by a simultaneous phase shift.

After this extensive analysis and extraction of solely molecular features, it is time to interpret and discuss the results. For this purpose, an atom-like toy model simulation is used in chapters 6.2 and 6.3, which helps to identify and extract the underlying physical processes.

6. Manipulation of the real-time dipole response

As presented in the previous chapter, the measurement concept is not only sensitive to the resonantly induced real-time dipole response of the target, but also to non-resonant pulse induced effects in the solvent.

Therefore, this chapter focuses on the numerical simulation of the observed effects using an atom-like toy model. The chapter is separated into three main sections. Section 6.1 focuses on the effects observed with measurement method 1, which comprises solely the manipulation of the time-dependent dipole response of AlClPc, while sections 6.2 and 6.3 treat the effects observed with measurement method 2. Section 6.2 treats the non-resonant case, where the interaction of the electric field with the non-resonantly absorbing solvent gives insight into the pulse's temporal structure. Finally, section 6.3 outlines how the sum of both resonant and non-resonant time-dependent dipole responses give rise to new destructively interfering features in the Fourier amplitude which can be assigned to the different induced dipole phases.

6.1. Resonant case - Modeling the manipulation of the time-dependent dipole response of AlClPc

To model the laser-induced coherent control of the time-dependent dipole moment in AlClPc, a numerical toy model is used, where the time-dependent Schrödinger equation is solved for a multi-level system. For this, the Q-band is approximated by an ensemble of $N = 300$ closely spaced states with energy widths of 2.2 meV, each. The linewidth of the states was chosen sufficiently small to reproduce quantum interferences with the time-delay range observed in the measured data. The weak-field only white-light absorption spectrum of the Q-band was approximated by equidistantly distributing the 300 states over an energy range between 1.61 eV and 2.21 eV with a mutual overlap and adjusting their real-valued transition dipole moments to the

ground state such that the simulated white-light absorption spectrum agrees with the measured one. As a comparison, both, measured and simulated weak-field white-light absorption spectra are depicted in Figure 6.1(A).

In this toy model, the time-dependent Schrödinger equation

$$i\hbar\frac{\partial}{\partial t}\left|\psi(t)\right\rangle = \mathcal{H}\left|\psi(t)\right\rangle, \tag{6.1}$$

with $\mathcal{H} = \mathcal{H}_0 + \mathcal{H}_{int}$ is solved using the split-step algorithm [57] previously introduced in section 2.3.

By using the dipole approximation for the interaction Hamiltonian ($\mathcal{H}_{int} = \hat{d}\cdot E(t)$), and representing the wavefunction $|\psi(t)\rangle$ as a sum of time-dependent state coefficients $c_i(t)$ and the spatial eigenstates $|\Phi_i\rangle$ of the system ($|\psi(t)\rangle = \sum_i c_i(t)\,|\Phi_i\rangle$), the dipole response $d(t)$ can be calculated by

$$d(t) = \langle\psi(t)|\,\hat{d}\,|\psi(t)\rangle = \sum_{m,n} d_{nm}c_n(t)c_m^*(t) + c.c., \tag{6.2}$$

with $d_{nm} = \langle\Phi_m|\,\hat{d}\,|\Phi_n\rangle$.

The transition dipole matrix elements d_{nm} between the ground state and the 300 excited states representing the Q-absorption band were chosen with the aim to reproduce the measured weak-field white-light absorption spectrum. The simulation-generated absorption spectrum closely matches the experimental data, as can be seen in Figure 6.1(A).

The resulting Hamiltonian matrix reads

$$\mathcal{H} = \begin{bmatrix} \omega_0 & d_{1,0}E(t) & d_{2,0}E(t) & \dots & d_{300,0}E(t) \\ d_{0,1}E(t) & \omega_1 & 0 & \dots & 0 \\ d_{0,2}E(t) & 0 & \omega_2 & \dots & 0 \\ \vdots & \vdots & \vdots & \ddots & 0 \\ d_{0,300}E(t) & 0 & 0 & 0 & \omega_{300} \end{bmatrix}, \tag{6.3}$$

where $E(t) = E_{\text{excitation}}(t) + E_{\text{control}}(t-\tau)$ is the sum of both - excitation and control pulse - electric fields. ω_i represent the complex eigenenergies of the states. Within the simulation the arrival time of the excitation pulse is kept constant at $t = 0$, while the control pulse is temporally varied with the relative time delay τ. Both pulses are implemented with a Gaussian envelope, an intensity FWHM of 3 fs and a central photon energy of 1.70 eV.

The dipole spectrum $\tilde{d}(\omega)$ is, in turn, obtained by Fourier-transforming the dipole response $d(t)$. Together with the spectral representation of the electric field $\tilde{E}_s(\omega)$, the absorption cross section $\sigma(\omega)$ can be calculated as

$$\sigma(\omega) \propto \omega \cdot \mathrm{Im}\left[\frac{\tilde{d}(\omega)}{\tilde{E}_s(\omega)}\right]. \tag{6.4}$$

This reflects the interference of the excitation-pulse induced dipole response with the excitation pulse itself. The optical density (OD) is, in-turn, proportional to the absorption cross section via

$$\mathrm{OD}(\omega) = -\log_{10}\left(\frac{I(\omega)}{I_0(\omega)}\right) = \frac{N_a l \sigma(\omega)}{\ln(10)}, \tag{6.5}$$

with the number density of absorbers N_a (i.e. AlClPc molecules) and the length of the absorption volume l. For a more detailed derivation of equation (6.4) and (6.5) the reader is referred to [24].

To mimic the non-collinearity of the experimental setup, an additional wave-front averaging (see also references [91, 92] for more details) is performed. Therefore, the absorption spectra with different carrier-envelope-phase (CEP) values for the control pulse are calculated, while the CEP of the excitation pulse is kept fixed. Afterwards, the average of the resulting absorption spectra is taken. By using this procedure, the optical interference between both optical pulses is suppressed in the simulation. In the experiment, the optical interference is suppressed by a pulse-intersection angle of 1.72°. In a last step, the simulated time-delay trace is convoluted with the instrument response function, to account for the finite temporal resolution of the experiment. The resulting time-delay trace, as well as the corresponding Fourier plot for positive time delays only are displayed in Figure 6.1(B) and (C).

To analyze the impact of the control-pulse intensity on the manipulation of the excitation-pulse induced dipole response, the numerical toy model was conducted for two more intensities, half (see first row of Figure 6.2) and double (second row of Figure 6.2) of the case shown in Fig. 6.1. The results presented in Figure 6.1 reproduce the experimental results best.

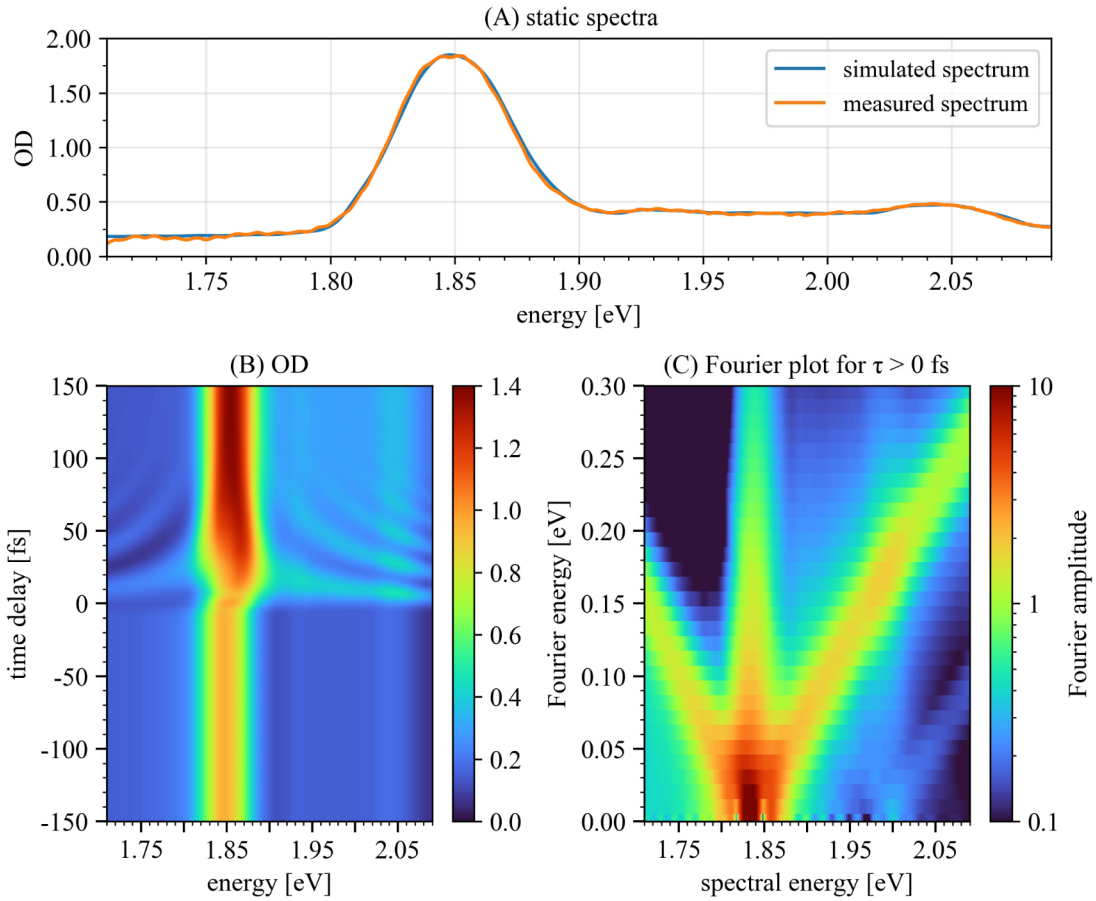

Figure 6.1.: Simulated and measured static absorption spectra (A), time-delay dependent optical density (B) and Fourier energy plot for positive time delays only (C). The subplot (B) shows the modeled optical density over a time-delay range of 300 fs, where the colorbar marks the magnitude of OD. The Fourier plot depicted in panel (C) shows diagonals with slope +/-1 in a similar fashion as seen in the experimental data. Negative time delays refer to control-pulse first, positive to excitation-pulse first. Image adapted from [88].

The results of the control-pulse intensity scan are the following: When the intensity of the control pulse is lowered, the magnitude of the spectro-temporal structures upon the absorption spectrum for positive time delays decrease (see Figure 6.2(A)). In turn, when the control-pulse intensity is increased one is able to enter the strong coupling limit, which is indicated here by a Rabi-/Autler-Townes splitting of the Q_I-band for positive time-delays (see Figure 6.2). A slight band splitting can already be seen in Figure 6.1(B). This involves light-induced level shifts of strongly coupled states, which can be observed to set in and grow with increasing control-pulse intensity.

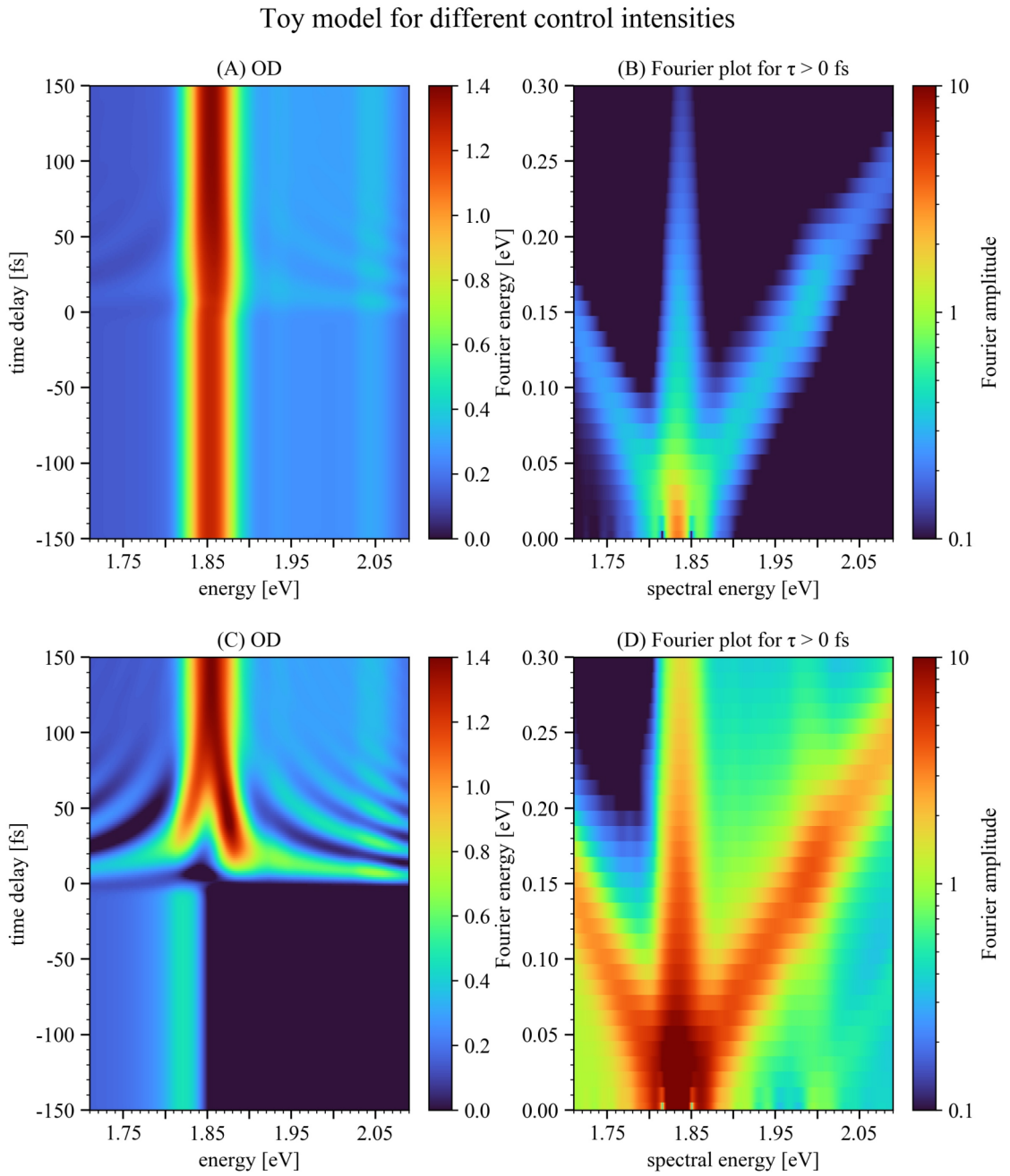

Figure 6.2.: Overview of the impact of the control-pulse intensity on the time-dependent optical density and the corresponding Fourier energy plot for positive time delays only ($\tau > 0$ fs). The first row depicts the case of half the control-pulse intensity, while the second row depicts the case of double the control-pulse intensity as compared to Figure 6.1. Panels (A) and (C) show the modeled optical density over a time-delay range of 300 fs. The Fourier plots (B) and (D) reveal diagonals with slope +/-1 in a less (upper row) or more (lower row) pronounced fashion compared to the experimental data. Image adapted from [88].

In this toy model, only states up to a total excitation energy of 2.21 eV were considered, therefore, only representing the Q-band and neglecting the Soret-band in the UV-regime. Excitation of these energetically higher-lying states might also take place in the experiment but were neglected in the simulation due to their lower relative population. It is assumed in the considerations of the toy model that they have only a minor effect on the strong coupling of the energetically lower-lying states of the Q-band.

Comparing the measured time-delay-dependent optical density (Fig. 5.8(A)) and the simulated trace (Fig. 6.1(B)) a good qualitative agreement can be found. Not only, does the toy model reproduce the decrease in the overall absorption for negative time delays, but also the observed hyperbolic structures upon the absorbance converging towards the Q_I-band. In addition, the slight splitting of the Q_I-band in the time delay range between 0 fs and 50 fs can be reproduced by the toy model. Furthermore, a good qualitative agreement between experiment and model is found in the Fourier energy plot for positive time-delays only depicted in Figure 6.1(C), where diagonals of slope +/-1 linked to the Q_I-bands spectral energy appear in the same fashion as in the experimental data (see Fig. 5.9(A)). The spectro-temporal modulations upon the absorption spectrum of AlClPc, as well as the diagonals in the corresponding Fourier-energy plot for positive time-delays only can therefore be realized and understood with the presented atom-like multi-level toy model. The good structural agreement between the experimental observations and the simulation results shows that the dynamical mechanism at work in the laser-driven target can be approximated as a coupled system of ground and excited states. The experimentally observed spectro-temporal structures in the optical density can thus be understood as a laser-induced coupling mechanism between the ground state and an ensemble of excited states which also includes strong-coupling effects represented by the Autler-Townes splitting.

6.2. Non-resonant case - How the solvent gives insight into the pulses' temporal structure

To model the spectro-temporal effects observed in the pure solvent, a simplification to the aforementioned toy model is made. Therefore, it is reduced to a two-level system, consisting of a ground state at an energy of 0 eV and one excited state centered at an energy of 4.7 eV with a linewidth of 0.053 eV, representing an excited electronic state of ethanol. Both, excitation and control pulse are implemented as FTL Gaussian

envelope pulses with an intensity FWHM of 5 fs and a center photon energy of 1.85 eV. As in the previous section, the absorption spectra are calculated with different carrier-envelope-phase (CEP) values for the control pulse, while keeping the CEP constant for the excitation pulse to suppress optical interference between both pulses in the simulation. Using this consideration, the OD(ω) was calculated for a time delay range from -300 fs to 300 fs with an incremental time-delay step size of 2.65 fs. The thereby simulated time-delay-dependent optical density OD(ω) is depicted in the left panel of Figure 6.3. Furthermore, the differential optical density ΔOD(ω) is shown (center panel), which was calculated by subtracting the weak-field only absorption spectrum from the time-delay-dependent optical density OD(ω). The Fourier energy plot, obtained by Fourier transforming the ΔOD(ω) along the time-delay axis is depicted in the right panel of Fig. 6.3.

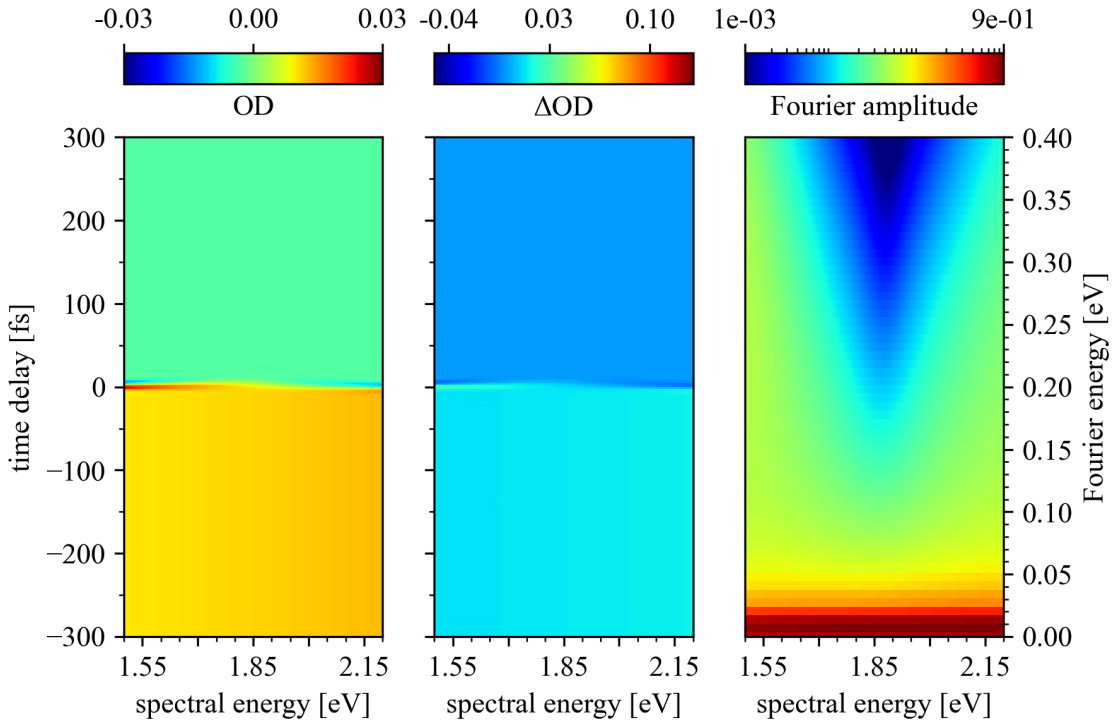

Figure 6.3.: Simulated time-delay-dependent optical density (left), ΔOD (middle) and corresponding Fourier energy plot (right) under the assumption of 5 fs (FWHM) FTL pulses and an off-resonant excited state of ethanol. In the OD and ΔOD an overall step can be observed between positive and negative time delays due to the different intensities of excitation and control pulse. In the pulse-overlap region a slight modulation in both, OD and ΔOD can be observed. This gives rise to the broad v-shape like contribution in the Fourier amplitude.

Taking a look at the OD and ΔOD depicted in Fig. 6.3 the most pronounced effect lies in the overall step in OD for positive and negative time delays, which arises

due to the different intensities of control and excitation pulse. In addition, a slight modulation can be observed in the pulse overlap region for time delays +/- 5 fs. This "short-lived" modulation gives rise to a broad v-shape like contribution in the Fourier amplitude centered at the pulses' photon energy of 1.85 eV. The pronounced DC-peak in the Fourier amplitude results from the overall step in OD between positive and negative time-delays. Comparing the simulated optical density from Fig. 6.3 with the experimental data shown in Fig. 5.10 and Fig. 5.11 it can be seen that the spectro-temporal modulations on the OD which can be observed in a time-delay region of approximately +/- 100 fs could not be reproduced yet. Also the experimentally determined sharp diagonals with a slope of +/- 1 in the Fourier amplitude plots (Fig. 5.17) are not reproduced in the results from Fig. 6.3. This concludes that the pure presence of the solvent is not the solely reason for the experimentally observed spectro-temporal modulations in the solvent's absorbance.

In a next step, the excitation pulse is modified from a Fourier-transform limited (FTL) pulse, to a pulse consisting of a short 5 fs main pulse and a long temporal pedestal of 100 fs, which can be seen as a simplified picture of an ultrashort pulse with remaining extended uncompressed pre- and post-pulses. The intensity ratio between main excitation pulse and the pedestal was set to 2.5:1. The control pulse is kept as a FTL-pulse with a FWHM of 5 fs. Both, excitation and control pulse are centered at a photon energy of 1.85 eV, such that a direct coupling with one photon to the excited state at 4.7 eV is very low. Nonetheless, the transition to the excited state can be conducted provided the control-pulse intensity is high enough. The transition matrix element between the ground and excited state was chosen such that for a control-pulse intensity of I_{set}, a change in the solvent's dipole phase by $\pi/2$ is obtained. The real-time dipole response of the 2-level system for a specific time delay of $\tau = 20$ fs is depicted in Figure 6.4.

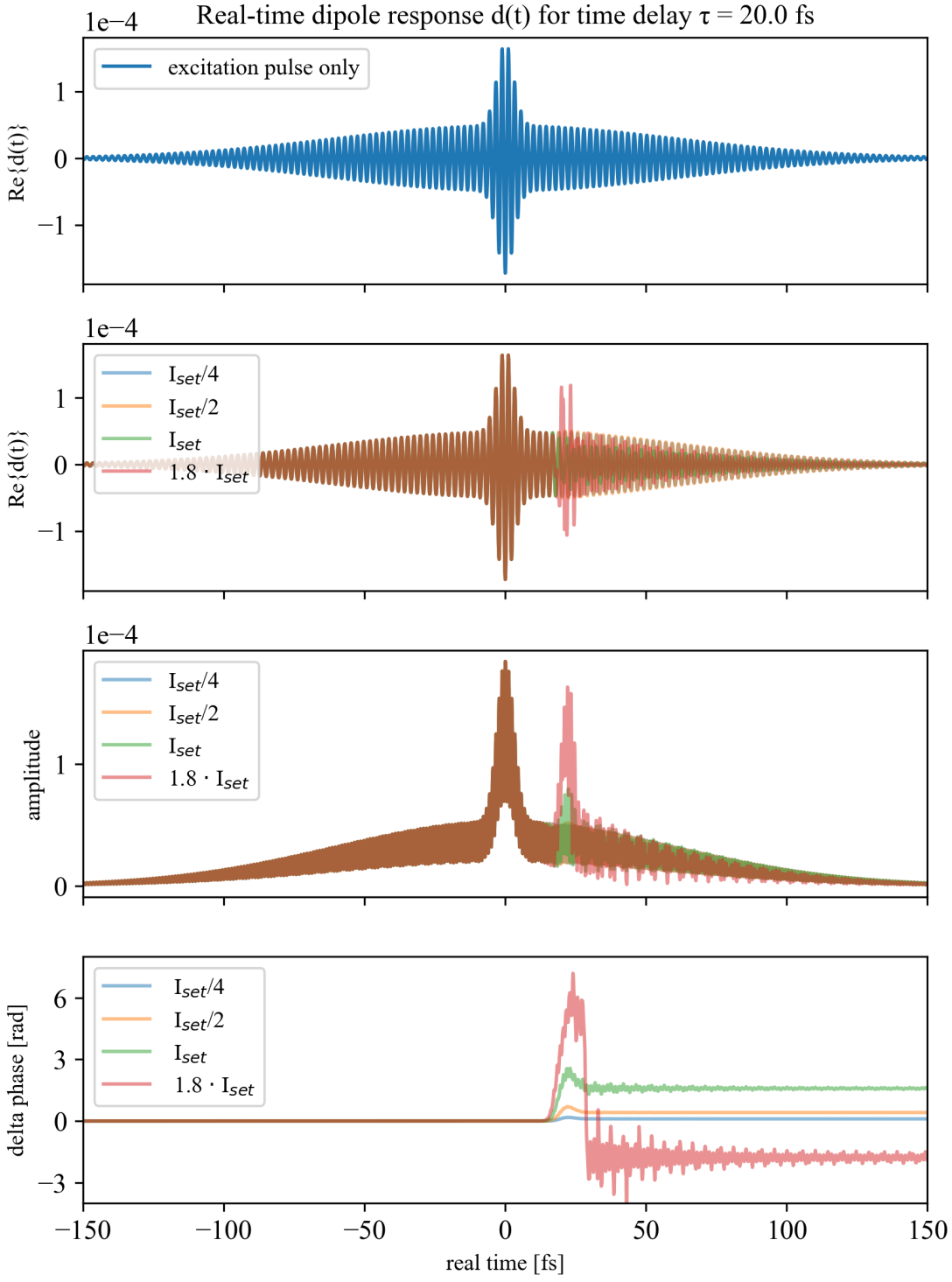

Figure 6.4.: Simulated real-time dipole response for the 2-level model of the solvent with an excitation pulse consisting of a sharp main pulse with a FWHM of 5 fs and a pedestal with a FWHM of 100 fs. The first panel shows the real part of the excitation-pulse induced unperturbed real-time dipole response $\mathrm{Re}\{d(t)\}$. The second panel shows $\mathrm{Re}\{d(t)\}$ with a control pulse present at a time delay of 20 fs (for different control-pulse intensities ranging from $\mathrm{I}_{set}/4$ to $1.8 \cdot \mathrm{I}_{set}$). The impact of the respective control pulse can be seen in the induced amplitude and phase changes (panel 3 and 4, respectively). With increasing control-pulse intensity, the amount of induced phase change increases.

The first panel shows the excitation-field induced real-time dipole response without interaction with the intense control pulse. It can be nicely seen, that the dipole response follows the trend of the excitation pulse. In the second panel, the real part of the perturbed dipole response is shown after the interaction with the control pulse for a time delay of 20 fs. Depicted are the cases for four different control-pulse intensities ranging from $I_{set}/4$ to $1.8 \cdot I_{set}$. The third panel shows the amplitude of $\mathrm{Re}\{|d(t)|\}$, and the bottom panel shows the control-pulse induced phase change of the dipole response. Since no rotating-wave approximation is implemented in the simulation, both amplitude and delta phase show a fast oscillating behavior. Taking a look at Figure 6.4, it can be seen that through the introduction of the pedestal in the excitation pulse, the control pulse is able to coherently modify the excitation pulse for the duration of the pedestal. This effect is also known as cross-phase modulation (XPM). The control-pulse induced phase change increases with higher control-pulse intensities in a similar fashion as for the simple resonant 2-level system shown in Figure 6.8.

As already mentioned, the transition matrix element was chosen such that a phase change of $\pi/2$ is obtained with a control pulse intensity of I_{set}. Furthermore, it can be seen that for low control-pulse intensities the phase remains almost unchanged. This fits to the experimental observation that for low control-pulse intensities nearly no effect can be seen in the pure solvent. For the control-pulse intensity $1.8 \cdot I_{set}$, both amplitude and phase show a different behavior due to the additional population transfer to the excited state at 4.7 eV, which is not possible for lower control-pulse intensities.

The absorption spectra were, again, calculated with different carrier-envelope-phase (CEP) values for the control pulse, while keeping the CEP constant for the excitation pulse to suppress optical interference between both pulses in the simulation. With this consideration, the $\mathrm{OD}(\omega)$ was calculated for a time delay range from -300 fs to 300 fs with an incremental time-delay step size of 2.65 fs for the control pulse intensities $I_{set}/4$, $I_{set}/2$, I_{set} and $1.8 \cdot I_{set}$.

The simulated time-delay-dependent optical density $\mathrm{OD}(\omega)$ with a control-pulse intensity of I_{set} can be seen in the left panel of Figure 6.5. In addition, the differential optical density $\Delta\mathrm{OD}(\omega)$ is shown (center panel), which was calculated by subtracting the weak-field only absorption spectrum from the time-delay-dependent optical density $\mathrm{OD}(\omega)$. The Fourier energy plot, in turn, is obtained by Fourier transforming the $\Delta\mathrm{OD}(\omega)$ along the time-delay axis (right panel of Figure 6.5). It can be seen, that

even though no resonance is present in the spectral region of the excitation pulse, spectro-temporal modulations centered at the pulse's center frequency are generated for both positive and negative time delays. Additionally, diagonals with a slope of +/- 1, arising at the excitation-pulse center frequency of 1.85 eV are observed in the Fourier energy plot. The pronounced DC-peak in the Fourier amplitude results from the overall step in OD between positive and negative time-delays.

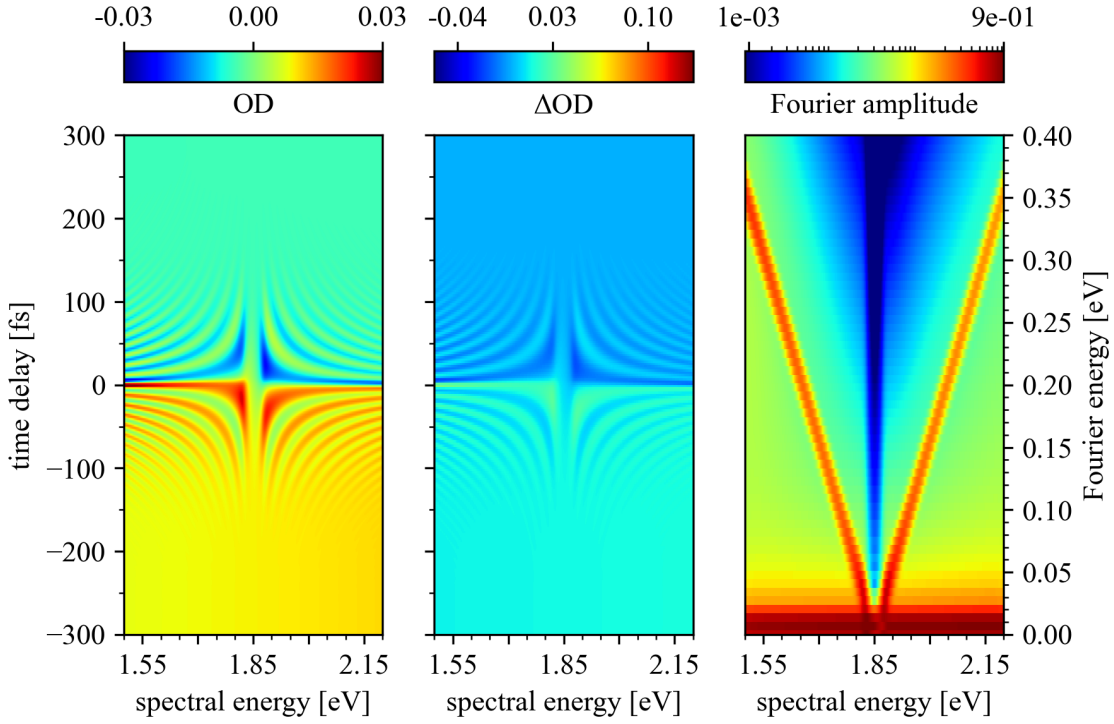

Figure 6.5.: Simulated time-delay-dependent optical density (left), ΔOD (middle) and corresponding Fourier energy plot (right) for control-pulse intensity I_{set}. Even though the resonance lies outside the pulse's spectral region, spectro-temporal modulations centered at pulse's center frequency can be observed for positive and negative time delays due to cross-phase modulation. By Fourier-transforming the optical density along the time-delay axis, these hyperbolic structures result in diagonals with a slope of +/-1 arising at the excitation pulse's center frequency of 1.85 eV.

Figure 6.6 shows the calculated Fourier amplitude (left panel) and phase (right panel) for only positive time delays ($\tau > 0$) of the in Figure 6.5 depicted ΔOD. The DC-peak, which could be observed in the right panel of Figure 6.5 vanishes when considering positive time delays only. A slight asymmetry can be observed in both Fourier amplitude and phase plots, which might be associated with the off-resonant state being present at 4.7 eV. Furthermore, it can be seen that the most pronounced changes in the Fourier phases coincide with the diagonal slopes in the Fourier amplitude. A similar behavior can be observed in the experimentally

determined Fourier phases of the pure-solvent data (see Fig. 5.19).

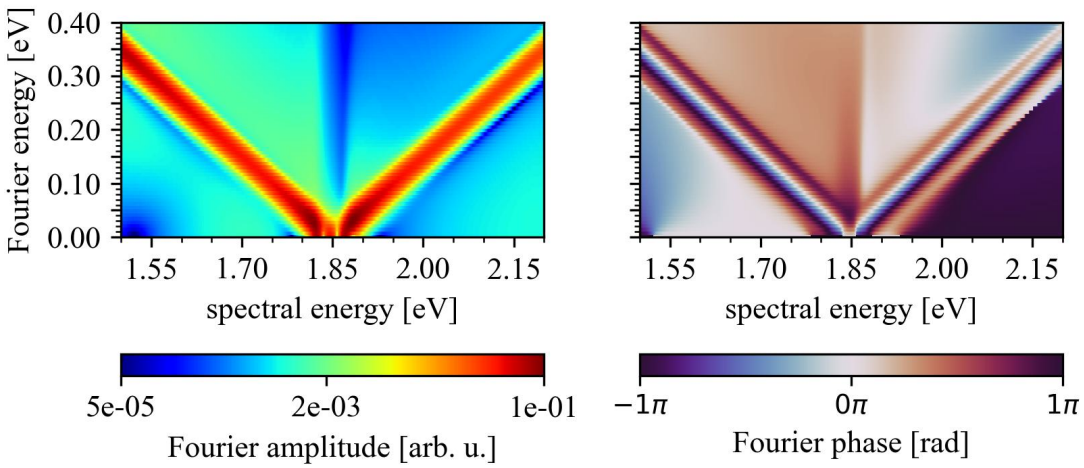

Figure 6.6.: Fourier amplitude and phase (left/right panel) for positive time-delays only ($\tau > 0$) of the in Figure 6.5 depicted ΔOD. Diagonals with a slope of +/-1 arising from the excitation-pulse's center energy can be observed. The slight asymmetry between energies smaller/bigger than 1.85 eV might be caused due to the presence of the excited off-resonant state at 4.7 eV.

Comparing Fig. 6.5 with the experimentally measured OD(ω) of the pure solvent (Fig. 5.10 and Fig. 5.11) a good qualitative agreement can be found for positive time delays. In addition, the toy model reveals diagonals with slope of +/-1 in a similar fashion as observed in the experimental data (see Fig. 5.17). This is a clear indication that the diagonals observed in the measurement data of the pure solvent are a result of cross-phase modulation and can, therefore, be associated to the excitation-pulse's temporal structure. Taking now a look at the retrieved temporal structure of the pulses used in the experiment (cf. Fig. 5.7), the specific behavior of the optical density OD(ω) in the pure solvent, can be understood even better. As the retrieved pulse shows predominately pre-pulses, the XPM effect is more expressed for positive time-delays. Since in the toy model a symmetrical pedestal was chosen, the spectro-temporal modulations are symmetric with respect to $\tau = 0$.

6.3. XPM effects imprinted on the resonant time-dependent dipole response

The question now arises how the presence of the pedestal in the excitation pulse impacts the real-time dipole response of the resonantly absorbing AlClPc. For this

investigation, the excited state is shifted from 4.7 eV to 1.85 eV, simplifying the molecular absorption band structure to a two-level system. In addition, the transition dipole moment was changed, such that for the control-pulse intensity I_{set} a change in the phase of the dipole response of $\pi/2$ is introduced. The course of the real-time dipole response for an excitation–control pulse time-delay of $\tau = 20.0$ fs is depicted in Figure 6.7. The top panel shows the real part of the excitation-pulse induced real-time dipole moment $\mathrm{Re}\{d(t)\}$ without the presence of the control pulse. In the second panel, the impact of the control-pulse interacting with the dipole response at the time delay $\tau = 20.0$ fs can be seen for the four chosen control-pulse intensities $I_{set}/4$, $I_{set}/2$, I_{set} and $1.8 \cdot I_{set}$. Panel 3 and 4 show the respective amplitude and control-pulse induced phase change. A direct comparison on how the real-time dipole response without the presence of the pedestal reacts under the influence of the control pulse for the same control-pulse parameters is depicted in Figure 6.8.

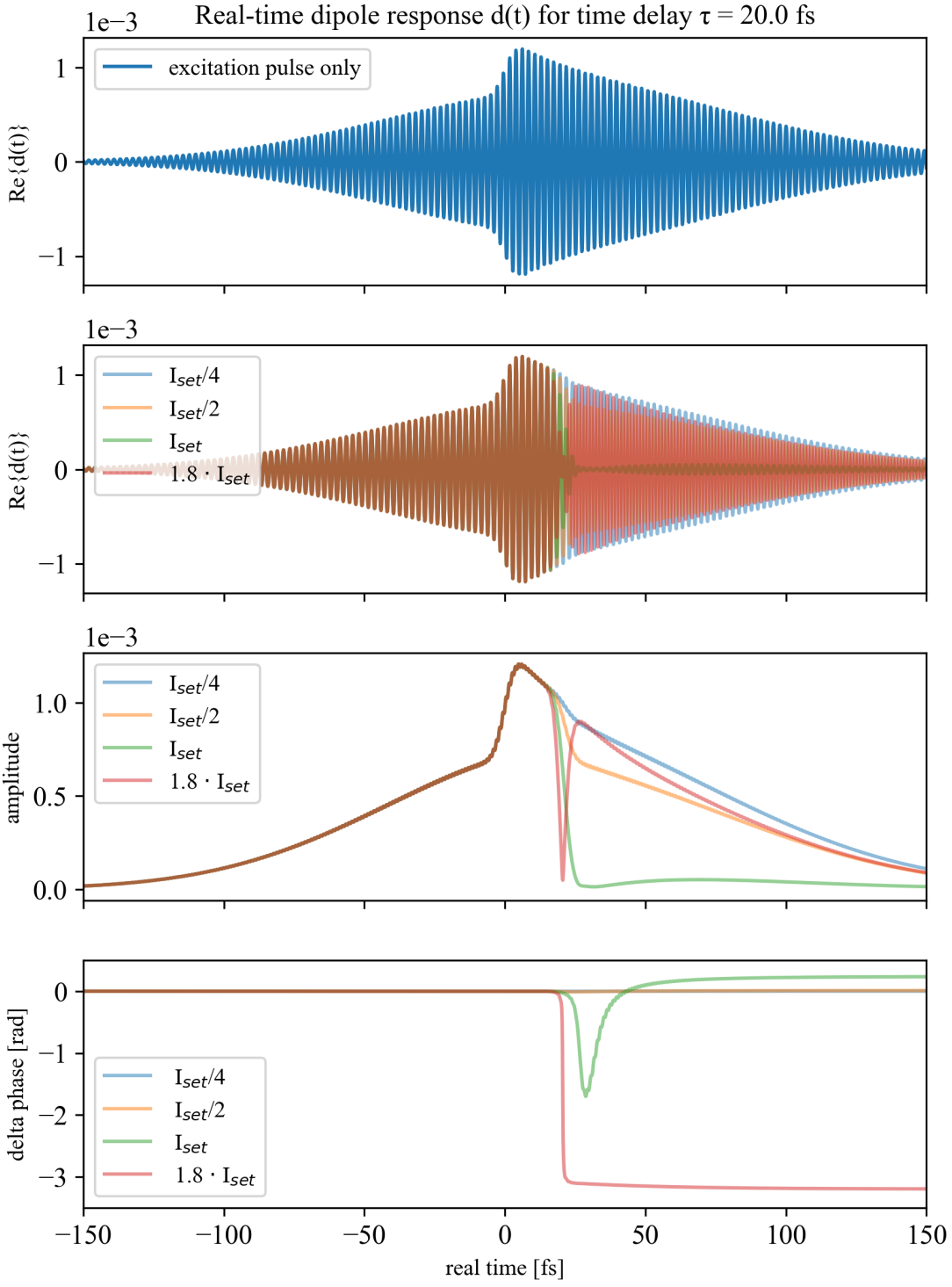

Figure 6.7.: Real-time dipole response d(t) for a 2-level system consisting of a ground state and one excited state at 1.85 eV. The excitation pulse is composed of a sum of a 5 fs FTL-pulse and a pedestal with a FWHM of 100 fs. This configuration is chosen to investigate how the real-time dipole moment of a resonantly absorbing medium behaves in the presence of the pulse pedestal. For a direct comparison without the excitation-pulse pedestal see Figure 6.8.

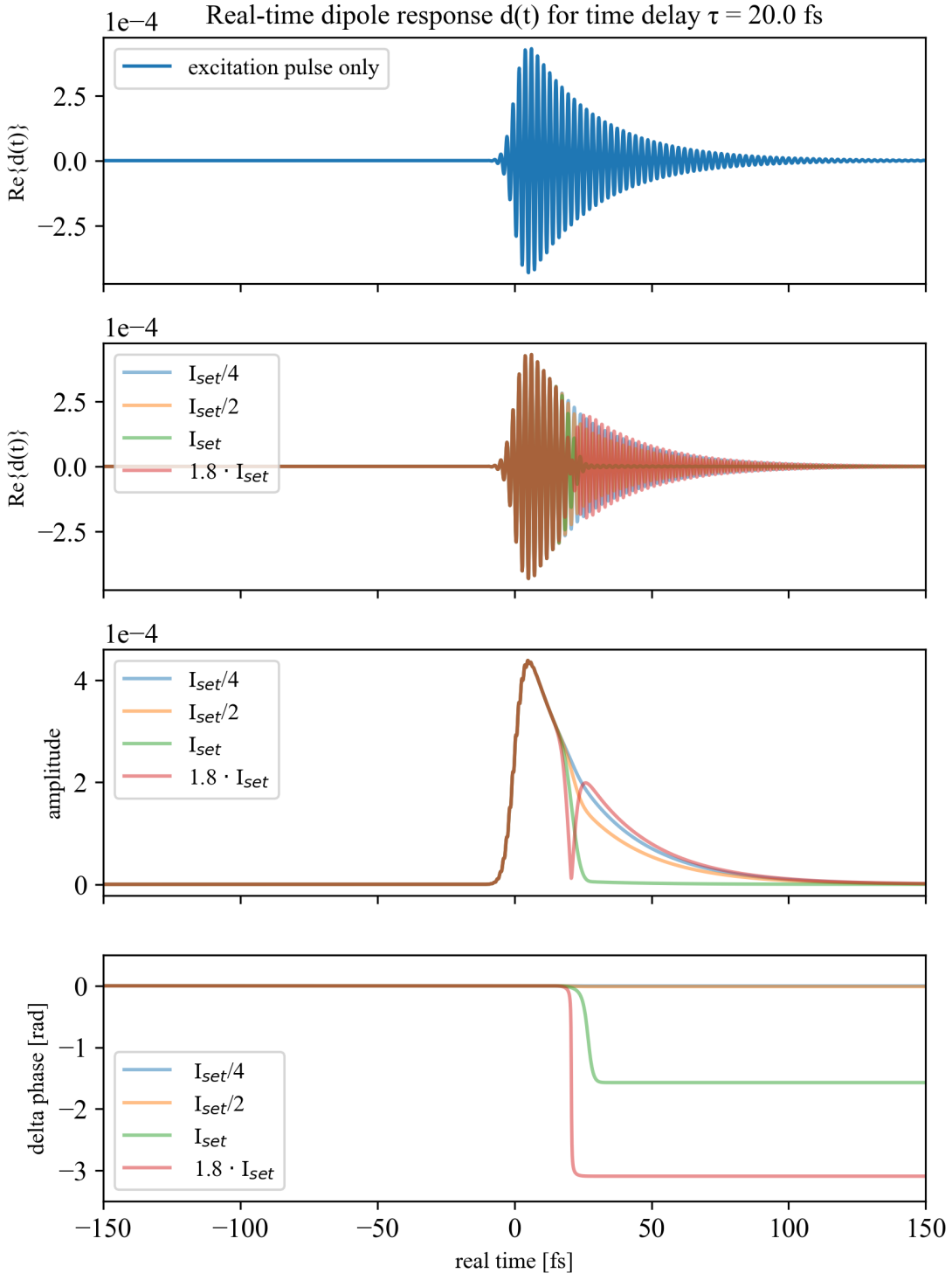

Figure 6.8.: Real-time dipole response d(t) of a simplified AlClPc target consisting of solely the ground state and one excited state at 1.85 eV. Here the excitation pulse was chosen to be a 5 fs FTL-pulse without pedestal. For a control-pulse intensity of I_{set} a phase change of $-\pi/2$ is introduced.

When comparing Fig. 6.7 to Fig. 6.8, the main differences can already be seen in the first panels, showing the real part of the real-time dipole response Re$\{d(t)\}$. In the ideal case of a short FTL-excitation pulse, the dipole response is initiated at t = 0 fs and freely evolves in time for times t > 0 (see top panel of Fig. 6.8). The manipulation of the real-time dipole response is, therefore, only possible for time-delays $\tau > 0$, as emphasized in the measurement concept. This leads to spectro-temporal modulations upon the absorbance for positive time-delays only (cf. Fig 6.1). In contrast, when the excitation pulse consists of a sharp FTL-pulse with a temporal pedestal, the unperturbed dipole response also has contributions for negative real times, as the dipole response follows the electric field (see top panel of Fig. 6.7). Since this real-time dipole response is non-zero for negative times, the control pulse is able to manipulate the induced dipole response not only for positive, but also for negative time-delays (see Figure 6.9). Regardless of the temporal pedestal, the amplitude of the dipole response reacts in a similar fashion to the influence of the control pulse for positive time-delays as can be seen in panels 3 of Figure 6.7 and 6.8, respectively. With increasing control-pulse intensity, the amplitude of the real-time dipole response is reduced, reaching a minimum for I_{set} in both cases. For higher control pulse intensities (here represented by the control-pulse intensity 1.8 $\cdot I_{set}$), Rabi-cycling can be observed. In both cases also the phase change of the dipole-response increases for increasing control-pulse intensity (see respective bottom panels of Fig. 6.7 and Fig. 6.8). Nonetheless, when analyzing the delta phase of the real-time dipole response, which was induced by the excitation pulse with pedestal, a complex phase course can be seen (bottom panel of Fig. 6.7), which does not remain constant after the interaction with the control pulse. This dephasing might be a result of the different phase behaviors of the cross-phase modulation and the resonant dipole control. As can be seen in Figure 6.4, the phase change induced by the control pulse in the cross-phase modulation is positive for the non-resonant interaction. In contrast, the control-pulse induced phase change for the resonant 2-level system without pedestal is negative (see Figure 6.8). Since both effects are present, it is not surprising that positive and negative changes to the phase behavior are possible (see bottom panel of Figure 6.7). The simulated optical density OD of the simplified 2-level AlClPC system excited by a pulse with temporal pedestal and manipulated by a control pulse with intensity I_{set} is depicted in the left panel of Figure 6.9.

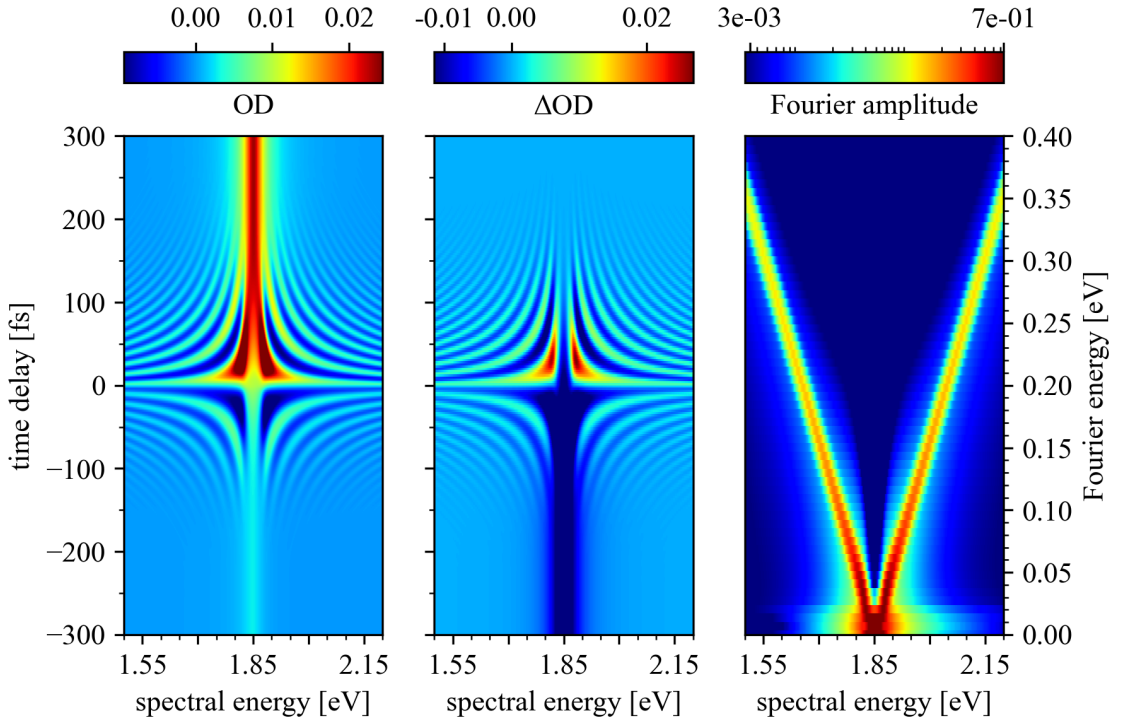

Figure 6.9.: Simulated time-delay-dependent optical density OD (left), differential OD (center) and corresponding Fourier plot (left) of a simplified AlClPc target consisting of only one excited state at 1.85 eV. The excitation pulse was chosen as a 5fs FTL-pulse with a 100 fs FWHM pedestal and the control-pulse intensity was set to I_{set}. In contrary to Fig. 6.1, modulations upon the OD can be observed for positive and negative time-delays.

Due to the presence of the pedestal, spectro-temporal modulations of the optical density can be observed for both, positive, as well as negative time-delays as already explained above. A step of the absorption line centered at 1.85 eV can be observed for negative time-delays which is associated to a ground-state bleach. The center panel of Fig. 6.9 shows the differential optical density ΔOD. This was obtained by subtraction of the excitation-pulse only absorbance from the time-delay trace. Direct comparison between the remaining modulations for positive and negative time-delays show, that the modulations for negative time-delays can be observed up to approx. -150 fs, while for positive time-delays the modulations are visible up to +250 fs. The resonant transition induces an asymmetry, which is not present in the simulation of the XPM in the pure solvent (see Figure 6.5 as a reference). The Fourier transform of the ΔOD reveals the already expected diagonals with slope +/-1. For completion and direct comparison to the XPM effects in the pure solvent, the Fourier amplitude and phase for positive time-delays only is shown in Figure 6.10. Both Fourier amplitude and phase are symmetric with respect to the resonance at 1.85 eV, which is in direct

contrast to the Fourier plots of the XPM effects in the pure solvent (see Fig. 6.6). Also here, the most pronounced change in the Fourier phase can be associated to the diagonals of slope +/-1 which can be nicely seen in the Fourier amplitude.

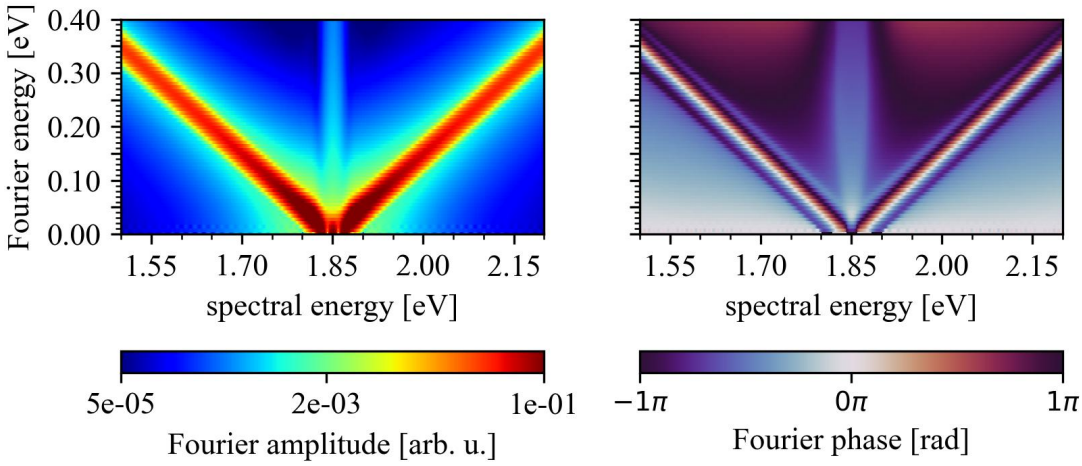

Figure 6.10.: Fourier amplitude and phase (left/right panel) for positive time-delays only ($\tau > 0$) of the ΔOD presented in Figure 6.9. Diagonals with slopes of +/-1 arise at the excited state's central energy of 1.85 eV. Both Fourier amplitude and phase are symmetric along 1.85 eV for higher/lower spectral energies. The most pronounced change in the Fourier phase is attributed to the +/-1 diagonals.

To explain the measured time-delay dependent optical density of the dissolved AlClPc molecules, presented in chapter 5.3.2, it is necessary to consider both, the XPM effects in the solvent, as well as the sum of both XPM and resonant effects in the AlClPc molecules. Under the assumption that the AlClPc molecules do not interact with the solvent, this can be achieved by calculating the time-dependent optical density for both cases independently using an excitation pulse with pedestal, followed by the addition of both ODs. This procedure is repeated for the four control-pulse intensities $I_{set}/4$, $I_{set}/2$, I_{set} and 1.8 $\cdot I_{set}$. The result for the control-pulse intensity I_{set} is shown in the left panel of Figure 6.11. As can directly be seen, the OD of the sum shows reduced spectro-temporal structures for spectral energies bigger than 1.85 eV, as compared to energies smaller than 1.85 eV. This is a result of the opposite changes in the dipole phase induced by the control pulse. While the phase change introduced in the pure solvent by the control pulse with an intensity of I_{set} is $+\pi/2$ (cf. Fig. 6.4), the phase induced in the resonant molecular case has a magnitude of $-\pi/2$, for a certain time window (cf. Fig. 6.7). The opposite sign of the phases, leads to opposed hyperbolic structures in the OD, which partially cancel out. Taking a

look at the Fourier amplitude (see Fig. 6.11 right panel), which was calculated from the ΔOD presented in the center panel of Fig. 6.11, a minimum structure upon the diagonal with slope +1 can be observed, while the diagonal with slope -1 seems to be mostly unaffected.

The observed minimum diagonal in the Fourier plot can be attributed to the partial cancellation of the spectro-temporal structures due to the opposite sign of the (control-pulse induced) phase changes in the pure solvent and the resonant molecular absorption.

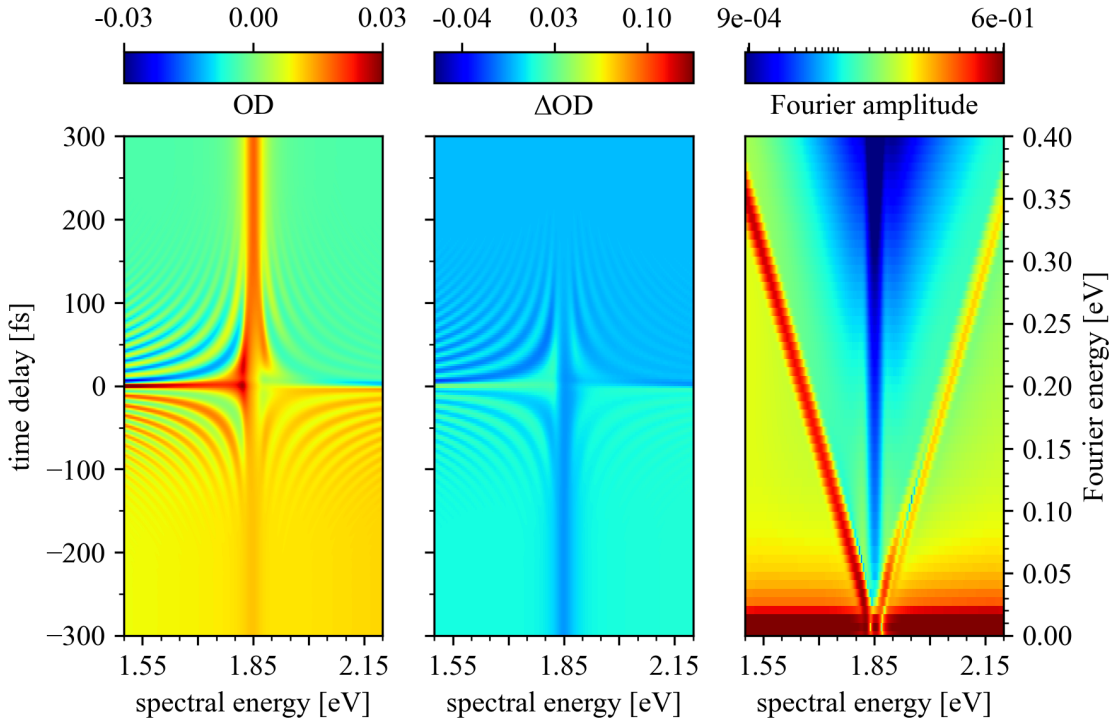

Figure 6.11.: The left panel shows the sum of the simulated optical densities calculated for the pure solvent (presented in Figure 6.5) and AlClPc with excitation-pulse pedestal (Figure 6.9) for control-pulse intensity I_{set}. The spectro-temporal modulations for energies > 1.85 eV are less pronounced in comparison to the ones for spectral energies < 1.85 eV, as can also be seen in the ΔOD (center panel) for both, positive and negative time delays. Fourier transformation of the ΔOD along the time-delay axis, reveals a Fourier energy plot (right panel) with a mostly unchanged diagonal with slope -1, while the diagonal with slope +1 shows an additional minimum.

To show the impact of the different control-pulse induced phase changes on the spectro-temporal modulations, lineouts through the simulated optical densities for all three cases: pure solvent with excitation-pulse pedestal (Fig. 6.5), resonant AlClPc with excitation-pulse pedestal (Fig. 6.9), and the sum of both (Fig. 6.11) for the control-pulse intensity I_{set}) are taken at a time-delay $\tau = 50$ fs. The lineouts are

summarized in Figure 6.12. It can be seen that for energies < 1.85 eV, both modulations, AlClPc (blue) and solvent (orange) are only phase-shifted by approximately $\pi/8$ leading to a high modulation amplitude of their sum (depicted as green curve) in this spectral energy range. For spectral energies > 1.85 eV, however, the modulations in OD between AlClPc and pure solvent are almost out of phase by π. This phase difference leads to a destructive interference of both signals, resulting in a less pronounced modulation for spectral energies > 1.85 eV.

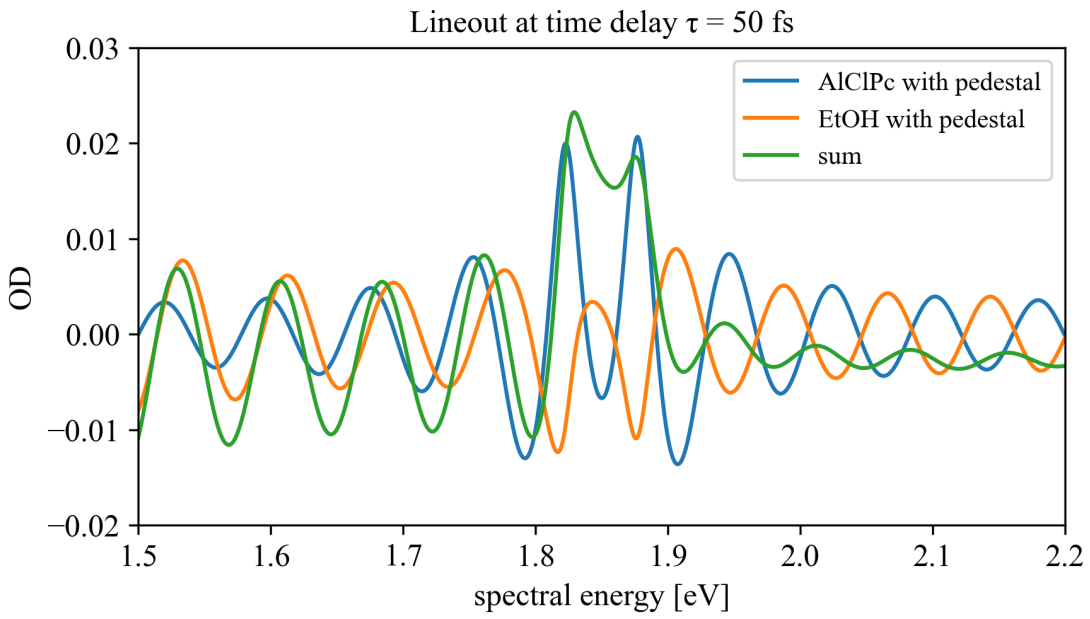

Figure 6.12.: Lineouts at time delay $\tau = 50$ fs through the ODs presented in Figures 6.5, 6.9 and 6.11. It can be seen that for energies > 1.85 eV the course of the simulated optical density of the pure solvent is almost out of phase by π compared to the OD of the resonant 2-level system representing the AlClPc molecules in a simplified manner. This phase difference leads to a destructive interference of both signals in their sum for energies above 1.85 eV.

Since the induced phase change is dependent on the control-pulse intensity, the Fourier plots (for positive time-delays only) of the sum OD are determined for different control-pulse intensities ($I_{set}/4$, $I_{set}/2$, I_{set} and $1.8 \cdot I_{set}$), as was done with the measurement data. Figure 6.13 summarizes both, Fourier amplitude and phase of the four simulated control-pulse intensities. A reduction in the Fourier amplitude of the diagonal with slope +1 can only be seen for a control-pulse intensity of I_{set} (see Fig. 6.13(C)), when the induced phase changes exactly lead to a destructive interference in the Fourier amplitude.

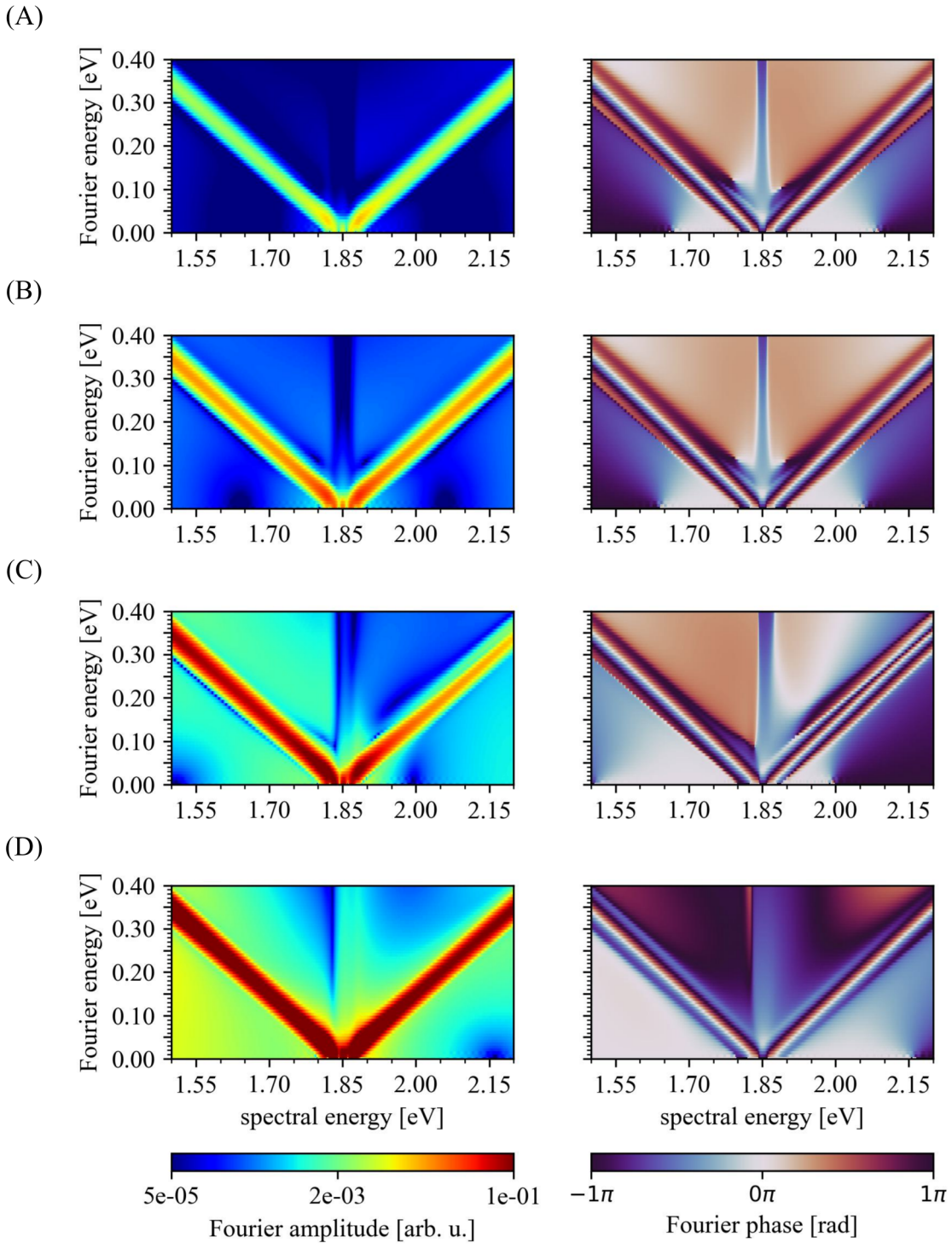

Figure 6.13.: Fourier amplitude and phase of the sum ΔOD for positive time delays only. The control-pulse intensities were chosen as: $I_{set}/4$ (A), $I_{set}/2$ (B), I_{set} (C) and 1.8 $\cdot I_{set}$ (D). The extinction of the diagonal with slope +1 emerging at 1.85 eV is only pronounced for a control-pulse intensity of I_{set} (panels (C)). Presumably for the other chosen control-pulse intensities the induced phases in the non-resonant and resonant case do not cancel out, as is the case for I_{set}. The corresponding Fourier phase shows one additional phase transition on the diagonal with slope +1 for intensity I_{set}.

In the corresponding Fourier phase for the case of I_{set} (Fig. 6.13(C)) one additional phase transition on the diagonal with slope +1 can be observed. The other calculated Fourier phases for control-pulse intensities $I_{set}/4$ (Fig. 6.13(A)), $I_{set}/2$ (Fig. 6.13(B)) and 1.8 $\cdot I_{set}$ (Fig. 6.13(D)) show a symmetric behavior.
To allow for a better comparison between the Fourier amplitude and phases of the sum OD for the four intensities depicted in Figure 6.13, lineouts for a fixed Fourier energy of 0.2 eV, as well as for a fixed spectral energy of 1.95 eV were taken. Lineouts of the individual cases before summation can be found in the appendix A.5. The lineouts of the sum OD's Fourier amplitude and phase for a fixed Fourier energy of 0.2 eV are summarized in Figure 6.14.

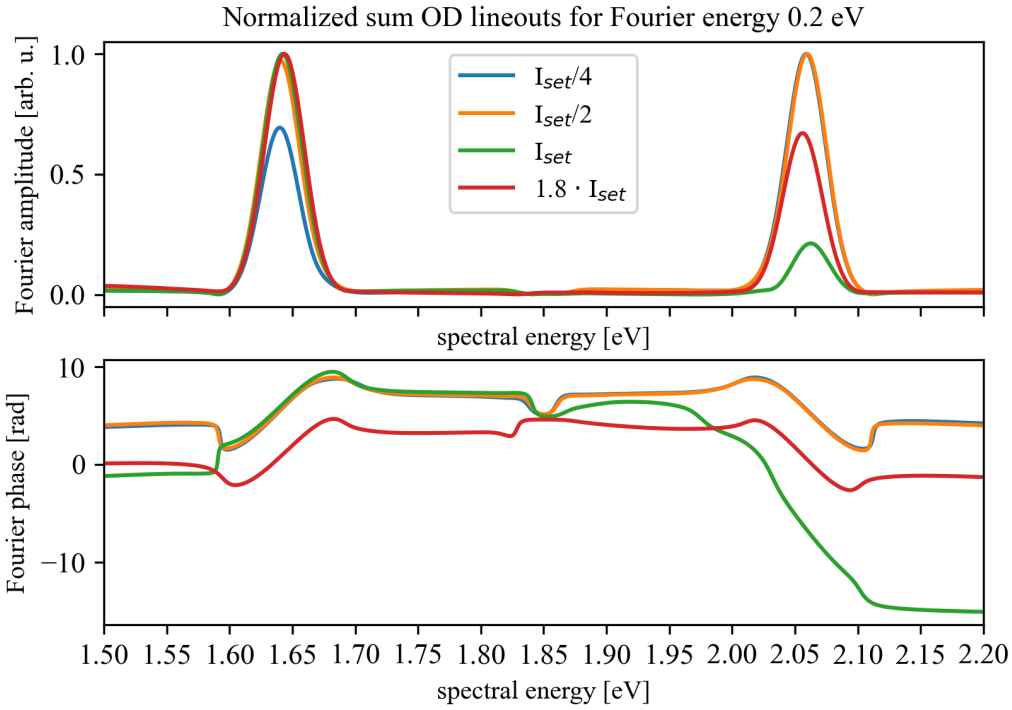

Figure 6.14.: Normalized spectral lineouts of the sum OD's Fourier amplitude and phase (top/bottom panel) for a selected Fourier energy of 0.2 eV. The lineouts of the Fourier amplitude are normalized to compare the minimum of the +1 slope diagonal for control-pulse intensity I_{set}. The peaks at 1.65 eV and 2.05 eV, hereby, correspond to the diagonals from Fig. 6.13. It can be clearly seen in the lineouts of the Fourier amplitude, that the contribution at 2.05 eV is strongly diminished for I_{set} (green curve) compared to the other intensities. Simultaneously, the Fourier phase undergoes a phase shift of several 2π in this specific spectral energy region.

Taking a look at the normalized Fourier amplitude lineouts (top panel of Fig. 6.14), the minimum in amplitude of the diagonal with slope +1 for control-pulse intensity I_{set} can directly be seen in the reduced peak centered at a spectral energy of approximately

2.05 eV. Simultaneously, the Fourier phase undergoes several 2π of phase shift in the spectral energy region between 2.00 eV and 2.10 eV. This seems to be linked to the destructive interference between both contributions (XPM of the solvent and resonant absorption of the molecule). For the control-pulse intensity $1.8 \cdot I_{set}$ only an overall phase offset of π can be observed. The asymmetry in the normalized Fourier amplitude for this intensity might be caused by a (intensity-dependent) potential coupling of the solvent to its excited state at 4.7 eV. Nonetheless, it seems that the Fourier amplitude contribution reaches its minimum for the control-pulse intensity I_{set}. This leads to the conclusion that the destructive interference between both resonant and non-resonant induced signals is intensity-dependent and reaches its minimum for the chosen control-pulse intensity I_{set}. The steep Fourier phase course can also be seen when taking lineouts for a fixed spectral energy of 1.95 eV for the different control-pulse intensities as shown in Figure 6.15.

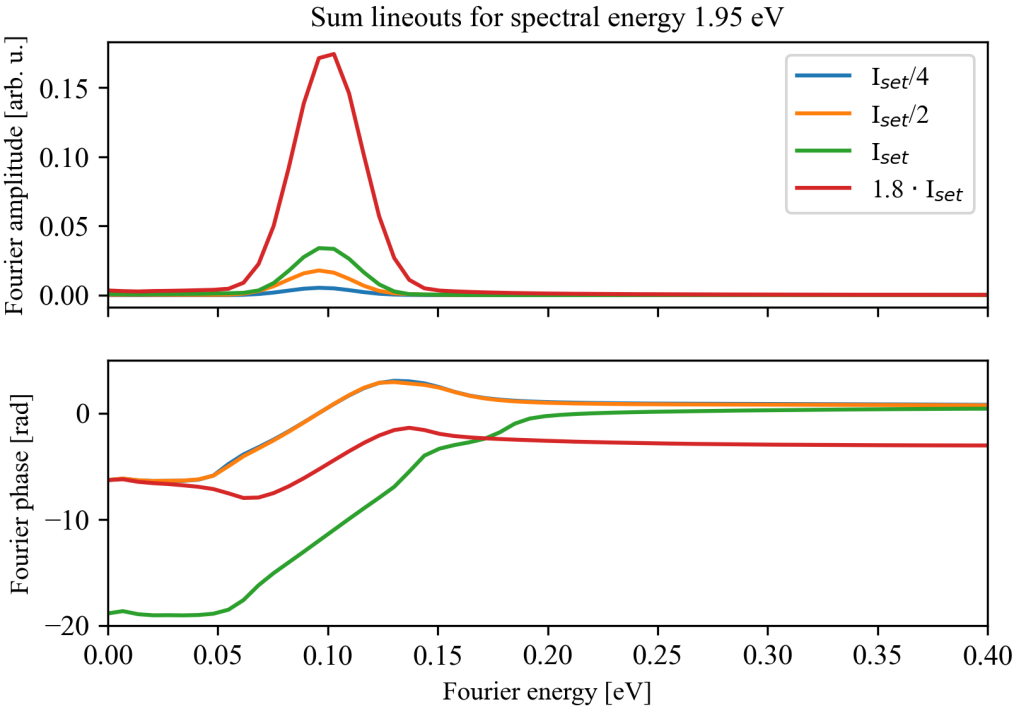

Figure 6.15.: Fourier lineouts for a spectral energy of 1.95 eV of the Fourier amplitude (top panel) and the Fourier phase (bottom panel). Also in this representation the Fourier phase for the case of control-pulse intensity I_{set} undergoes a significant total phase change, which is not observed for the Fourier phases of the other intensity cases. The minimum in the Fourier amplitude for control-pulse intensity I_{set} in this representation can be seen, when comparing Fig. 6.15 directly to the lineouts of the individual cases before summation, which can be found in the appendix in Fig. A.8 and Fig. A.6.

Comparing the simulated sum OD (depicted in Figure 6.11) with the measured

time-delay dependent absorbance of the dissolved AlClPc molecules shown in Figure 5.10 and 5.11 a qualitative agreement can be found. Furthermore, the minimum diagonals with slope +1, which can be observed in the Fourier energy plots of the dissolved AlClPc molecules (cf. Fig. 5.16) were nicely reproduced by the toy model (see right panel of Figure 6.11). The good qualitative agreement between simulation and experimental data suggests the destructive interference between both the molecular dipole response and the induced XPM in the solvent to take place, leading to destructive diagonals in the Fourier amplitude plots.

In total, this means that in the liquid-phase target, which consists of dissolved molecules and the solvent, two independent effects take place: the laser-induced resonant coupling in the molecule and the non-resonant laser-induced XPM effects in the solvent. For the latter of which, the pulse's temporal structure plays a significant role. Even though both, resonant and non-resonant laser-induced effects are independent of each other, they are able to interfere, giving rise to destructively interfering features in both, the optical density and the corresponding Fourier energy plots.

7. Conclusion and Outlook

For the first part of this thesis, which includes the measurement results presented in chapter 5.3.1 and the associated multi-level toy model presented in chapter 6.1 the following conclusion can be made: The direct comparison between the measured time-delay-dependent optical density (Fig. 5.8(A)) and the simulated trace (Fig. 6.1(B)) shows a good qualitative agreement. The toy model is able to reproduce the decrease in the overall absorption for negative time delays, as well as the observed hyperbolic structures on the absorbance converging towards the Q_I-band. In addition, also the slight splitting of the Q_I-band in the time delay range between 0 fs and 50 fs could be reproduced via the toy model, indicating the presence of coherent strong-field coupling effects. A qualitative agreement between experiment and model was also achieved in the Fourier energy plot for positive time-delays only depicted in Figure 6.1(C), where diagonals of slope +/-1 linked to the Q_I-bands spectral energy appear in the same fashion as in the experimental data (see Fig. 5.9(A)). The hyperbolic spectro-temporal modulations of the absorption spectrum, as well as the diagonals in the Fourier-energy plot for positive time-delays only can, therefore, be realized and understood with the presented atom-like multi-level model. The good structural agreement between the simulation results and the experimental observation shows that coherent strong-coupling effects are at work in the laser-driven target. Both, experimental and simulated results imply that the coherent control of the absorption spectrum through strong-field light–matter interaction in the liquid phase is possible.

The second part of this thesis investigated the impact of the control-pulse intensity on the laser-driven absorbance of the dissolved AlClPc target, as well as the solvent itself. It includes the measurement results presented in chapter 5.3.2 and the associated 2-level toy model presented in chapters 6.2 and 6.3. Comparing the measured time-delay-dependent absorbance of the pure solvent (Fig. 5.10 and 5.11) with the simulated trace depicted in Figure 6.5, it can be said that the toy model is able to reproduce spectro-temporal modulations which solely depend on the excitation pulse's temporal structure. A qualitative agreement between measurement data of the pure solvent and

the toy model could also be achieved in the Fourier energy plot for positive time-delays only depicted in Figure 6.5, where diagonals of slope +/-1 linked to the center energy of the excitation pulse appear in agreement with to the experimental data (see Fig. 5.19). The spectro-temporal modulations measured in the absorbance of the pure solvent, as well as the diagonals in the Fourier-energy plot for both positive and negative time delays can be realized and understood by the implementation of a temporally extended excitation pulse consisting of a FTL-pulse on top of a temporal pedestal non-resonantly acting on a simplified two-level system. The good agreement between experimental data and simulation suggests the cross-phase modulation effect to take place in the vicinity of the solvent. In addition, the impact of the intense laser pulses upon a target consisting of both, solvent and AlClPc molecules was modeled by simplifying both to individual, independent 2-level systems, one off-resonant and one resonant to the laser pulses. Subsequently, both calculated time-delay-dependent absorbances are summed to a total OD (depicted in Figure 6.11). The modeled sum OD shows good qualitative agreement with the measured time-delay-dependent absorbance of the dissolved AlClPc molecules depicted in Figure 5.10 and 5.11. Qualitative agreement between experiment and toy model was also achieved in the corresponding Fourier energy plots for both Fourier amplitude and phase. The destructive minimum diagonal with slope +1, which can be seen in the right panel of Figure 6.11 can also be observed in a similar fashion in the Fourier amplitude plots of the dissolved AlClPc molecules (Fig. 5.16). The good qualitative agreement between the simulation and the experimental data suggests that destructive interference between both the molecular dipole response and induced XPM in the solvent leads to the minimum in the positive diagonal of the Fourier amplitude.

To summarize, time-dependent coherent modifications of the ground-state absorption spectrum attributed to the Q-band of AlClPc molecules in the liquid phase could be observed within this thesis. By comparing the experimental data to an atom-like multi-level model simulation, the spectro-temporal structures in the optical density could be qualitatively reproduced and identified, as a strong-field coupling between the ground state and a bath of excited states. Furthermore, in the second part of this thesis, a simplified 2-level toy model was used to reproduce spectro-temporal modulations measured in the pure solvent. The simplified toy model indicates that these modulations can be associated with XPM effects due to a non-trivial laser-pulse structure. When taking both the solvent and the AlClPc molecules into consideration, a minimum in the positive diagonal of the Fourier amplitude appears, which in turn

can be associated to a destructive interference between the control-pulse induced XPM effects in the solvent and the resonant control of the molecule's dipole response. Therefore, by controlling the dipole response with moderately strong fields, it is possible to understand and control the coherent ultrafast dynamics of complex systems in solution under the influence of intense light fields.

On the basis of this thesis' findings, a deeper insight into the intrinsic mechanisms behind light-matter interaction in the liquid phase can be obtained. One interesting follow-up experiment could be to conduct the measurement for a target containing aggregates of multiple molecules (clusters) to determine whether they show a similar behavior under the influence of strong laser fields, as compared to the monomeric state. To the best of the author's knowledge, it is still an open question how the environment of the molecules changes their electronic coherences under the influence of strong-laser fields on ultrafast timescales. Furthermore, the implementation of a pulse shaper, opening up the possibility to directly access the laser-pulses' temporal structure and spectrum, would be beneficial. By controlling the laser pulses in such a manner, XPM effects in the solvent could be reduced or even intentionally used to imprint a desired signal onto the target, thereby allowing for a femtosecond "switch". Due to the versatility of the measurement setup, the study of strong-field induced coherent control is not restricted to AlClPc, but can be employed on different liquids or even solid samples, without applying major modifications to the experimental setup.

A. Appendix

A.1. Atomic units

Within the field of atomic and molecular physics, the prototype hydrogen provides the scale on which physical quantities are measured. It is used to define the system of atomic units (a.u.), where the following conventions apply: $m_e = e = \hbar = 1/(4\pi\epsilon_0) = 1$. Important quantities for this work were rescaled in atomic units and are summarized here:

Unit	Definition	Value
Length	$a_0 = 4\pi\epsilon_0\hbar^2/m_e e^2$	$5.292 \cdot 10^{-11}$ m
Energy	$E_h = e^2/4\pi\epsilon_0 a_0 = \alpha^2 m_e c^2$	27.2114 eV
Velocity	$v_0 = e^2/4\pi\epsilon_0\hbar c = \alpha c$	$2.188 \cdot 10^6$ m/s
Time	$\frac{a_0}{v_0} = \hbar/E_h$	$2.419 \cdot 10^{-17}$ s
Field strength	$E_0 = e/4\pi\epsilon_0 a_0^2$	$5.142 \cdot 10^{11}$ V/m
Intensity	$I_0 = \frac{1}{2}\epsilon_0 c E_0^2$	$3.509 \cdot 10^{16}$ W/cm^2

Table A.1.: Quantities used in the numerical simulations rescaled in atomic units.

A.2. Different nomenclature systems of electronic transitions in molecules

When moving in the area of transient absorption spectroscopy in molecules one makes the acquaintance with a multitude of different notations regarding states and their electronic transitions. To prevent confusion three of the most common notations are summarized in Table A.2 from the simplest to the most complex system. The most simple notation uses an enumerative system, which only differentiates between singlet and triplet states and gives no further details on the transition-involved electron(s). The second listed notation (which was chosen within the scope of this theses) is based on the system after the American spectroscopist Michael Kasha. Here the electronic

states are named after the molecular orbital they occupy. Using this notation the electronic transitions specify the molecular orbitals involved. The most complete (and therefore complex) notation is based on group theory. It specifies electronic states via the symmetry of the system under investigation. For a vivid example, the reader might have a look back at Figure 2.4, where molecular orbitals of benzene are depicted. Here group theory notation can distinguish between the different π-states based on the geometry of the molecular orbitals.

System	State icons	States	Electronic transitions
enumerative	S_0	singlet ground state	$S_0 \rightarrow S_1$
	$S_1, S_2, S_3...$	higher singlet states	$S_0 \rightarrow S_2$
	$T_1, T_2, T_3...$	triplet state	$T_1 \rightarrow T_2$
after Kasha	σ, π, n	starting orbitals	$\sigma \rightarrow \sigma^*$
	σ^*, π^*	orbitals of excited states	$\pi \rightarrow \pi^*$
group theory		based on symmetry classes	
	A_{ij}	symmetric state	${}^1B_{1u} \leftarrow {}^1A_{1g}$
	B_{ij}	anti-symmetric state	${}^1B_{2u} \leftarrow {}^1A_{1g}$
	E_{ij}	2-fold degenerated state	${}^1E_{1u} \leftarrow {}^1A_{1g}$

Table A.2.: Summary of three common nomenclatures/representations of electronic states and their transitions in molecules.

Supplement to the symmetry considerations: A/B are symmetric/anti-symmetric about the rotation-axis C_n. $i = 1, 2$ depends on whether the state is symmetric or anti-symmetric to the C_2-axes perpendicular to C_n, while $j = g, u$, meaning symmetric and anti-symmetric with respect to inversion.

A.3. Efficiency curves

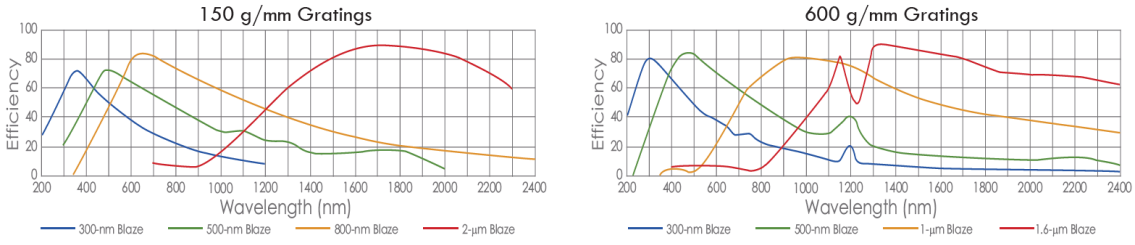

Figure A.1.: Grating efficiency curves for both 150 grooves/mm and 600 grooves/mm gratings. Image reprinted from [93].

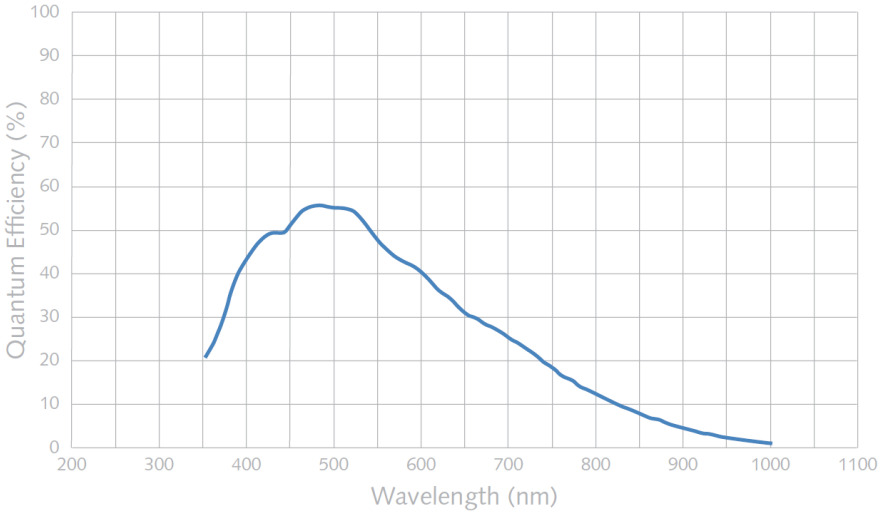

Figure A.2.: Quantum efficiency curve for the used CoolSNAP K4 CCD camera. Image reprinted from [94].

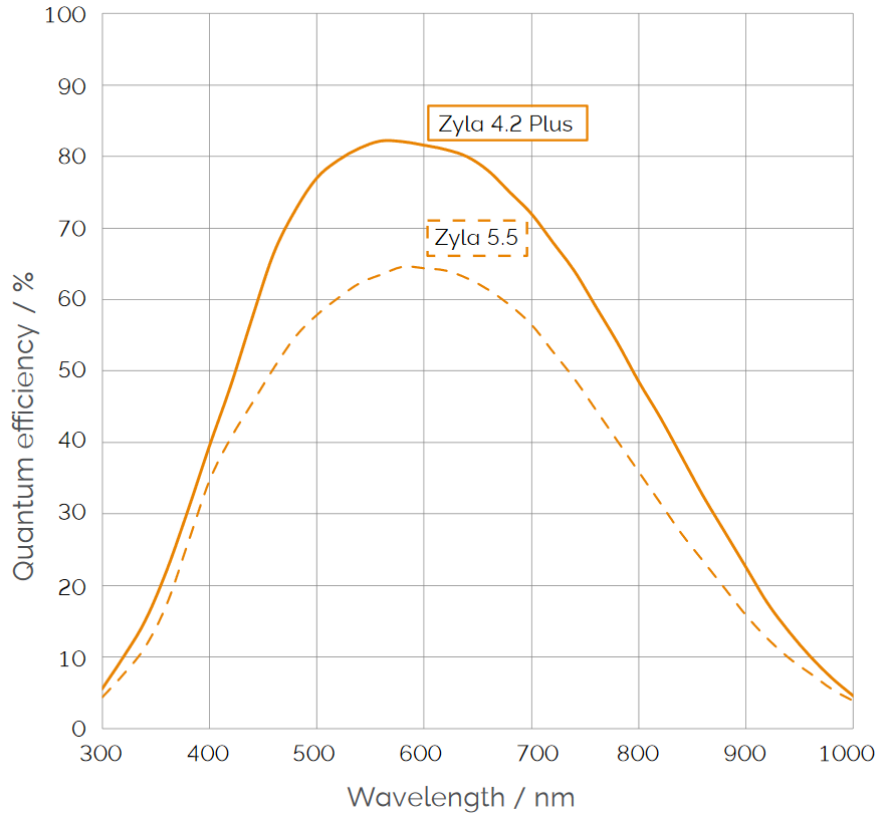

Figure A.3.: Quantum efficiency curve for the used Zyla 5.5 sCMOS camera. Image reprinted from [95].

A.4. Datasheet of beamsplitter

Coating 114039

LAYERTEC® OPTICAL COATINGS · OPTICS

PRp(45°,540-950nm)=80(±3)% |GDD-Rp,Tp(45°,540-950nm)|<60fs²

fig. 1 reflection PR-region 45°

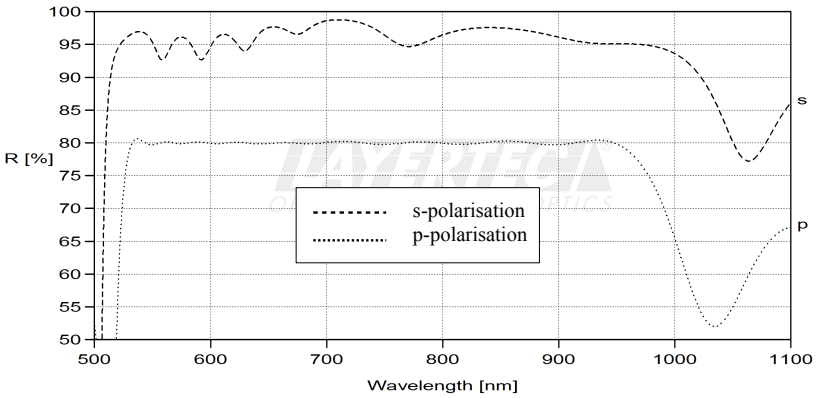

fig. 2 calculated GDD(R,45°)

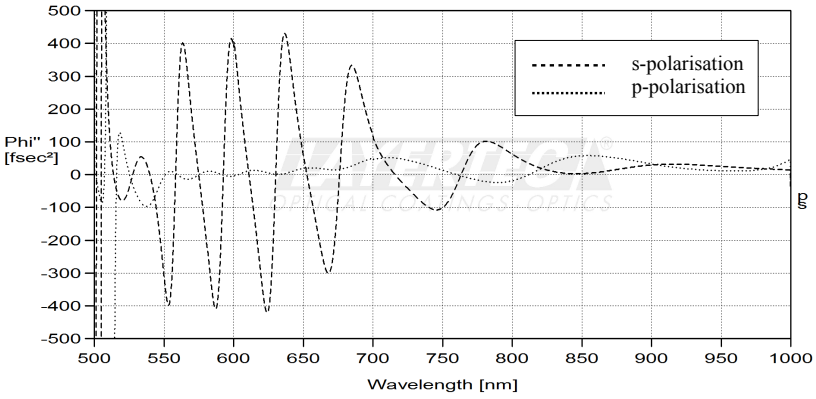

page 1 (2) non binding principle curve

Figure A.4.: Reflectivity and group delay dispersion of the used beamsplitter. Datasheet reprinted from [96].

A.5. Fourier lineouts of the individual cases before summation

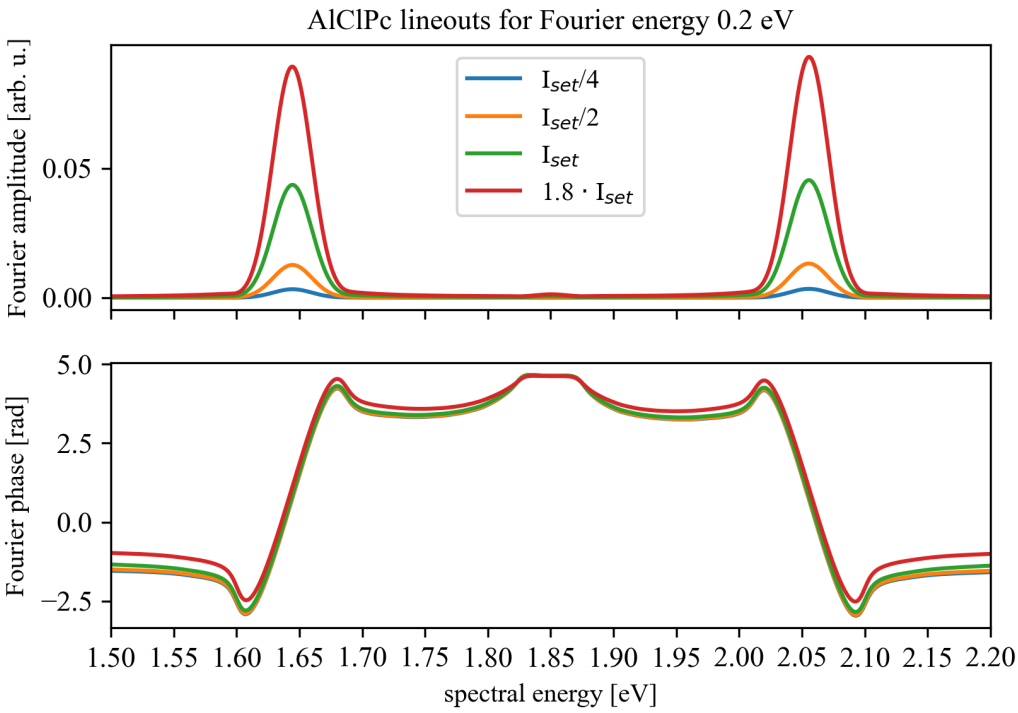

Figure A.5.: Spectral lineouts of the Fourier amplitude (top panel) and Fourier phase (bottom panel) for a fixed Fourier energy of 0.2 eV. For this part of the simulation the AlClPc was simplified to a 2-level system. Furthermore the excitation pulse was chosen to have a temporal pedestal with a FHWM of 100 fs. The magnitude of the Fourier amplitude increases with increasing control-pulse intensity, as expected. The Fourier phase course shows a steep phase change in the region of the diagonals and is constant outside these regions.

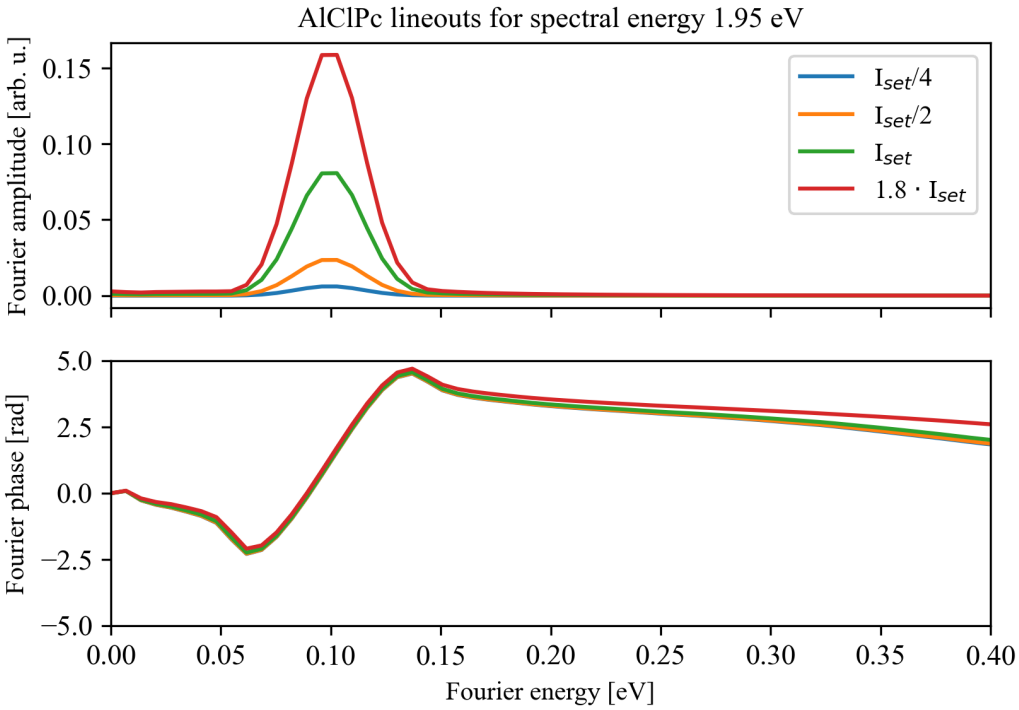

Figure A.6.: Fourier lineout for a spectral energy of 1.95 eV of the Fourier amplitude (top panel) and Fourier phase (bottom panel). Also in this representation an increase in the control-pulse intensity leads to an increase of the Fourier amplitude of the coupling diagonals as expected. The most pronounced feature in the course of the Fourier phase, can be linked to the peak in the Fourier amplitude.

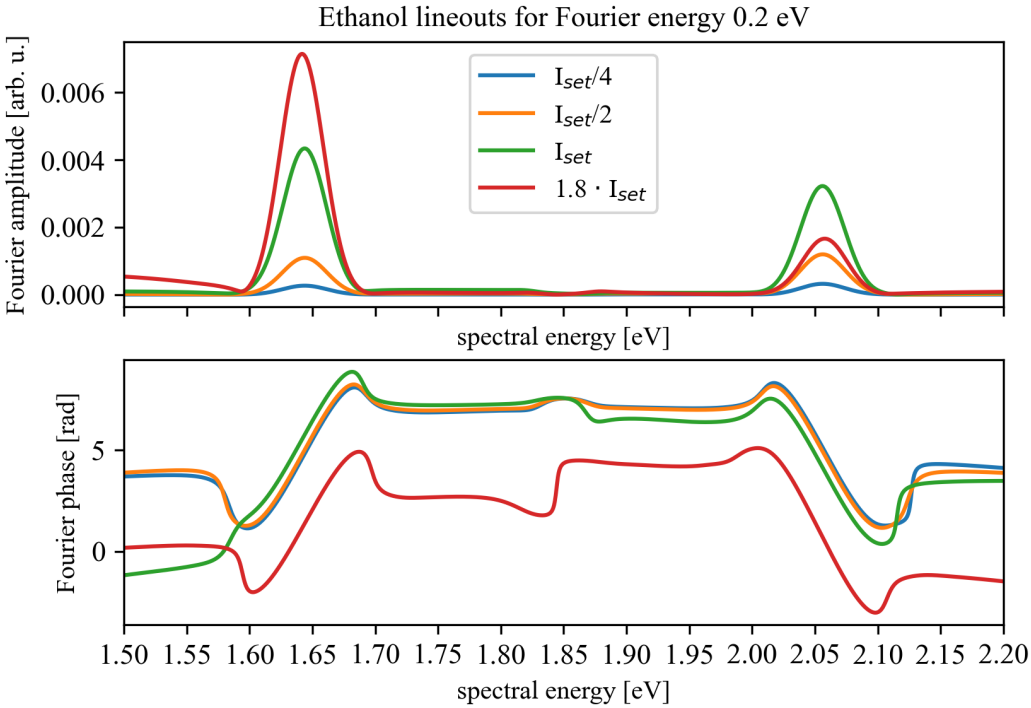

Figure A.7.: Spectral lineouts of the Fourier amplitude (top panel) and Fourier phase (bottom panel) for a fixed Fourier energy of 0.2 eV. For this part of the simulation the solvent was modeled as a 2-level system, with an off-resonant excited state at 4.7 eV. Furthermore the excitation pulse was chosen to have a temporal pedestal with a FHWM of 100 fs. The magnitude of the Fourier amplitude increases with increasing control-pulse intensity up to I_{set}. For the control-pulse intensity 1.8 $\cdot I_{set}$ a coupling to the excited state get's possible leading to an asymmetry in the Fourier amplitude of the diagonals. Also the corresponding Fourier phase shows a different behavior compared to the lower control-pulse intensities.

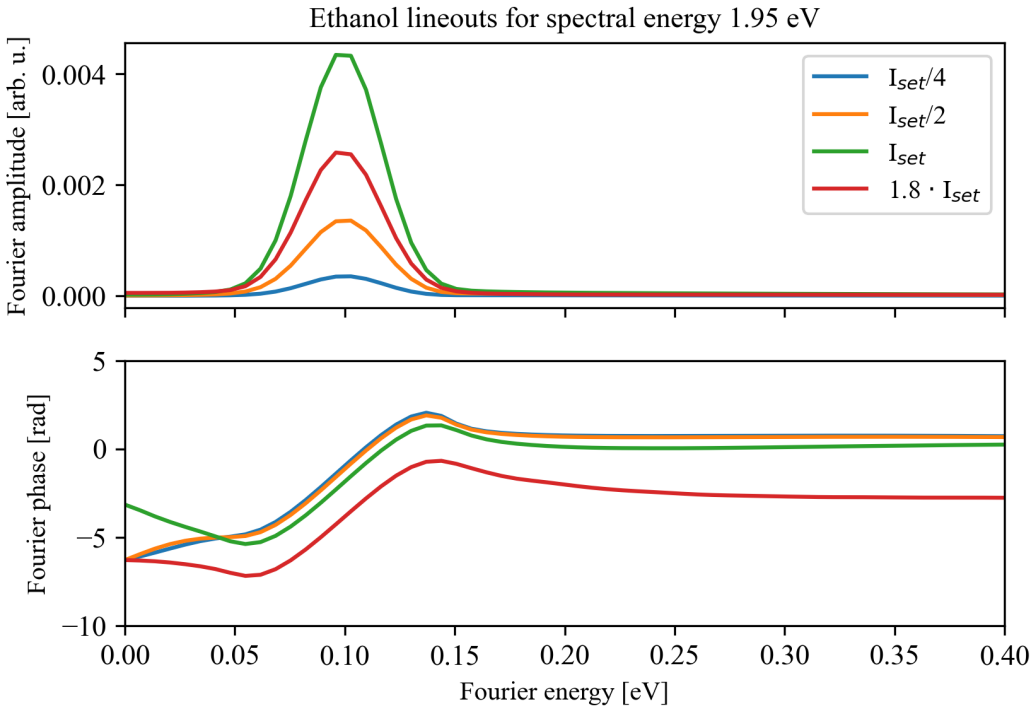

Figure A.8.: Fourier lineout for a spectral energy of 1.95 eV of the Fourier amplitude and phase (top/bottom panel). As this is only a different representation of the same data set, the same trends as in Fig. A.7 can be seen for both Fourier amplitude and phase.

List of publications

The following publication is used within this thesis:

- C. da Costa Castanheira, A. Persch, P. Birk, C. Ott, T. Pfeifer. *Laser-Induced Control of the Optical Response of Aluminum Phthalocyanine Chloride Complexes Dissolved in Ethanol.* Frontiers in Physics 9:627826, 2021.

Additional publications, which are not used within this thesis:

- M. Rebholz, T. Ding, V. Despré, L. Aufleger, M. Hartmann, K. Meyer, V. Stooß, A. Magunia, D. Wachs, P. Birk, Y. Mi, G. D. Borisova, C. da Costa Castanheira, P. Rupprecht, G. Schmid, K. Schnorr, C. D. Schröter, R. Moshammer, Z.-H. Loh, A. R. Attar, S. R. Leone, T. Gaumnitz, H. J. Wörner, S. Roling, M. Butz, H. Zacharias, S. Düsterer, R. Treusch, G. Brenner, J. Vester, A. I. Kuleff, C. Ott, and T. Pfeifer. *All-XUV pump-probe transient absorption spectroscopy of the structural molecular dynamics of diiodomethane.* Phys. Rev. X 11:031001, 2021.

- M. Rebholz, T. Ding, L. Aufleger, M. Hartmann, K. Meyer, V. Stooß, A. Magunia, D. Wachs, P. Birk, Y. Mi, G. D. Borisova, C. da Costa Castanheira, P. Rupprecht, M. Magrakvelidze, U. Thumm, S. Roling, M. Butz, H. Zacharias, S. Düsterer, R. Treusch, G. Brenner, C. Ott, and T. Pfeifer. *XUV-Initiated Dissociation Dynamics of Molecular Oxygen.* J. Phys. Chem. A 125:10138–10143, 2021.

- T. Ding, M. Rebholz, L. Aufleger, M. Hartmann, V. Stooß, A. Magunia, P. Birk, G. D. Borisova, C. da Costa Castanheira, P. Rupprecht, Y. Mi, T. Gaumnitz, Z.-H. Loh, S. Roling, M. Butz, H. Zacharias, S. Düsterer, R. Treusch, C. Ott, and T. Pfeifer. *XUV pump–XUV probe transient absorption spectroscopy at FELs.* Faraday Discuss. 228:519-536, 2021.

- T. Ding, M. Rebholz, L. Aufleger, M. Hartmann, V. Stooß, A. Magunia, P. Birk, G. D. Borisova, D. Wachs, C. da Costa Castanheira, P. Rupprecht, Y. Mi, A. R.

Attar, T. Gaumnitz, Z.-H. Loh, S. Roling, M. Butz, H. Zacharias, S. Düsterer, R. Treusch, A. Eislage, S. M. Cavaletto, C. Ott, and T. Pfeifer. *Measuring the frequency chirp of extreme-ultraviolet free-electron laser pulses by transient absorption spectroscopy.* Nature Communications 12:643, 2021.

- T. Ding, M. Rebholz, L. Aufleger, M. Hartmann, K. Meyer, V. Stooß, A. Magunia, D. Wachs, P. Birk, Y. Mi, G. D. Borisova, C. da Costa Castanheira, P. Rupprecht, Z.-H. Loh, A. R. Attar, T. Gaumnitz, S. Roling, M. Butz, H. Zacharias, S. Düsterer, R. Treusch, S. M. Cavaletto, C. Ott, and T. Pfeifer. *Nonlinear Coherence Effects in Transient-Absorption Ion Spectroscopy with Stochastic Extreme-Ultraviolet Free-Electron Laser Pulses.* Phys. Rev. Lett. 123:103001, 2019.

- C. Ott, L. Aufleger, T. Ding, M. Rebholz, A. Magunia, M. Hartmann, V. Stooß, D. Wachs, P. Birk, G. D. Borisova, K. Meyer, P. Rupprecht, C. da Costa Castanheira, R. Moshammer, A. R. Attar, T. Gaumnitz, Z. H. Loh, S. Düsterer, R. Treusch, J. Ullrich, Y. Jiang, M. Meyer, P. Lambropoulos, and T. Pfeifer., *Strong-field extreme-ultraviolet dressing of atomic double excitation.* Phys. Rev. Lett. 123:163201, 2019.

Bibliography

[1] A. L. Schawlow and C. H. Townes. Infrared and optical masers. *Phys. Rev.*, 112: 1940–1949, Dec 1958. doi: 10.1103/PhysRev.112.1940. URL https://link.aps.org/doi/10.1103/PhysRev.112.1940.

[2] T H MAIMAN. Stimulated Optical Radiation in Ruby. *Nature*, 187(4736): 493–494, 1960. ISSN 1476-4687. doi: 10.1038/187493a0. URL https://doi.org/10.1038/187493a0.

[3] F J McClung and R W Hellwarth. Giant Optical Pulsations from Ruby. *Journal of Applied Physics*, 33(3):828–829, mar 1962. ISSN 0021-8979. doi: 10.1063/1.1777174. URL https://doi.org/10.1063/1.1777174.

[4] Willis E. Lamb. Theory of an optical maser. *Phys. Rev.*, 134:A1429–A1450, Jun 1964. doi: 10.1103/PhysRev.134.A1429. URL https://link.aps.org/doi/10.1103/PhysRev.134.A1429.

[5] L E Hargrove, R L Fork, and M A Pollack. LOCKING OF He–Ne LASER MODES INDUCED BY SYNCHRONOUS INTRACAVITY MODULATION. *Applied Physics Letters*, 5(1):4–5, jul 1964. ISSN 0003-6951. doi: 10.1063/1.1754025. URL https://doi.org/10.1063/1.1754025.

[6] D. E. Spence, P. N. Kean, and W. Sibbett. 60-fsec pulse generation from a self-mode-locked ti:sapphire laser. *Opt. Lett.*, 16(1):42–44, Jan 1991. doi: 10.1364/OL.16.000042. URL http://opg.optica.org/ol/abstract.cfm?URI=ol-16-1-42.

[7] U. Keller, G. W. 'tHooft, W. H. Knox, and J. E. Cunningham. Femtosecond pulses from a continuously self-starting passively mode-locked ti:sapphire laser. *Opt. Lett.*, 16(13):1022–1024, Jul 1991. doi: 10.1364/OL.16.001022. URL http://opg.optica.org/ol/abstract.cfm?URI=ol-16-13-1022.

[8] Donna Strickland Gerard and Mourou. Compression of amplified chirped optical pulses. *Optics Communications*, 56(3):219–221, 1985. ISSN 0030-4018. doi: 10.1016/0030-4018(85)90120-8. URL http://www.sciencedirect.com/science/article/pii/0030401885901208.

[9] Brett J. Weinacht, Thomas; Pearson. *Time-Resolved Spectroscopy: An Experimental Perspective*. CRC Press, 2019.

[10] Shaul Mukamel. *Principles of Nonlinear Optical Spectroscopy*. Oxford University Press, Inc., 1995.

[11] Jennifer L Herek, Wendel Wohlleben, Richard J Cogdell, Dirk Zeidler, and Marcus Motzkus. Quantum control of energy flow in light harvesting. *Nature*, 417(6888):533–535, 2002. ISSN 1476-4687. doi: 10.1038/417533a. URL https://doi.org/10.1038/417533a.

[12] T Brixner, N H Damrauer, P Niklaus, and G Gerber. Photoselective adaptive femtosecond quantum control in the liquid phase. *Nature*, 414(6859):57–60, 2001. ISSN 1476-4687. doi: 10.1038/35102037. URL https://doi.org/10.1038/35102037.

[13] Yin Song, Alexander Schubert, Elizabeth Maret, Ryan K Burdick, Barry D Dunietz, Eitan Geva, and Jennifer P Ogilvie. Vibronic structure of photosynthetic pigments probed by polarized two-dimensional electronic spectroscopy and ab initio calculations. *Chemical Science*, 10(35):8143–8153, 2019. ISSN 2041-6520. doi: 10.1039/C9SC02329A. URL http://dx.doi.org/10.1039/C9SC02329A.

[14] Christian Ott, Andreas Kaldun, Luca Argenti, Philipp Raith, Kristina Meyer, Martin Laux, Yizhu Zhang, Alexander Blättermann, Steffen Hagstotz, Thomas Ding, Robert Heck, Javier Madroñero, Fernando Martín, and Thomas Pfeifer. Reconstruction and control of a time-dependent two-electron wave packet. *Nature*, 516(7531):374–378, 2014. ISSN 1476-4687. doi: 10.1038/nature14026. URL https://doi.org/10.1038/nature14026.

[15] M Wollenhaupt, A Präkelt, C Sarpe-Tudoran, D Liese, and T Baumert. Quantum control by selective population of dressed states using intense chirped femtosecond laser pulses. *Applied Physics B*, 82(2):183–188, 2006. ISSN 1432-0649. doi: 10.1007/s00340-005-2066-0. URL https://doi.org/10.1007/s00340-005-2066-0.

[16] Johannes Schneider, Matthias Wollenhaupt, Andreas Winzenburg, Tim Bayer, Jens Köhler, Rüdiger Faust, and Thomas Baumert. Efficient and robust strong-field control of population transfer in sensitizer dyes with designed femtosecond laser pulses. *Physical Chemistry Chemical Physics*, 13(19):8733–8746, 2011. ISSN 1463-9076. doi: 10.1039/C0CP02723E. URL http://dx.doi.org/10.1039/C0CP02723E.

[17] Brian Kaufman, Tamás Rozgonyi, Philipp Marquetand, and Thomas Weinacht. Coherent control of internal conversion in strong-field molecular ionization. *Phys. Rev. Lett.*, 125:053202, Jul 2020. doi: 10.1103/PhysRevLett.125.053202. URL https://link.aps.org/doi/10.1103/PhysRevLett.125.053202.

[18] Moshe Shapiro and Paul Brumer. Coherent control of atomic, molecular, and electronic processes. volume 42 of *Advances In Atomic, Molecular, and Optical Physics*, pages 287 – 345. Academic Press, 2000. doi: 10.1016/S1049-250X(08)60189-5. URL http://www.sciencedirect.com/science/article/pii/S1049250X08601895.

[19] Marcos Dantus. Coherent nonlinear spectroscopy: From femtosecond dynamics to control. *Annual Review of Physical Chemistry*, 52(1):639–679, 2001. doi: 10.1146/annurev.physchem.52.1.639. URL https://doi.org/10.1146/annurev.physchem.52.1.639. PMID: 11326077.

[20] Kenji Ohmori. Wave-packet and coherent control dynamics. *Annual Review of Physical Chemistry*, 60(1):487–511, 2009. doi: 10.1146/annurev.physchem.59.032607.093818. PMID: 19335221.

[21] He Wang, Michael Chini, Shouyuan Chen, Chang-Hua Zhang, Feng He, Yan Cheng, Yi Wu, Uwe Thumm, and Zenghu Chang. Attosecond time-resolved autoionization of argon. *Phys. Rev. Lett.*, 105:143002, Oct 2010. doi: 10.1103/PhysRevLett.105.143002. URL https://link.aps.org/doi/10.1103/PhysRevLett.105.143002.

[22] Shaohao Chen, M. Justine Bell, Annelise R. Beck, Hiroki Mashiko, Mengxi Wu, Adrian N. Pfeiffer, Mette B. Gaarde, Daniel M. Neumark, Stephen R. Leone, and Kenneth J. Schafer. Light-induced states in attosecond transient absorption spectra of laser-dressed helium. *Phys. Rev. A*, 86:063408, Dec 2012.

doi: 10.1103/PhysRevA.86.063408. URL https://link.aps.org/doi/10.1103/PhysRevA.86.063408.

[23] Andreas Kaldun, Christian Ott, Alexander Blättermann, Martin Laux, Kristina Meyer, Thomas Ding, Andreas Fischer, and Thomas Pfeifer. Extracting Phase and Amplitude Modifications of Laser-Coupled Fano Resonances. *Physical Review Letters*, 112(10):103001, mar 2014. doi: 10.1103/PhysRevLett.112.103001. URL https://link.aps.org/doi/10.1103/PhysRevLett.112.103001.

[24] Mengxi Wu, Shaohao Chen, Seth Camp, Kenneth J Schafer, and Mette B Gaarde. Theory of strong-field attosecond transient absorption. *Journal of Physics B: Atomic, Molecular and Optical Physics*, 49:062003, 3 2016. ISSN 0953-4075. doi: 10.1088/0953-4075/49/6/062003. URL https://iopscience.iop.org/article/10.1088/0953-4075/49/6/062003.

[25] M Reduzzi, W-C Chu, C Feng, A Dubrouil, J Hummert, F Calegari, F Frassetto, L Poletto, O Kornilov, M Nisoli, C-D Lin, and G Sansone. Observation of autoionization dynamics and sub-cycle quantum beating in electronic molecular wave packets. *Journal of Physics B: Atomic, Molecular and Optical Physics*, 49(6):065102, feb 2016. doi: 10.1088/0953-4075/49/6/065102. URL https://doi.org/10.1088%2F0953-4075%2F49%2F6%2F065102.

[26] Erika R. Warrick, Wei Cao, Daniel M. Neumark, and Stephen R. Leone. Probing the dynamics of rydberg and valence states of molecular nitrogen with attosecond transient absorption spectroscopy. *J. Phys. Chem. A*, 120:3165, 2016. doi: 10.1021/acs.jpca.5b11570. URL https://doi.org/10.1021/acs.jpca.5b11570.

[27] Yan Cheng, Michael Chini, Xiaowei Wang, Alberto González-Castrillo, Alicia Palacios, Luca Argenti, Fernando Martín, and Zenghu Chang. Reconstruction of an excited-state molecular wave packet with attosecond transient absorption spectroscopy. *Physical Review A*, 94(2):23403, aug 2016. doi: 10.1103/PhysRevA.94.023403. URL https://link.aps.org/doi/10.1103/PhysRevA.94.023403.

[28] Erika R. Warrick, Ashley P. Fidler, Wei Cao, Etienne Bloch, Daniel M. Neumark, and Stephen R. Leone. Multiple pulse coherent dynamics and wave packet control of the N_2 a$''$ $^1\Sigma_g^+$ dark state by attosecond four-wave mixing. *Faraday Discuss.*, 212:157–174, 2018. doi: 10.1039/C8FD00074C. URL http://dx.doi.org/10.1039/C8FD00074C.

[29] L. Drescher, G. Reitsma, T. Witting, S. Patchkovskii, J. Mikosch, and M. J. J. Vrakking. State-resolved probing of attosecond timescale molecular dipoles. *J. Phys. Chem. Lett.*, 10:265–269, 2019. doi: 10.1021/acs.jpclett.8b02878. URL https://doi.org/10.1021/acs.jpclett.8b02878.

[30] Christian Ott, Andreas Kaldun, Philipp Raith, Kristina Meyer, Martin Laux, Jörg Evers, Christoph H Keitel, Chris H Greene, and Thomas Pfeifer. Lorentz Meets Fano in Spectral Line Shapes: A Universal Phase and Its Laser Control. *Science*, 340(6133):716 LP – 720, may 2013. doi: 10.1126/science.1234407. URL http://science.sciencemag.org/content/340/6133/716.abstract.

[31] Alexander Blättermann, Christian Ott, Andreas Kaldun, Thomas Ding, and Thomas Pfeifer. Two-dimensional spectral interpretation of time-dependent absorption near laser-coupled resonances. *Journal of Physics B: Atomic, Molecular and Optical Physics*, 47(12):124008, 2014. ISSN 0953-4075. doi: 10.1088/0953-4075/47/12/124008. URL http://dx.doi.org/10.1088/0953-4075/47/12/124008.

[32] V. Stooß, S. M. Cavaletto, S. Donsa, A. Blättermann, P. Birk, C. H. Keitel, I. Březinová, J. Burgdörfer, C. Ott, and T. Pfeifer. Real-time reconstruction of the strong-field-driven dipole response. *Phys. Rev. Lett.*, 121:173005, Oct 2018. doi: 10.1103/PhysRevLett.121.173005. URL https://link.aps.org/doi/10.1103/PhysRevLett.121.173005.

[33] Patrick Nuernberger, Stefan Ruetzel, and Tobias Brixner. Multidimensional electronic spectroscopy of photochemical reactions. *Angewandte Chemie International Edition*, 54(39):11368–11386, 2015. doi: 10.1002/anie.201502974. URL https://onlinelibrary.wiley.com/doi/abs/10.1002/anie.201502974.

[34] Muath Nairat, Morgan Webb, Michael P. Esch, Vadim V. Lozovoy, Benjamin G. Levine, and Marcos Dantus. Time-resolved signatures across the intramolecular response in substituted cyanine dyes. *Phys. Chem. Chem. Phys.*, 19:14085–14095, 2017. doi: 10.1039/C7CP00119C. URL http://dx.doi.org/10.1039/C7CP00119C.

[35] Tatu Kumpulainen, Bernhard Lang, Arnulf Rosspeintner, and Eric Vauthey. Ultrafast elementary photochemical processes of organic molecules in liquid solution.

Chemical Reviews, 117(16):10826–10939, 2017. doi: 10.1021/acs.chemrev.6b00491. URL https://doi.org/10.1021/acs.chemrev.6b00491. PMID: 27957848.

[36] Thomas A. A. Oliver. Recent advances in multidimensional ultrafast spectroscopy. *Royal Society Open Science*, 5(1):171425, 2018. doi: 10.1098/rsos.171425. URL https://royalsocietypublishing.org/doi/abs/10.1098/rsos.171425.

[37] Tiago Buckup and Jérémie Léonard. *Multidimensional Time-Resolved Spectroscopy*. Springer, 2018.

[38] B. J. Pearson, J. L. White, T. C. Weinacht, and P. H. Bucksbaum. Coherent control using adaptive learning algorithms. *Phys. Rev. A*, 63:063412, May 2001. doi: 10.1103/PhysRevA.63.063412. URL https://link.aps.org/doi/10.1103/PhysRevA.63.063412.

[39] Kristina Meyer, Zuoye Liu, Niklas Müller, Jan-Michael Mewes, Andreas Dreuw, Tiago Buckup, Marcus Motzkus, and Thomas Pfeifer. Signatures and control of strong-field dynamics in a complex system. *Proceedings of the National Academy of Sciences*, 112(51):15613 LP – 15618, dec 2015. doi: 10.1073/pnas.1509201112. URL http://www.pnas.org/content/112/51/15613.abstract.

[40] M. Chini, X. Wang, Y. Cheng, Y. Wu, D. Zhao, D. A. Telnov, S. Chu, and Z. Chang. Sub-cycle Oscillations in Virtual States Brought to Light. *Scientific Reports*, 3:1105, 2013.

[41] C. H. Brito Cruz, J. P. Gordon, P. C. Becker, R. L. Fork, and C. V. Shank. Dynamics of spectral hole burning. *IEEE Journal of Quantum Electronics*, 24 (2):261–269, February 1988. doi: 10.1109/3.122.

[42] Fumio Sasaki and Shunsuke Kobayashi. Femtosecond dynamics of frenkel excitons in pseudoisocyanine j aggregates. *Japanese Journal of Applied Physics*, 34(S1): 188, jan 1995. doi: 10.7567/jjaps.34s1.188. URL https://doi.org/10.7567%2Fjjaps.34s1.188.

[43] S. Bengtsson, E. W. Larsen, D. Kroon, S. Camp, M. Miranda, C. L. Arnold, A. L'Huillier, K. J. Schafer, M. B. Gaarde, L. Rippe, and J. Mauritsson. Space–time control of free induction decay in the extreme ultraviolet. *Nature Photonics*, 11:252 – 258, 2017. doi: 10.1038/nphoton.2017.30. URL https://doi.org/10.1038/nphoton.2017.30.

[44] Thomas Ding, Christian Ott, Andreas Kaldun, Alexander Blättermann, Kristina Meyer, Veit Stooss, Marc Rebholz, Paul Birk, Maximilian Hartmann, Andrew Brown, Hugo Van Der Hart, and Thomas Pfeifer. Time-resolved four-wave-mixing spectroscopy for inner-valence transitions. *Optics Letters*, 41(4):709–712, 2016. doi: 10.1364/OL.41.000709. URL http://ol.osa.org/abstract.cfm?URI=ol-41-4-709.

[45] Gema de la Torre, Christian G Claessens, and Tomás Torres. Phthalocyanines: old dyes, new materials. Putting color in nanotechnology. *Chemical Communications*, (20):2000–2015, 2007. ISSN 1359-7345. doi: 10.1039/B614234F. URL http://dx.doi.org/10.1039/B614234F.

[46] Michael G Walter, Alexander B Rudine, and Carl C Wamser. Porphyrins and phthalocyanines in solar photovoltaic cells. *Journal of Porphyrins and Phthalocyanines*, 14(09):759–792, sep 2010. ISSN 1088-4246. doi: 10.1142/S1088424610002689. URL https://doi.org/10.1142/S1088424610002689.

[47] Raymond Bonnett. Photosensitizers of the porphyrin and phthalocyanine series for photodynamic therapy. *Chemical Society Reviews*, 24(1):19–33, 1995. ISSN 0306-0012. doi: 10.1039/CS9952400019. URL http://dx.doi.org/10.1039/CS9952400019.

[48] Karen R Py-Daniel, Joy S Namban, Laise R de Andrade, Paulo E N de Souza, Leonardo G Paterno, Ricardo B Azevedo, and Maria A G Soler. Highly efficient photodynamic therapy colloidal system based on chloroaluminum phthalocyanine/pluronic micelles. *European Journal of Pharmaceutics and Biopharmaceutics*, 103:23–31, 2016. ISSN 0939-6411. doi: 10.1016/j.ejpb.2016.03.028. URL http://www.sciencedirect.com/science/article/pii/S0939641116301047.

[49] Cristiano Ceron Jayme, Italo Rodrigo Calori, and Antonio Claudio Tedesco. Spectroscopic analysis of aluminum chloride phthalocyanine in binary water/ethanol systems for the design of a new drug delivery system for photodynamic therapy cancer treatment. *Spectrochimica Acta Part A: Molecular and Biomolecular Spectroscopy*, 153:178–183, 2016. ISSN 1386-1425. doi: 10.1016/j.saa.2015.08.027. URL http://www.sciencedirect.com/science/article/pii/S1386142515301852.

[50] Lawrence Edwards and Martin Gouterman. Porphyrins: XV. Vapor absorption

spectra and stability: Phthalocyanines. *Journal of Molecular Spectroscopy*, 33 (2):292–310, 1970. ISSN 0022-2852. doi: 10.1016/0022-2852(70)90040-8. URL http://www.sciencedirect.com/science/article/pii/0022285270900408.

[51] B. E. A. Saleh and M. C. Teich. *Fundamentals of Photonics - Second Edition*. Wiley, 2007.

[52] C. Rulliere. *Femtosecond Laser Pulses: Principles and Experiments - Second Edition*. Springer, 2005.

[53] Jean-Claude Diels and Wolfgang Rudolph. *Ultrashort laser pulse phenomena - Second Edition*. Elsevier, 2006.

[54] R. Boyd and D. Prato. *Nonlinear Optics - Third Edition*. Elsevier, 2008.

[55] Wolfgang Demtröder. *Atoms, Molecules and Photons*. Springer Berlin, Heidelberg, Heidelberg, Germany, 2018. ISBN 978-3-662-55521-7. doi: doi:10.1007/978-3-662-55523-1. URL https://doi.org/10.1007/978-3-662-55523-1.

[56] Erwin Riedel and Christoph Janiak. *Anorganische Chemie*. De Gruyter, Berlin, München, Boston, 2015. ISBN 9783110355284. doi: doi:10.1515/9783110355284. URL https://doi.org/10.1515/9783110355284.

[57] M D Feit and J A Fleck. Solution of the Schrödinger equation by a spectral method II: Vibrational energy levels of triatomic molecules. *The Journal of Chemical Physics*, 78(1):301–308, jan 1983. ISSN 0021-9606. doi: 10.1063/1.444501. URL https://doi.org/10.1063/1.444501.

[58] M. Kasha. Characterization of electronic transitions in complex molecules. *Discussions of the Faraday Society*, 9:14–19, 1950.

[59] Hermann Haken and Hans Christoph Wolf. *Molekülphysik und Quantenchemie*. Springer Berlin, Heidelberg, Heidelberg, Germany, 2006. ISBN 978-3-540-30314-5. doi: doi:10.1007/3-540-30315-4. URL https://doi.org/10.1007/3-540-30315-4.

[60] A. Zawadzka, A. Karakas, P. Płóciennik, J. Szatkowski, Z. Łukasiak, A. Kapceoglu, Y. Ceylan, and B. Sahraoui. Optical and structural characterization of thin films containing metallophthalocyanine chlorides. *Dyes and Pigments*, 112:116–126, 2015. ISSN 0143-7208. doi: https://doi.org/10.1016/j.dyepig.

2014.06.029. URL https://www.sciencedirect.com/science/article/pii/S0143720814002599.

[61] Bruno Vilsinski, Adriana Gerola, Évelin Lemos, Patricia Magalhães Barbosa, Campanholi Katieli, Gabriel Cesar, Andre Tessaro, Noboru Hioka, and Wilker Caetano. Spectroscopic study of aluminum phthalocyanine chloride (AlPcCl) in homogeneous and micro-heterogeneous media consisting of P-123 AND F-127 polymeric micelles. *Química Nova*, 38, jun 2015. doi: 10.5935/0100-4042.20150056.

[62] FEMTOLASERS Produktions GmbH. *User's Manual FEMTOPOWER™ HE/HR CEP4*. FEMTOLASERS Produktions GmbH, Vienna, Austria, 2011.

[63] FEMTOLASERS Produktions GmbH. *FEMTOSOURCE™ rainbow™ operator's manual , version 1.2*. FEMTOLASERS Produktions GmbH, Vienna, Austria, 2014.

[64] FEMTOLASERS Produktions GmbH. *CEP4™ , CEP4 PRO™, CEP4 SEED™, Module for FEMTOSOURCE™ rainbow™ operator's manual , version 1.3*. FEMTOLASERS Produktions GmbH, Vienna, Austria, 2013.

[65] M. Nisoli, S. De Silvestri, and O. Svelto. Generation of high energy 10 fs pulses by a new pulse compression technique. *Applied Physics Letters*, 68(20):2793–2795, 1996. doi: 10.1063/1.116609. URL https://doi.org/10.1063/1.116609.

[66] M. Nisoli, S. De Silvestri, O. Svelto, R. Szipöcs, K. Ferencz, Ch. Spielmann, S. Sartania, and F. Krausz. Compression of high-energy laser pulses below 5 fs. *Opt. Lett.*, 22(8):522–524, Apr 1997. doi: 10.1364/OL.22.000522. URL http://opg.optica.org/ol/abstract.cfm?URI=ol-22-8-522.

[67] Vahe Shirvanyan. Generation of sub-4-fs, mj pulses via hollow-core fiber nonlinear pulse compression by the conjugate pressure-gradient method. Master's thesis, Technische Universität München, 2015.

[68] Paul Birk. *The Dipole Response of an Ionization Threshold within Ultrashort and Strong Fields*. PhD thesis, Heidelberg University, Heidelberg, Germany, dec 2020.

[69] Maximilian David Hartmann. *Attosecond dynamics of strong-field generated ions*. PhD thesis, Heidelberg University, Heidelberg, Germany, jul 2021.

[70] Francisco Silva, Miguel Miranda, Benjamín Alonso, Jens Rauschenberger, Vladimir Pervak, and Helder Crespo. Simultaneous compression, characterization and phase stabilization of gw-level 1.4 cycle vis-nir femtosecond pulses using a single dispersion-scan setup. *Opt. Express*, 22(9):10181–10191, May 2014. doi: 10.1364/OE.22.010181. URL http://opg.optica.org/oe/abstract.cfm?URI=oe-22-9-10181.

[71] Henry Timmers, Yuki Kobayashi, Kristina F. Chang, Maurizio Reduzzi, Daniel M. Neumark, and Stephen R. Leone. Generating high-contrast, near single-cycle waveforms with third-order dispersion compensation. *Opt. Lett.*, 42(4):811–814, Feb 2017. doi: 10.1364/OL.42.000811. URL http://opg.optica.org/ol/abstract.cfm?URI=ol-42-4-811.

[72] Rick Trebino and Daniel J. Kane. Using phase retrieval to measure the intensity and phase of ultrashort pulses: frequency-resolved optical gating. *J. Opt. Soc. Am. A*, 10(5):1101–1111, May 1993. doi: 10.1364/JOSAA.10.001101. URL http://opg.optica.org/josaa/abstract.cfm?URI=josaa-10-5-1101.

[73] D.J. Kane and R. Trebino. Characterization of arbitrary femtosecond pulses using frequency-resolved optical gating. *IEEE Journal of Quantum Electronics*, 29(2):571–579, 1993. doi: 10.1109/3.199311.

[74] Vadim V. Lozovoy, Igor Pastirk, and Marcos Dantus. Multiphoton intrapulse interference. iv. ultrashort laser pulse spectral phase characterization and compensation. *Opt. Lett.*, 29(7):775–777, Apr 2004. doi: 10.1364/OL.29.000775. URL http://opg.optica.org/ol/abstract.cfm?URI=ol-29-7-775.

[75] Kenneth W. DeLong and Rick Trebino. Improved ultrashort pulse-retrieval algorithm for frequency-resolved optical gating. *J. Opt. Soc. Am. A*, 11(9):2429–2437, Sep 1994. doi: 10.1364/JOSAA.11.002429. URL http://opg.optica.org/josaa/abstract.cfm?URI=josaa-11-9-2429.

[76] JW Nicholson, FG Omenetto, DJ Funk, and AJ Taylor. Evolving frogs: phase retrieval from frequency-resolved optical gating measurements by use of genetic algorithms. *Opt Lett.*, 24(7):490–2, 1999. doi: 10.1364/ol.24.000490.

[77] Miguel Miranda, Cord L. Arnold, Thomas Fordell, Francisco Silva, Benjamín Alonso, Rosa Weigand, Anne L'Huillier, and Helder Crespo. Characterization of broadband few-cycle laser pulses with the d-scan technique. *Opt. Express*, 20(17):

18732–18743, Aug 2012. doi: 10.1364/OE.20.018732. URL http://opg.optica.org/oe/abstract.cfm?URI=oe-20-17-18732.

[78] Miguel Miranda, Thomas Fordell, Cord Arnold, Anne L'Huillier Helder, and Crespo. Simultaneous compression and characterization of ultrashort laser pulses using chirped mirrors and glass wedges. *Optics express*, 20(1):688–697, 2012. URL https://doi.org/10.1364/OE.20.000688.

[79] Benjamín Alonso, Miguel Miranda, Í nigo J. Sola, and Helder Crespo. Spatiotemporal characterization of few-cycle laser pulses. *Opt. Express*, 20(16): 17880–17893, Jul 2012. doi: 10.1364/OE.20.017880. URL http://opg.optica.org/oe/abstract.cfm?URI=oe-20-16-17880.

[80] Mathias Hoffmann, Tamas Nagy, Thomas Willemsen, Marco Jupé, Detlev Ristau, and Uwe Morgner. Pulse characterization by thg d-scan in absorbing nonlinear media. *Opt. Express*, 22(5):5234–5240, Mar 2014. doi: 10.1364/OE.22.005234. URL http://opg.optica.org/oe/abstract.cfm?URI=oe-22-5-5234.

[81] Miguel Canhota, Francisco Silva, Rosa Weigand, and Helder M. Crespo. Inline self-diffraction dispersion-scan of over octave-spanning pulses in the single-cycle regime. *Opt. Lett.*, 42(15):3048–3051, Aug 2017. doi: 10.1364/OL.42.003048. URL http://opg.optica.org/ol/abstract.cfm?URI=ol-42-15-3048.

[82] Miguel Miranda, Jo ao Penedones, Chen Guo, Anne Harth, Maïté Louisy, Lana Neoričić, Anne L'Huillier, and Cord L. Arnold. Fast iterative retrieval algorithm for ultrashort pulse characterization using dispersion scans. *J. Opt. Soc. Am. B*, 34(1):190–197, Jan 2017. doi: 10.1364/JOSAB.34.000190. URL http://opg.optica.org/josab/abstract.cfm?URI=josab-34-1-190.

[83] Esmerando Escoto, Ayhan Tajalli, Tamas Nagy, and Günter Steinmeyer. Advanced phase retrieval for dispersion scan: a comparative study. *J. Opt. Soc. Am. B*, 35(1):8–19, Jan 2018. doi: 10.1364/JOSAB.35.000008. URL http://opg.optica.org/josab/abstract.cfm?URI=josab-35-1-8.

[84] Sven Kleinert, Ayhan Tajalli, Tamas Nagy, and Uwe Morgner. Rapid phase retrieval of ultrashort pulses from dispersion scan traces using deep neural networks. *Opt. Lett.*, 44(4):979–982, Feb 2019. doi: 10.1364/OL.44.000979. URL http://opg.optica.org/ol/abstract.cfm?URI=ol-44-4-979.

[85] Maximilian David Hartmann. Characterization of few-cycle laser pulses. Master's thesis, University of Heidelberg, 2016.

[86] Sigma-Aldrich Co. *Aluminum phthalocyanine chloride SAFETY DATA SHEET, Version 6.4*. Merck KGaA, Darmstadt, Germany, 2020.

[87] Isabel Baumann. Spektroskopische analyse von aluminiumphthalocyanin-chlorid in variablen binären solvate. Bachelor's Thesis, 2022. Ruprecht-Karls-Universität Heidelberg Heidelberg.

[88] C. da Costa Castanheira, A. Persch, P. Birk, C. Ott, and T. Pfeifer. Laser-induced control of the optical response of aluminum phthalocyanine chloride complexes dissolved in ethanol. *Frontiers in Physics*, 9(627826), 2021. doi: 10.3389/fphy.2021.627826.

[89] Quan Gan, Shayu Li, Fabrice Morlet-Savary, Shuangqing Wang, Shuyin Shen, Huijun Xu, and Guoqiang Yang. Photophysical properties and optical limiting property of a soluble chloroaluminum-phthalocyanine. *Opt. Express*, 13(14):5424–5433, Jul 2005. doi: 10.1364/OPEX.13.005424. URL http://www.opticsexpress.org/abstract.cfm?URI=oe-13-14-5424.

[90] Mikhail Ya. Melnikov et al. Aluminum phthalocyanine on silica nanoparticles: Aggregation and excited states. *Macroheterocycles*, 8(3), 2015.

[91] Zuoye Liu, Stefano M. Cavaletto, Christian Ott, Kristina Meyer, Yonghao Mi, Zoltán Harman, Christoph H. Keitel, and Thomas Pfeifer. Phase reconstruction of strong-field excited systems by transient-absorption spectroscopy. *Phys. Rev. Lett.*, 115:033003, Jul 2015. doi: 10.1103/PhysRevLett.115.033003. URL https://link.aps.org/doi/10.1103/PhysRevLett.115.033003.

[92] Vadim Becquet and Stefano M Cavaletto. Transient-absorption phases with strong probe and pump pulses. *Journal of Physics B: Atomic, Molecular and Optical Physics*, 51(3):035501, jan 2018. doi: 10.1088/1361-6455/aa8e6a. URL https://doi.org/10.1088%2F1361-6455%2Faa8e6a.

[93] Princeton Instruments. *Princeton Instruments Acton Series Datasheet, Rev N3.1*. Teledyne Princeton Instruments, Tucson, USA, 2012.

[94] Photometrics. *CoolSNAP K4 Monochrome Datasheet, Rev B1*. Teledyne Photometrics, Tucson, USA, 2010.

[95] Andor Technology Oxford Instruments. *Zyla 5.5 Specification sheet for physical sciences*. Andor Technology - Oxford Instruments, Belfast, UK, 2021.

[96] LAYERTEC GmbH. Beamsplitter coating specifications. https://www.layertec.de/en/shop/datasheet-110105, 2022. Accessed: 2022-07-25.

Danksagung

Zu guter Letzt möchte ich mich bei allen bedanken, die zu dieser Arbeit beigetragen und mich sowohl professionell als auch privat unterstützt haben. Eine Doktorarbeit ist nie nur die Arbeit einer einzelnen Person, sondern das Ergebnis von Teamarbeit was Diskussionen, wissenschaftlichen und interkulturellen Austausch, und die Atmosphäre in der Gruppe mit einschließt. Deshalb möchte ich mich allen Mitgliedern der Arbeitsgruppe bedanken: Ich habe viel von euch gelernt und den großartigen Teamgeist genossen. Insbesondere geht mein Dank an:

Prof. Dr. Thomas Pfeifer, der mich zuerst als Praktikantin, später als Masterstudentin und schlussendlich als Doktorandin in der Arbeitsgruppe willkommen geheißen hat. Dein Optimismus und die Begeisterung für Physik haben mich immer wieder aufs Neue inspiriert. Auch möchte ich dir dafür danken, dass deine Bürotür für deine Studenten immer einen Spalt offen steht.

Als Nächstes möchte ich **Prof. Dr. Andreas Wolf** für die Übernahme des Zweitgutachtens dieser Arbeit danken.

Mein Dank gilt auch **Dr. Christian Ott** für die Betreuung des Projekts, die vielen Stunden an Diskussion über die Messdaten, zahlreiche Erläuterungen und das Korrekturlesen dieser Arbeit.

Dr. Maximilian Hartmann, **Dr. Veit Stoß**, **Alexander Magunia** und **Gergana Dimitrova Borisova** mit denen ich über die Jahre zusammenarbeiten durfte. Ich habe viel von euch gelernt. Danke für den Support wann immer er benötigt wurde und die schönen Momente abseits der Arbeit.

Auch möchte ich mich bei der Konstruktionsabteilung, der Werkstatt und der Elektronikabteilung des MPIK für die ausgezeichnete technische Unterstützung über

die Jahre bedanken. Mein Dank gilt hier insbsondere **Nikola Mollov** für seine entspannte Art, den Laser "einfach am laufen zu halten" - von dir habe ich sehr viel gelernt. **Alexander von der Dellen**, dafür, in technischen Notfällen alles stehen und liegen zu lassen, um zur Hilfe zur eilen. **Uwe Zeiske**, für die langjährige Unterstützung und Freundschaft - das Institut wird ohne dich, nicht mehr das gleiche sein.

Als Nächstes möchte ich mich bei meinen Studenten und co^{3}sy Teamkollegen **Andreas Persch** und **Maximilian Richter** bedanken. Nicht nur, habt ihr mir gezeigt, welchen Spaß es mir bereitet mein Wissen weiterzugeben, sondern ich konnte auch von euch vieles lernen. Ich danke euch für die großartige Teamarbeit und die vielen interessanten und lustigen Gespräche. Ich bin mir sicher, ihr werdet euren Weg gehen!

Insbesondere möchte ich mich auch bei **Marc** für die langjährige professionelle und private Unterstützung bedanken. Sei es weil "Python schon wieder nicht das macht was ich will" oder man das "gruselige schwarze Fenster" benutzen muss. Immer hast du mir mit einem Lächeln weitergeholfen. Danke für das Korrekturlesen dieser Arbeit auch insbesondere dafür, mich immer wieder auf den Boden der Tatsachen zurückzuholen, wenn mir alles zuviel ist.

Ich danke meinen Mädels **Angela**, **Pia** und **Melina** für die bedingungslose jahrelange Freundschaft. Auch wenn wir über ganz Deutschland verstreut sind, sind wir uns doch immer nah.

Bedanken möchte ich mich auch bei **Eda** für die schönsten Kindheitserinnerungen und **Lilli**, dafür, mir jeden Tag aufs Neue ein Lächeln ins Gesicht zu zaubern.

Auch möchte ich mich bei meinen **Eltern** und meinen zwei kleinen **Brüdern** bedanken. Dafür, als Familie immer füreinander da zu sein und gemeinsam durch dick und dünn zu gehen. Ein Teil dessen, wer ich heute bin, ist euer Verdienst. *Obrigado.*